EPFL

Thèse n° 8297

Metabolic rescue of muscle and muscle stem cells in muscle disease

Présentée le 27 novembre 2020

à la Faculté des sciences de la vie
Chaire Nestlé en métabolisme énergétique
Programme doctoral en biotechnologie et génie biologique

pour l'obtention du grade de Docteur ès Sciences

par

Peiling LUAN

Acceptée sur proposition du jury

Prof. D. Pioletti, président du jury
Prof. J. Auwerx, directeur de thèse
Dr R. Mounier, rapporteur
Dr N. Place, rapporteur
Prof. M. Lutolf, rapporteur

École polytechnique fédérale de Lausanne

2020

Acknowledgements

My four-year Ph.D. program is an intense and exciting experience, which was like climbing a high peak step by step accompanied with encouragement, hardship, trust and frustration. Through this spectacular journey, I have not only harvested precious knowledge, but I feel that it also helped me to grow into a real adult, who is more mature and responsible.

First and foremost, I would like to express my sincere gratitude to my tremendous supervisor, **Prof. Johan Auwerx**, for his continuous support and trust during my Ph.D. study, for his patience, motivation, and immeasurable-knowledge. I really appreciated that he gave me the chance to do an internship in his lab when I was a master student, which opened the door of stem cell research for me. After the internship, he encouraged me to start a Ph.D., continuing the scientific exploration in the field of muscle stem cell. He has been giving me freedom to manage various projects and in the same time helpfully guiding me in many different aspects of my Ph.D. life. I am very grateful for everything he taught me, in particular, professionalism, preciseness, efficacy and perseverance. He is the most enthusiastic and one of the smartest persons I have ever known. I wish I could be as enthusiastic, energetic and persistent as Johan in my future career.

I would also like to thank **Prof. Kristina Schoonjans** for her encouragement and support during my Ph.D. studies, which is truly unforgettable.

Besides my supervisor, I acknowledge Prof. Mathieus Lütolf, Dr. Nicolas Place, Dr. Remi Mounier and Prof. Dominique Pioletti, who kindly accepted to be my jury members.

My deep appreciation also goes out to **Dr. Pirkka-Pekka Laurila**, with whom I collaborated closely on several different projects for three years. He has played a major role in my Ph.D. studies through providing insightful ideas to our projects and critical help with scientific writing for publications and my thesis. We became much more than colleagues and therefore worked in a friendly and constructive team spirit.

My sincere thanks also goes to **Dr. Davide D'Amico**, who has made significant contributions to our projects. Through the collaboration with him, I have acquired experience in diverse aspects, ranging from experiment design to figure arrangement. His rigorous attitudes toward scientific research set a good example for me to do precise and efficient researches.

I will forever be thankful to another excellent colleague of mine, **Dr. Hongbo Zhang**, for his tremendous supervision, support and patience during my master thesis and the first year of my Ph.D. study. Hongbo transferred to me not only competent experiment skills and problem-solving strategies, but also the way to think about questions that occurs during research. Apart from academic-life and science, he is also one of my best friends. I earnestly hope that we could collaborate further in future in the field of muscle stem cell.

Dr. **Elena Katsyuba** is another key person in my four-year journey and I really appreciate that she taught me worm skills and supervised me for the candidacy examination.

Life could not be so wonderful without a good environment. Many thanks to the other fellow-labmates in both LISP and UPSCHOONJANS, with whom I enjoyed working everyday in the lab, including Martin Wohlwend, Dr. Yang Li, Dr. Wen Gao, Dr. Hao Li, Dr. Laurent Mouchiroud, Dr. Vincenzo Sorrentino, Dr. Adrienne Mottis, Mario Romani, Dr. Alessia Perino, Yu Sun and Xiaoxu Li for the stimulating discussions, invaluable advice and support on my research. I would also like to thank our former and current lab tachnicians, Dr. Moullan Norman, Thibaud Clerc, Sabrina Bichet, Laure Vogeleisen-Delpech, Fabiana Fraga and Carla Mendes, for their professional technical assistance. In particular, a special appreciation goes to our adored secretary Valerie Stengel for her excellent and efficient administrative work.

I also owe thanks to my Chinese friends in Switzerland who offer me numerous support for both my daily life and research activity. Particular thanks goes to Yuqing Xie, Dr. Qiqun Zeng, Tao Lin, and Zhiwen Jiang.

At this moment of accomplishment, I would like to express my deep appreciation and sincere thanks to my beloved husband, **Li,** for his selfless support, encouragement and love all the time especially during my pursuit of the Ph.D. degree, which made the completion of my thesis possible. It is the most precious fortune for me to meet him, know him and marry him during this four-year journey. When I was too frustrated to continue, he not only tried his best to keep me happy but also helped me to analyze the situation and provide constructive suggestions. I greatly value his contribution to our family and appreciate his belief in me.

At last but not least, none of this would have been possible without the love and patience from my parents. I am truly grateful to my beautiful mother and my wise father, who are always there to support, encourage, believe and love me during the past 28 years. Dear mom and dad; thank you for all you do for me and our family!

This thesis is dedicated to them, with all my love.

Peiling Luan
22nd March, 2020

Summary

Duchenne muscular dystrophy (DMD), caused by the mutation of dystrophin gene, is an X-linked disorder that affects 1 in 3500 males, leading to progressive muscle degeneration and eventually resulting in premature death. Increasing evidence indicates that DMD and age-related sarcopenia share clinical hallmarks, such as decreased metabolic activity of both myofibers and muscle stem cells (MuSCs), which results in defective MuSC function and impaired muscle regeneration. In my Ph.D. thesis, I focused on manipulating mitochondrial function, such as mitophagy, and lipid metabolism, particularly sphingolipid metabolic pathways, to restore muscle and MuSC functions in DMD and age-associated sarcopenia. My thesis consists of three projects:

Rescue of mitophagy improves muscle function in DMD. In this project, we identified defective mitophagy as a hallmark of muscular dystrophy. Rescue of dysfunctional mitophagy by dietary supplementation of Urolithin A (UA), a metabolite present in fruit extracts and a potent activator of mitophagy, improved muscle function in *mdx* mice. The beneficial effects of mitophagy restoration observed in dystrophic animals were attributed to the improvement in mitochondrial function, structural integrity of muscles, restoration of MuSC activity, and reduction in general inflammation and fibrosis.

Sphingolipid depletion improves muscle regeneration during ageing. We first established the link between sphingolipid metabolism and ageing by demonstrating that sphingolipids accumulate in skeletal muscle upon aging. We reduced skeletal muscle sphingolipid accumulation by treating aged mice with myriocin, a selective inhibitor of serine pamitoyltransferase (SPT), the first and rate-limiting enzyme of sphingolipid *de novo* synthesis pathway. Sphingolipid depletion increased MuSC regenerative ability through enhancing the proliferation and differentiation capacities of MuSCs, ultimately leading to the prevention of age-related decline in muscle mass and function.

Inhibition of sphingolipid synthesis reverts muscular dystrophy. By studying skeletal muscle transcript profiles of human muscular dystrophies, we identified upregulation of sphingolipid biosynthetic pathway as a universal feature of human patients affected with muscular dystrophy. To rescue the aberrant sphingolipid metabolism, we treated *mdx* mice with myriocin and showed that inhibition of sphingolipid generation enhanced muscle function, leading to amelioration of DMD. Furthermore, we uncovered a novel role of sphingolipid depletion in macrophage polarization and in reconstruction of the *mdx* MuSC niche, resulting in improved regenerative capacity of MuSCs.

In summary, our work establishes the essential roles of mitophagy and sphingolipid metabolism in maintaining muscle and MuSC function. Restoration of mitophagy and blockade of sphingolipid generation could therefore be attractive treatment strategies to delay the progression of DMD and age-related sarcopenia.

Key words: Muscular dystrophy, Ageing, Mitophagy, Mitochondria, Sphingolipid metabolism, Skeletal muscle, Muscle stem cell

Zusammenfassung

Die Duchenne-Muskeldystrophie (DMD), die durch die Mutation des Dystrophin-Gens verursacht wird, ist eine X-chromosomale Störung, von der 1 von 3500 Männern betroffen ist, die zu einer fortschreitenden Muskelentartung führt und schließlich zum vorzeitigen Tod führt. Zunehmende Evidenz deutet darauf hin, dass DMD und altersbedingte Sarkopenie klinische Merkmale aufweisen, wie z. B. eine verminderte Stoffwechselaktivität sowohl von Myofasern als auch von Muskelstammzellen (MuSCs), was zu einer fehlerhaften MuSC-Funktion und einer beeinträchtigten Muskelregeneration führt. In meinem Ph.D. In meiner Diplomarbeit konzentrierte ich mich auf die Manipulation der Mitochondrienfunktion wie Mitophagie und Lipidstoffwechsel, insbesondere der Sphingolipid-Stoffwechselwege, um die Muskel- und MuSC-Funktionen bei DMD und altersbedingter Sarkopenie wiederherzustellen. Meine Arbeit besteht aus drei Projekten:

Die Rettung der Mitophagie verbessert die Muskelfunktion bei DMD. In diesem Projekt haben wir eine defekte Mitophagie als Kennzeichen für Muskeldystrophie identifiziert. Die Rettung einer gestörten Mitophagie durch Nahrungsergänzung mit Urolithin A (UA), einem in Fruchtextrakten enthaltenen Metaboliten und einem starken Aktivator der Mitophagie, verbesserte die Muskelfunktion bei *mdx*-Mäusen. Die bei dystrophischen Tieren beobachteten vorteilhaften Wirkungen der Mitophagie-Wiederherstellung wurden auf die Verbesserung der Mitochondrienfunktion, die strukturelle Integrität der Muskeln, die Wiederherstellung der MuSC-Aktivität und die Verringerung der allgemeinen Entzündung und Fibrose zurückgeführt.

Sphingolipid-Depletion verbessert die Muskelregeneration während des Alterns. Wir haben zunächst den Zusammenhang zwischen dem Sphingolipid-Metabolismus und dem Altern hergestellt, indem wir gezeigt haben, dass sich Sphingolipide beim Altern im Skelettmuskel ansammeln. Wir reduzierten die Sphingolipid-Akkumulation der Skelettmuskulatur, indem wir gealterte Mäuse mit Myriocin behandelten, einem selektiven Inhibitor der Serin-Pamitoyltransferase (SPT), dem ersten und geschwindigkeitsbestimmenden Enzym des Sphingolipid-de-novo-Synthesewegs. Die Sphingolipid-Depletion erhöhte die Regenerationsfähigkeit von MuSC durch Verbesserung der Proliferations- und Differenzierungskapazitäten von MuSCs, was letztendlich zur Verhinderung eines altersbedingten Rückgangs von Muskelmasse und -funktion führte.

Die Hemmung der Sphingolipidsynthese kehrt die Muskeldystrophie zurück. Durch Untersuchung der Transkriptprofile der Skelettmuskulatur von menschlichen Muskeldystrophien identifizierten wir die Hochregulation des Sphingolipid-Biosynthesewegs als universelles Merkmal menschlicher Patienten, die an Muskeldystrophie leiden. Um den aberranten Sphingolipid-Metabolismus zu retten, behandelten wir mdx-Mäuse mit Myriocin und zeigten, dass die Hemmung der Sphingolipid-Erzeugung die Muskelfunktion verbesserte, was zu einer Verbesserung der DMD führte. Darüber hinaus haben wir eine neue Rolle der Sphingolipid-Depletion bei der Polarisation von Makrophagen und bei der Rekonstruktion der *mdx*-MuSC-Nische entdeckt, was zu revert einer verbesserten Regenerationskapazität von MuSCs führt.

Zusammenfassend legt unsere Arbeit die wesentlichen Rollen der Mitophagie und des Sphingolipid-Metabolismus bei der Aufrechterhaltung der Muskel- und MuSC-Funktion fest. Die Wiederherstellung der Mitophagie und die Blockade der Sphingolipid-Erzeugung könnten daher attraktive Behandlungsstrategien sein, um das Fortschreiten von DMD und altersbedingter Sarkopenie zu verzögern.

Schlüsselwörter: Muskeldystrophie, Altern, Mitophagie, Mitochondrien, Sphingolipid-Stoffwechsel, Skelettmuskel, Muskelstammzellen

Table of contents

ACKNOWLEDGEMENTS **1**

SUMMARY **3**

ZUSAMMENFASSUNG **4**

TABLE OF CONTENTS **5**

LIST OF FIGURES **7**

LIST OF TABLES **9**

CHAPTER 1. INTRODUCTION **10**

1.1 SKELETAL MUSCLES AND THEIR HOMEOSTASIS 10
1.1.1 Basic structure and function of skeletal muscles *10*
1.1.2 Components of DAPC and their associated muscular dystrophy *10*
1.1.3 Duchenne muscular dystrophy *12*
1.1.4 Animal models of DMD *13*
1.2 MUSCS AND MYOGENIC PATHWAYS 13
1.2.1 A brief history of MuSCs *14*
1.2.2 The function of PAX3 and PAX7 in myogenesis *14*
1.2.3 The role of MRFs in myogenic commitment *15*
1.2.4 The maintenance and self-renewal of MuSCs *16*
1.3 THE MICROENVIRONMENT SURROUNDING MUSCS 17
1.3.1 The inflammatory niche *17*
1.3.2 Muscle inflammation and muscular diseases *17*
1.4 THE ENERGY METABOLISM OF SKELETAL MUSCLE 18
1.4.1 Basic energy metabolism of muscles *18*
1.4.2 Mitochondria and skeletal muscle health *19*
1.4.3 Dysfunctional mitochondria and muscle diseases *20*
1.5 MODULATION OF ENERGY METABOLISM IN SKELETAL MUSCLES 21
1.5.1 Sphingolipid signaling pathway *21*
1.5.2 The role of sphingolipids in muscle and MuSC physiology *23*
1.5.3 Inhibition of sphingolipid de novo synthesis *23*

CHAPTER 2. UROLITHIN A IMPROVES MUSCLE FUNCTION BY RESCUING MITOPHAGY IN MUSCULAR DYSTROPHY **25**

2.1 ABSTRACT 26
2.2 INTRODUCTION 27
2.3 RESULTS 27
2.3.1 Reduced mitophagy is a hallmark of Duchenne muscular dystrophy *27*
2.3.2 UA rescued mitophagy defects and muscle function in dys-1;hlh-1 mutant C. elegans *28*
2.3.3 UA restored mitophagy and mitochondrial function in mdx mice muscle *29*
2.3.4 UA enhanced both mitophagy and regenerative ability of muscle stem cells in mdx mice *30*
2.3.5 UA improved myocellular quality and muscle function in mdx mice *31*
2.4 DISCUSSION 32
2.5 MATERIALS AND METHODS 34
2.6 ACKNOWLEDGEMENTS 38
2.7 SUPPLEMENTARY MATERIALS 39

CHAPTER 3. SPHINGOLIPID DEPLETION REVERSES AGE-ASSOCIATED SARCOPENIA AND IMPROVES MUSCLE REGENERATION **44**

3.1 ABSTRACT 45
3.2 INTRODUCTION 46
3.3 RESULTS 47
3.3.1 Ceramides accumulate in skeletal muscle upon aging 47
3.3.2 Inhibition of sphingolipid de novo synthesis prevents loss of muscle mass and function in aging 48
3.3.3 Sphingolipid reduction replenishes age-depleted MuSC pool 49
3.3.4 Myriocin primes MuSCs for accelerated regeneration 50
3.3.5 Sphingolipid depletion activates myogenic differentiation in muscle progenitor cells 51
3.3.6 Genetic variants reducing SPT expression are associated with improved fitness in aged humans 53
3.4 DISCUSSION 54
3.5 MATERIALS AND METHODS 56
3.6 ACKNOWLEDGMENTS 62
3.7 TABLE 63
3.8 SUPPLEMENTARY MATERIALS 64

CHAPTER 4. REDUCTION OF SPHINGOLIPID *DE NOVO* SYNTHESIS COUNTERACTS MUSCULAR DYSTROPHY 72

4.1 ABSTRACT 73
4.2 INTRODUCTION 74
4.3 RESULTS 75
4.3.1 Sphingolipid metabolism is dysregulated in skeletal muscle in DMD 75
4.3.2 Inhibition of sphingolipid de novo synthesis restored muscle function in mdx mice 76
4.3.3 Myriocin improved muscle regeneration through recovering MuSC function in DMD 77
4.3.4 Myriocin improved the stem cell microenvironment in mdx muscles 79
4.3.5 Myriocin protected dystrophic mice from cardiac and diaphragm failure 80
4.4 DISCUSSION 81
4.5 MATERIALS AND METHODS 84

CHAPTER 5. CONCLUSIONS, DISCUSSION AND FUTURE PERSPECTIVES 87

5.1 RESULTS ACHIEVED 87
5.2 MITOCHONDRIAL STRESS RESPONSES, MUSCS AND MUSCULAR DISEASES 87
5.3 COMPLEXITY OF SPHINGOLIPID METABOLISM 88
5.4 POTENTIAL OF CLINICAL TRANSLATION 89

REFERENCES 91

LIST OF ABBREVIATIONS 107

CURRICULUM VITAE 108

List of figures

Figure 1.1 Structure of skeletal muscle……... 11

Figure 1.2 Schematic representation of DAPC and associated muscular dystrophy…….. 12

Figure 1.3 The quiescence and activation of MuSCs……... 14

Figure 1.4 Hierachy of transcription factors regulating progression through the postnatal myogenic lineage…….. 16

Figure 1.5 Modes of MuSC division……. 17

Figure 1.6 Distinct mitophagy pathways……. 20

Figure 1.7 Structure of key sphingolipid molecules…….. 22

Figure 1.8 The pathways of sphingolipid metabolism…….. 23

Figure 2.1 Mitophagy is downregulated in human DMD…….. 28

Figure 2.2 UA treatment rescued mitophagy, mitochondrial and muscle functions in *C.elegans* model of DMD…….. 29

Figure 2.3 UA treatment rescued mitophagy, mitochondrial and muscle functions in mice models of DMD…….. 30

Figure 2.4 UA induced mitophagy and mitochondrial function in muscle stem cells (MuSCs) of *mdx* mice……31

Figure 2.5 UA reduced muscle damage and recovered muscle function in *mdx* mice…….32

Figure 2. S1 Mitophagy is downregulated in human and mouse DMD and in other neuromuscular dystrophies……... 40

Figure 2. S2 UA recovered mitophagy, mitochondrial and muscle morphology in DMD worm models……41

Figure 2. S3 UA activated mitophagy and enhanced mitochondrial function in human and mouse DMD models……41

Figure 2. S4 UA induced mitophagy, mitochondrial function and regenerative ability in MuSCs from *mdx* mice……42

Figure 2. S5 UA reduced muscle damage and ameliorated DMD symptoms in *mdx* mice…….43

Figure 3.1 Sphingolipid *de novo* synthesis is activated upon aging in skeletal muscle……48

Figure 3.2 Inactivation of sphingolipid *de novo* synthesis increases muscle mass and improves muscle function……..49

Figure 3.3 Inhibition of sphingolipid *de novo* synthesis increases MuSC proliferation and tissue count……..50

Figure 3.4 Sphingolipid depletion improves MuSC function and regenerative capacity……..51

Figure 3.5 Sphingolipid depletion cell-autonomously activates muscle differentiation in MuSCs and myoblasts……..52

Figure 3.6 Genetic evidence points to beneficial effects of sphingolipid depletion in humans……54

Figure 3. S1 Sphingomyelin and deoxysphingolipid levels in skeletal muscle in aging and upon myriocin treatment……65

Figure 3. S2 Inhibition of sphingolipid *de novo* synthesis increases MuSC proliferation and tissue count……..65

Figure 3. S3 Sphingolipid depletion improves MuSC function and muscle regeneration *in vivo*…….....66

Figure 3. S4 Single clone CRISPR-Cas9 mediated *Sptlc1* knockout promotes muscle cell differentiation in C2C12 myoblasts in a dose-dependent manner……66

Figure 3. S5 Linkage disequilibrium (LD) structure of *cis*-eQTL of human *SPTLC1* and *SPTLC2*…....67

Figure 4.1 Sphingolipid metabolism is defective in human muscular dystrophy and in a mouse model of DMD……...76

Figure 4.2 Inhibition of sphingolipid *de novo* synthesis restored integrity of muscle structures and improved muscle functions of *mdx* mice……..77

Figure 4.3 Myriocin rescued muscle regeneration and muscle stem cell functions in dystrophic animals……..78

Figure 4.4 Myriocin exhibited anti-inflammatory effects and restored the macrophage polarization in dystrophic muscles……..80

Figure 4.5 Myriocin ameliorated heart failure and respiratory dysfunctions in *mdx* mice…….81

List of tables

Table 1.1 *Pax3* and *Pax7* mutant phenotypes and functions of these factors during prenatal myogenesis……...15

Table 1.2 Metabolic characters of different types of muscle fibers……..19

Table 3.1 Clinical characteristics of the Helsinki Birth Cohort Study……63

Table 3. S1. *Cis*-eQTLs of *SPTLC1* in skeletal muscle……..67

Table 3. S2. *Cis*-eQTLs of *SPTLC2* in skeletal muscle……..67

Table 3. S3. Association of skeletal muscle transcripts of neighboring genes with *SPTLC1 cis*-eQTL rs10820917……...68

Table 3. S4. Association of skeletal muscle transcripts of neighboring genes with *SPTLC2 cis*-eQTL rs8013312……69

Table 3. S5. List of mouse primers……...70

Table 3. S6. List of guide RNAs……....70

Table 3. S7. List of plasmids……..70

Table 3. S8. List of antibodies……....71

Chapter 1. Introduction

1.1 Skeletal muscles and their homeostasis

1.1.1 Basic structure and function of skeletal muscles

Muscle tissues are categorized into three types: skeletal, cardiac and smooth muscles. Skeletal muscle, belonging to one of the three major muscle types, is named after the fact that they mainly attach to the skeletal system *via* tendons. Skeletal muscles constitute the largest organ in human body, comprising around 40% of human body weight (*1*). Functionally, skeletal muscles contract to support the movement and to allow functions, for instance, swallowing, urination and defecation, to be under voluntary control. Apart from this, skeletal muscles also contribute to the regulation of metabolism and temperature.

Structurally, each skeletal muscle is composed of bundles of elongated multinuclear cells called myofibers or myocytes. Other elements of skeletal muscle include blood vessels, nerve fibers and connective tissues (*2*). There are three layers of connective tissues surrounding these myofibers to form a complete muscle (Figure 1.1). Individual muscle is covered by a sheath of dense and irregular connective tissue named the epimysium (Figure 1.1), allowing muscles to contract and move efficiently while maintaining the integrity of the structure. In parallel, epimysium also enables the skeletal muscles to be separated from other organs so that each muscle can move independently. The second layer of connective tissue, the perimysium, encircles one bundle of muscle fibers to form a fascicle. Inside each fascicle, single muscle fibers are encased in a thin connective tissue layer consisting of collagen and reticular fibers, termed endomysium (Figure 1.1). This layer contains extracellular fluid and nutrients that are supplied by the blood to support muscle fibers.

A single muscle fiber, which has a diameter varying from 10 to 100 μm and a length of about 1 cm to 30 cm, is surrounded by a plasma membrane termed sarcolemma (*2*). Within the sarcolemma, each muscle fiber is made up of thousands of myofibrils and the sarcoplasmic reticulum that is a system to adjust intracellular calcium concentration. Myofibrils are primarily made up of two types of filaments: the thin filament and the thick filament. The myofilaments are assembled in an extremely orderly and characteristic pattern to form sarcomeres functioning as basic contractile units of skeletal muscles (Figure 1.1). The most abundant myofilament proteins are actin (thin filament) and myosin (thick filament), accounting for about 70-80% of the protein content in a single fiber. In addition to actin and myosin, there is a specific complex of several proteins that connects peripheral myofibrils to the sarcolemma. This protein complex is called dystrophin associated protein complex (DAPC). Partial or complete absence or dysfunction of one of the proteins belonging to DAPC could cause damage to sarcolemma, which eventually leads to muscle wasting and weakness (*3*).

1.1.2 Components of DAPC and their associated muscular dystrophy

The DAPC has been reported to play a structural role in linking the actin cytoskeleton to the extracellular matrix, stabilizing sarcolemma during repeated cycles of contraction and relaxation and transmitting force generated in the muscle sarcomeres to extracellular matrix (*4*). On top of the structural and mechanical functions, the DAPC is also responsible for initiating intracellular signal transduction *via* its interaction with calmodulin, Grb2 and nNOS (*5*).

Aside from dystrophin, the DAPC is composed of intracellular (neuronal nitric oxide synthase (nNOS), α1- and β1-syntrophin, caveolin-3, α-dystrobrevin), transmembrane (β-dystroglycan, α-, β-, γ-, and δ-sarcoglycan, and sarcospan) and extracellular proteins (α-dystroglycan and laminin-2) (Figure 1.2) (*6*). Some of the DAPC components, such as dystrophin, have been extensively studied due to their

tight association with different muscular dystrophies (Figure 1.2). For example, mutations in caveolin-3 are associated with autosomal dominant limb-girdle muscular dystrophy (LGMD-1C) and rippling muscle disease (*7*). The extracellular DAPC component laminin-2 is composed of α2, β1 and γ1 chains and binds to α-dystroglycan and the α7β1 integrin complex. Mutations of laminin α2 gene initiate severe congenital muscular dystrophy while they do not seem to damage the sarcolemma (*8*). The transmembrane proteins sarcoglycan family is constituted by five proteins, including α (50 kDa, also called adhalin), β (43 kDa), γ (35 kDa), δ (35 kDa) and ϵ (50 kDa). Mutations abolishing any of the sarcoglycans cause loss of the others from the sarcolemma. The absence of the α, β,γ or δ sarcoglycans caused the four recessive limb girdle muscular dystrophies 2D, 2E, 2C and 2F, respectively (*9*). As the core unit of DAPC, α- and β-dystroglycans establish the transmembrane link between laminin-2 and dystrophin. Total deletion of dystroglycans in mouse is embryonic lethal, implying the indispensable function of dystroglycans for survival (*10*). Disruption of the dystropglycan-dystrophin link causes Duchenne-like phenotypes, whereas breaking the laminin-dystroglycan link results in congenital muscular dystrophy (*5*).

Compared to the other DAPC components, dystrophin is the most widely studied. Indeed, as a 427kDa-protein, dystrophin plays a central role in assembling and maintaining the link between cytoskeletal actin and extracellular matrix. Loss of dystrophin leads to the destabilization of DAPC, therefore, contracting myofibers cannot endure the mechanical stress produced by sarcomeres and the fragile sarcolemma cannot be protected from the injuries caused by contraction (*4*), finally causing Duchenne muscular dystrophy (DMD) or Becker muscular dystrophy (BMD).

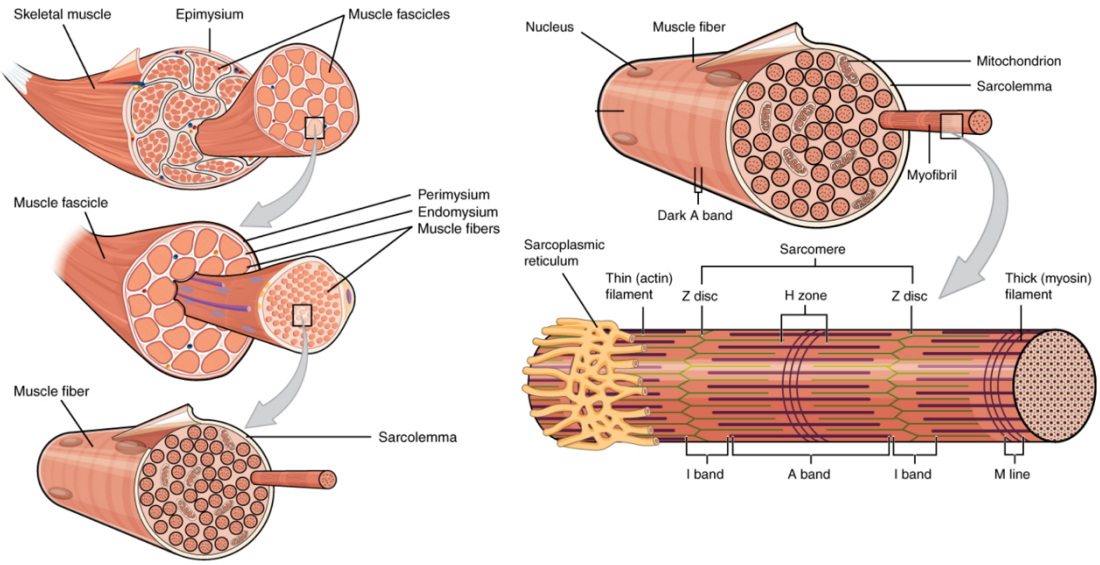

Figure 1.1. Structure of skeletal muscle. Skeletal muscles are attached to bones *via* tendons and are covered by epimysium. Muscle fibers are grouped in bundles, named as fascicles, which are surrounded by blood vessels and another layer of connective tissue, the perimysium. Inside each fascicle, muscle fibers are encased in a fibrous connective tissue termed endomysium and surrounded by a plasma membrane that is called the sarcolemma. Each individual muscle fiber contains thousands of myofibrils, which are composed of bundles of actins and myosins. Surrounding the myofibrils, there is a network of tubules and channels called sarcoplasmic reticulum. Because of the way the myofilaments are arranged, the myofibrils appear to have dark and light bands, giving the muscles a striated appearance. The dark bands are known as A bands, and consist of thick filaments and some thin filaments. At the center of the A band is the H-zone, where only thick filaments are present, and the M-line, which contains enzymes involved in energy metabolism. The light bands, known as I bands, are the regions containing thin filaments only, and are found between the A bands. The I bands are centered on a region known as the Z line, a disk made up of the protein α-actinin that anchors the thin actin filaments and acts as a boundary between sarcomere subunits. Adapted from BC Campus open education (https://opentextbc.ca/anatomyandphysiology/chapter/10-2-skeletal-muscle/)

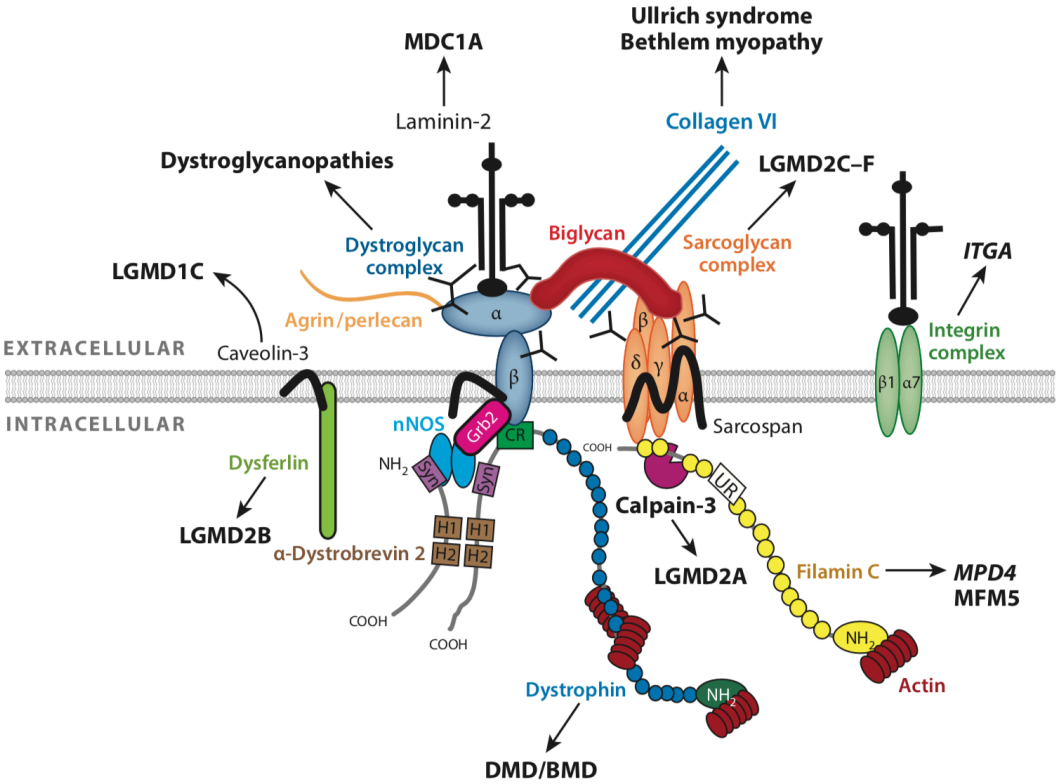

Figure 1.2. Schematic representation of dystrophin associated protein complex (DAPC) and associated muscular dystrophy. DAPC, which is a protein complex that links the intracellular cytoskeleton to the extracellular matrix (ECM), is composed of laminin, collagen and other structure proteins. Muscle-specific laminin directly connects with α-dystroglycan, which in turn interacts with other components of DAPC, including β-dystroglycan, dystrophin/utrophin, α-dystrobrevin, syntrophin, plectin sarcoglycan and sarcospan complex, biglycan and caveolin-3. The deficiency of certain DAPC components is associated with different muscular dystrophy, as demonstrated in the figure. Image adapted from Guiraud et al, Annu. Rev. Genomics Hum. Genet., 2015 (*11*).

1.1.3 Duchenne muscular dystrophy

Muscular dystrophies are a group of inherited genetic diseases that cause progressive weakness and muscle degeneration. In muscular dystrophy, the mutations of genes interfere with the production of proteins required to form healthy muscles. Among different types of muscular dystrophy, DMD is the most common and severe (*12*).

DMD is a lethal progressive pediatric muscle disorder and is genetically inherited as an X-linked disease due to the mutations in *DMD* gene that cause almost complete absence of dystrophin protein. It affects every 1 in 3500 males. This disease starts to develop in early childhood, usually between the ages 2 and 3, with diagnosis at approximately four years of age (*11*). The affected individuals show progressive muscle wasting and weakness, which further results in their dependency on a wheelchair by the age of 10 and assisted ventilation before the age of 20. Following the development of this disease, the patients will die before they are 30 years old primarily due to cardiac or respiratory failure (*12*). Compared to DMD, BMD that is caused by the reduction in the amount or change in the size of dystrophin protein, has a later onset, milder symptoms and relatively advanced survival age.

As described previously, the dysfunction of dystrophin weakens the sarcolemma, which makes the muscle cells more susceptible to damage upon muscle contraction (*13*). In line with this, increased permeability of cells has been noticed, allowing large proteins, such as creatine kinase (CK), to transverse the cell membrane into the serum. Thus, high levels of CK in circulating blood is one of the biomarkers for DMD (*14*). Furthermore, many cell signaling pathways are also affected and these factors lead to an imbalanced intracellular environment, further contributing to the muscle cell damage and necrosis. For example, increased activation of nuclear factor–κB (NF-κB) and activator protein-1 (AP-1) was observed in dystrophic muscles, inducing the transcription of inflammatory genes and

further leading to the persistent inflammation (*15, 16*). Additionally, the calcium signaling cascade, such as the ryanodine receptor (RyR1) and inositol 1,4,5-trisphosphate receptor (IP3R) dependent pathway, is also dysfunctional, delaying myogenesis in DMD fetal muscle (*17*). The resulting muscle pathology is characterized by cell degeneration and regeneration, producing myofibers of variable size and centralized nuclei while healthy muscle fibers are roughly equal in diameter with multiple nuclei in the periphery (*18*). At later stages of the disease, cells undergoing continuous degeneration and regeneration are replaced by fibrotic tissue or fatty tissue. Therefore, fibrosis is another hallmark of muscular dystrophy (*19*). To better understand the pathogenesis of DMD and to benefit the drug development, different animal models of DMD have been generated.

1.1.4 Animal models of DMD

Currently, there are more than 60 different animal models for DMD, including non-mammalian models (for example, *Caenorhabditis elegans,* Zebrafish, *Drosophila melanogaster)* and mammalian models (such as mouse, rat or dog) (*20*). Among them, the most widely used animal model of DMD is the *mdx* mouse. The *mdx* mouse carries a non-sense point mutation in exon 23 of the dystrophin gene, which aborts the expression of full-length dystrophin (*21*). Despite the deficiency of dystrophin, *mdx* mice have minimal clinical symptoms and their lifespan is only reduced by around 25%, while the lifespan of DMD patients is reduced by 75% (*22*). The muscle pathology of *mdx* mice is most pronounced between 2 and 8 weeks of age, a period characterized by the presence of necrotic foci, newly regenerated centrally nucleated myofibers and high plasma concentrations of CK. The cyclical degeneration and regeneration peaks between week 3 and 4, and then mild myopathy with its associated fibrosis persists for the remainder of animal's life (*23*). Therefore, *mdx* limb muscles usually become hypertrophic. Different from limb muscles, the diaphragm of *mdx* mice models well the diaphragm in affected humans by exhibiting a pattern of degeneration, fibrosis and severe functional deficit comparable to that seen in human DMD. The other severe dystrophic phenotypes, including muscle wasting, scoliosis and heart failure, do not appear until the mice are 15 months old (*24*).

It is well-accepted that the moderate pathology of *mdx* mice is due to the partial functional compensation of the loss of dystrophin by the homologous protein utrophin (*25*). Therefore, mice that are null for both dystrophin and utrophin (DKO) have been generated. In contrast to *mdx* mice, these DKO mice indeed have a much more severe muscle disease exhibiting growth retardation, weight loss, spinal curvature, joint contractures, early diaphragmatic pathology and premature death, which is similar to or even worse than that of humans with DMD (*26*). In spite of their advantage in well recapitulating the DMD phenotypes, the DKO mice are difficult to generate and maintain, hence, *mdx* mice are still the most commonly used murine model in DMD research.

In addition to the compensatory effects of utrophin, it has also been established that longer telomere length in murine muscles increases their regenerative capacity relative to that of human muscles, resulting in milder phenotypes of *mdx* mice (*27*). Accordingly, another mouse model for DMD has been generated by crossing *mdx* mice with mice carrying mutation in the gene that encodes telomerase (*27*). These double-knockout mice (*mdx/mTR*^{KO}), have been shown to have a marked decrease in the ability of activated muscle stem cells (MuSCs) to proliferate and support regeneration both *in vitro* and *in vivo*. The MuSCs from *mdx/mTR*^{KO} mice more closely resemble human dystrophic MuSCs, explaining why the phenotypes of these mice are more comparable to human disease. In general, the model of *mdx/mTR*^{KO} not only provides scientists with a novel tool to explore the mechanisms of dystrophic progression but also reinforces the role of MuSCs during the development of disease.

1.2 MuSCs and myogenic pathways

(Adapted from 'Regulation of muscle stem cell function by the acetyltransferase KAT2A,' Peiling Luan)

Adult skeletal muscle in mammals is a stable tissue under normal physiological conditions with only sporadic fusion of MuSCs to compensate for muscle turnover caused by daily wear and tear (*28*). However, upon acute injury, skeletal muscles will undergo a highly orchestrated degenerative and regenerative process at cellular and molecular levels, showing a remarkable ability of regeneration.

1.2.1 A brief history of MuSCs

MuSCs have been identified half a century ago as a group of mononucleated cells at the periphery of adult skeletal muscle fibers (*29*). These unique cells, residing between the basal lamina and the sarcolemma of the muscle fiber, are adult stem cells that can self-renew and are capable of generating skeletal muscle progenitor cells (differentiation). Due to their sublaminar location and association with the plasma membrane, MuSCs are also named as satellite cells.

Owing to the direct juxtaposition of MuSCs and myofibers, the hypothesis has been raised on the role of these cells in the postnatal growth, maintenance and repair of skeletal muscles (*30*). Indeed, [^{3}H]thymidine tracing experiments indicated that MuSCs are mitotically quiescent in adult skeletal muscle, while upon muscle damage and/or exercise, they rapidly enter the cell cycle (*31*). Activated MuSCs can then give rise to proliferating myoblasts, which fuse into multinucleated myotubes at the final stage of muscle regeneration (*32*) (Figure 1.3). In parallel with the myogenic differentiation, the activated MuSCs also self-renew to replenish the stem cell pool (Figure 1.3). The essential function of MuSCs in muscle regeneration has stimulated research to determine the mechanisms that control and preserve the balance between stem cell differentiation and self-renewal. Since the first observation of MuSCs, accumulating evidence has indicated that complex regulatory networks composed of growth factors, stem cell niche, myogenic regulatory factors and the key transcriptional regulators such as PAX3 and PAX7, are involved in the regulation of MuSCs maintenance and differentiation during muscle regeneration (*33*).

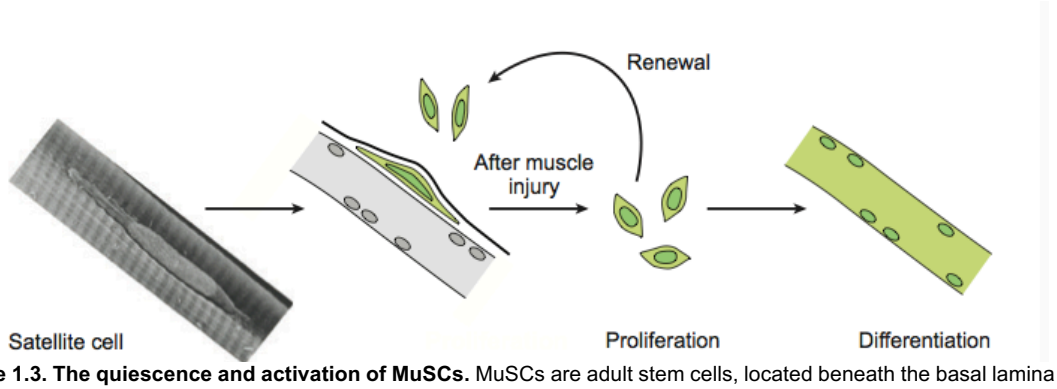

Figure 1.3. The quiescence and activation of MuSCs. MuSCs are adult stem cells, located beneath the basal lamina of muscle fibers, which can self-renew and are capable of giving rise to skeletal muscle progenitor cells. Under normal physiological conditions, MuSCs remain quiescent. After muscle injury, quiescent MuSCs are activated to differentiate into muscle fibers and meanwhile to self-renew. Modified from: Buckingham *et al.,* Annu. Rev. Cell Dev. Biol. 2007(*34*).

1.2.2 The function of PAX3 and PAX7 in myogenesis

PAX3 and PAX7 both are paralog transcription factors that are structurally characterized by the presence of a Paired Domain (PD), an Octapeptide motif (OP) and a Homeobox DNA-binding Domain (HD) (*35*). As a typical marker of MuSCs, PAX7 is usually highly expressed in quiescent MuSCs and in proliferating myoblasts (*36*). Knock-out of the *Pax7* gene in mice resulted in complete absence of MuSCs, which further caused muscle atrophy and ultimately led to death (*37*).

Though PAX7 and its paralog PAX3 are key regulators of myogenesis, they have overlapping functions only in myogenic differentiation. Distinct phenotypes of *Pax3*- or *Pax7*-knockout mice (Table 1.1) indicated that PAX3 is uniquely involved in embryonic development (*38*) while PAX7 plays an essential role in the specification of MuSCs (*34*). PAX7 can rescue almost all phenotypes caused by PAX3-deficiency, but it is unable to fully recover the lack of delamination and long-range migration of muscle progenitors to the limb bud, which suggests that PAX3 is solely responsible for this developmental activity (*39*). Taken together, these results indicate that PAX3 and PAX7 have partially overlapping but not redundant roles in myogenesis.

PAX3 and PAX7 not only control critical aspects of the behavior of muscle progenitor cells, including cell survival, cell proliferation and migration, but also regulate the entry of these cells into the myogenic program (*34*).

As PAX3 has a robust expression exclusively in the embryo but is downregulated after birth, it was concluded that PAX3 plays an important role in orchestrating myogenesis in the embryo, yet is lowly expressed in most postnatal MuSCs (Figure 1.4). Recent researches presented that $PAX3^{+}$ myogenic cells contribute to adult muscle regeneration (*40*), and PAX3 regulates MuSC differentiation independent of myogenic regulatory network (*41*), suggesting that PAX3 is also required in postnatal MuSCs. In contrast, PAX7 expression is maintained in all satellite cells and proliferating myoblasts but is sharply downregulated immediately before differentiation (*42*) (Figure 1.4), implying a function of PAX7 in maintaining the undifferentiated state of MuSCs. Therefore, in response to muscle damage, activated MuSCs have to downregulate PAX7 and progressively initiate the synthesis of early myogenic regulatory factors (MRFs), such as Myogenic Factor 5 (MYF5) and Myoblast Determination Protein (MYOD), when withdrawing from the cell cycle and preparing for the myogenic differentiation (*43*) (Figure 1.4).

Table 1.1 *Pax3* and *Pax7* mutant phenotypes and functions of these factors during prenatal myogenesis

Age	*Pax3*		*Pax7*		*Pax3:Pax7*	
	Mutant phenotype	Function	Mutant phenotype	Function	Mutant phenotype	Function
E9.5–E12.5	Reduced epaxial and hypaxial dermomyotome Disorganised myotome No migratory myogenesis	Survival of hypaxial dermomyotome Upstream regulation of myogenic hierarchies (*Myf5; MyoD; Six1/4*) Activation of *c-met*	Normal	(Masked by Pax3)	Primary myotome reduced and disorganised No limb and other muscles of migratory origin	Survival and specification of embryonic myogenic progenitor cells
E12.5–E14.5	Abnormal trunk myogenesis No myogenic cells of migratory origin (limb, diaphragm, part of tongue)	Consequences of early myogenic defects Consequences of early myogenic defects	Normal	(Masked by Pax3)	Major trunk muscle deficit No limb and other muscles of migratory origin	Survival and specification of embryonic myogenic progenitor cells
E15–E18.5	Embryonic lethality with most *Pax3* alleles	Consequences of early myogenic defects in few surviving foetuses	Normal	(Masked by Pax3)	Complete mutants do not survive; conditional not reported	N/A

Modified from Buckingham *et al,* Seminars in Cell & Developmental Biology 44 (2015) (*44*)

1.2.3 The role of MRFs in myogenic commitment

Quiescent MuSCs are characterized by the expression of PAX7, but they do not express MYOD or Myogenin (MYOG) (*45*). Consequent to muscle damage, activation of MuSCs into myoblasts is typified by the upregulation of basic helix-loop-helix MRF transcription factors (MYF5, MYOD, MYOG, MRF4) (*46*). PAX3 and PAX7 lie upstream of the MRFs and the nature of the hierarchy depends on the spatiotemporal context (*47*). In embryonic myogenesis, PAX3 and PAX7 act upstream of both MYF5 and MYOD (*48*). In satellite cells of the postnatal skeletal muscle, MYOD expression depends on PAX3/7 while MYF5 is possibly independent of PAX regulation[13].

Gene targeting and expression analysis have displayed a functional classification of MRFs: MYF5 and MYOD belong to the group of determination factors, while MYOG and MRF4 constitute differentiation factors (*49*). Entry into the myogenic program depends on the determination factors conferring the skeletal muscle identity, followed by activation of myogenic differentiation factors and consequent formation of skeletal muscles.

MYF5 and MYOD are expressed in proliferating myoblasts and subject to cycle regulation (*50*). Previous work has demonstrated that MYF5 is expressed before MYOD at the onset of myogenesis (*51*). MYOD is shortly upregulated after the beginning of differentiation. The expression of MYOD as well as high levels of MYF5 lead to the activation of MYOG, which was reported to negatively regulate PAX7 at the protein level (*52*) and induces new muscle fiber formation. After this point, MYF5 and MYOD expression levels gradually decline. The level of MYOG increases through differentiation, and then decreases prior to upregulation of MRF4 (*53*) (Figure 1.4). In addition to MRFs, the Myocyte Enhancer Factor 2 (MEF2) class of transcription factors also has an important regulatory role in the control of myogenesis. Instead of having myogenic activity, MEF2 proteins potentiate the functions of MRFs through transcriptional cooperation (*54*).

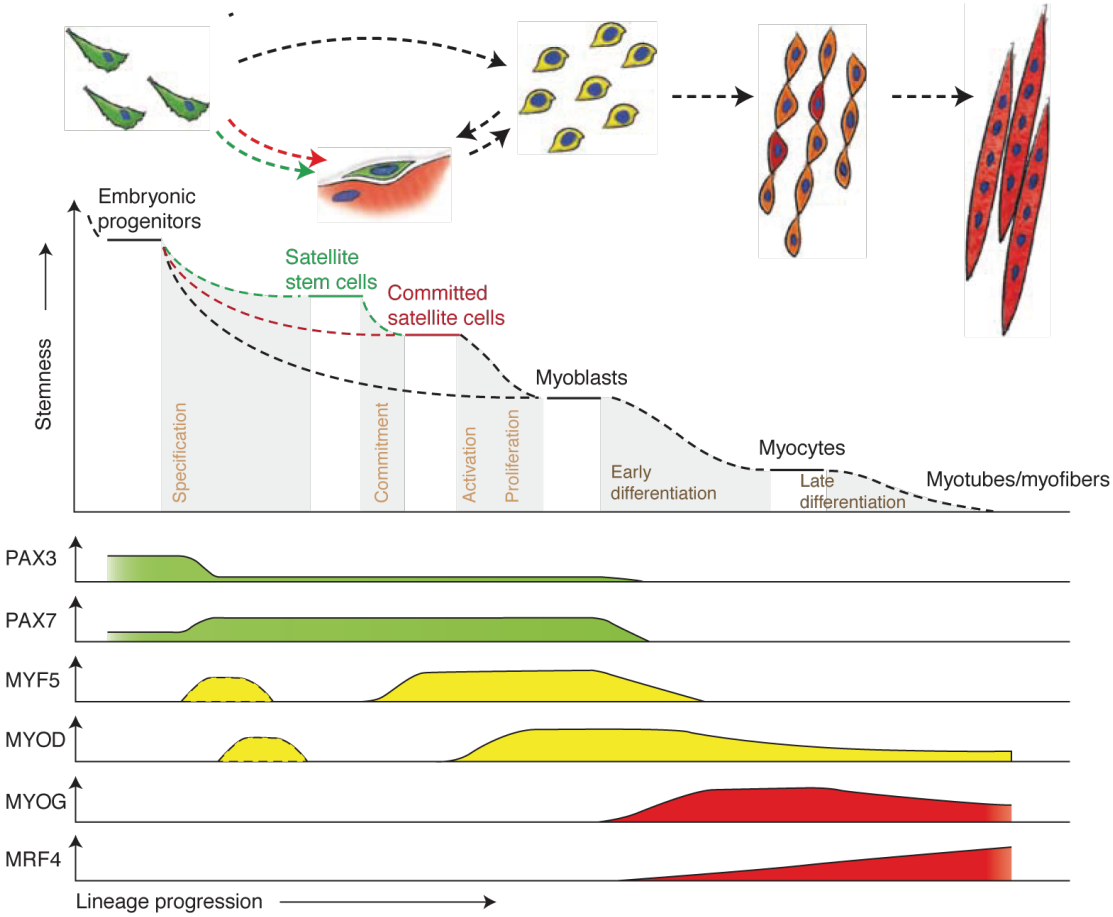

Figure 1.4. Hierachy of transcription factors regulating progression through the postnatal myogenic lineage Muscle progenitors that are involved in embryonic muscle differentiation skip the quiescent MuSC stage and directly become myoblast cells. Some embryonic progenitors remain as MuSCs in postnatal muscles and form a heterogeneous population of quiescent and activated MuSCs. Activated MuSCs can return to quiescent state in addition to entering the myogenic program. PAX3/7 are master regulators of early lineage specification, whereas MYF5 and MYOD commit cells to the myogenic program. Expression of the terminal differentiation genes, needed for the fusion of myocytes and the formation of myotubes, are performed by both MYOG and MRF4. Adapted from *Cold Spring Harb Perspect Biol 2012*, C.Florian Bentzinger et al (*55*).

1.2.4 The maintenance and self-renewal of MuSCs

As aforementioned, skeletal muscle has remarkable regenerative capacity and even following multiple rounds of injury, the reservoir of MuSCs is still maintained at a constant size. This suggests that, apart from the differentiation program, MuSCs are able to display significant self-renewal capacity, which constitutes another hallmark of MuSC. The most classic experiment proving MuSC self-renewal capacity is transplantation of myofibers into the hind limb of immunodeficient *mdx* (*scid-mdx*) mouse model (*56*). It was found that grafted MuSCs could undergo a 10-fold expansion *via* self-renewal. Additionally, one grafted fiber could give rise to more than 100 myofibers, which contain around 25000-30000 differentiated myonuclei (*57*).

How MuSCs can self-renew themselves has remained a fundamental question of MuSC biology. It was established that MuSCs can divide and self-renew in two ways: through symmetric and asymmetric cell division (*58*) (Figure 1.5). In asymmetric cell division, one parental stem cell divides into two daughter cells with different functions, one stem cell and one progenitor cell destined for differentiation. In symmetric division, two daughter cells with equal stemness are produced (*28*). Asymmetric divisions are only observed in $PAX7^+/MYF5^-$ cells, giving rise to one stem cell ($PAX7^+/MYF5^-$) and one myogenic cell ($PAX7^+/MYF5^+$); while symmetric divisions occur in both $PAX7^+/MYF5^-$ and $PAX7^+/MYF5^+$ cells (*28*). Transplantation of both $PAX7^+/MYF5^-$ and $PAX7^+/MYF5^+$ cells into mice lacking endogenous MuSCs demonstrated that only $PAX7^+/MYF5^-$ can reconstitute the MuSC population, suggesting that $PAX7^+/MYF5^-$ cells are *bona fide* stem cells (*59*).

Although asymmetric self-renewal may be sufficient under normal physiological conditions, MuSCs are likely to favor symmetric divisions to replenish and expand their pool in response to an acute need of a large number of MuSCs after injury or disease. Some groups revealed that, in damaged muscles, in addition to intrinsic cues such as MYF5, the MuSC niche also secretes Wnt7a during muscle regeneration to promote symmetric self-renewal (*60*) (Figure 1.5), which indicated the potential of MuSC niche in governing the choice of MuSC between symmetric and asymmetric division.

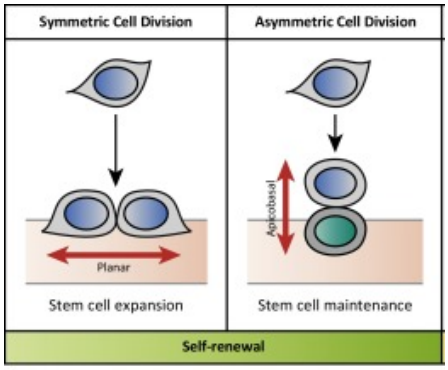

Figure 1.5. Modes of MuSC division. Satellite stem cells can self-renew *via* symmetric or asymmetric cell divisions. A symmetric cell division along the planar axis (with respect to the myofiber) generates two daughter stem cells. Asymmetric cell divisions along the apicobasal axis give rise to a stem cell and a committed myogenic progenitor cell. Modified from Trends in Molecular Medicine, 2016, NC. Chang et al (*61*).

1.3 The microenvironment surrounding MuSCs

MuSCs are exposed to a highly specified environment called the MuSC niche, which consists of extracellular matrix (ECM), vascular and neural networks, different types of surrounding cells, for example, immune cells, and various diffusible molecules (*28*). The dynamic interactions between MuSCs and their niche play a critical role in the regulation of MuSC quiescence, self-renewal and differentiation. Therefore, understanding the interactions between MuSCs and their niche is of paramount importance for developing therapies to treat age-related sarcopenia and other muscular dystrophies. Here, I will primarily introduce the inflammatory environment surrounding MuSCs, which is involved in the pathogenesis of various muscle diseases, and how dysfunctional niche impairs the regenerative potential of MuSCs and thereby contributes to muscle diseases.

1.3.1 The inflammatory niche

The regeneration of skeletal muscle is a tightly regulated process, during which quiescent MuSCs are activated to proliferate, differentiate and then fuse to form myotubes. The coordination of myogenesis involves the cooperation of numerous other components, in particular, the inflammatory response stimulated by muscle damage. Macrophages are the predominant immune cells that accumulate in skeletal muscles at the onset of injury-induced inflammation (*62*). During muscle regeneration, macrophages are key regulators of different biological processes including myogenesis, fibrosis, inflammation and revascularization (*63*).

Macrophages are immunologically classified into two subsets based on their functions. The pro-inflammatory M1 macrophages are dominant during the inflammatory phase and are responsible for the clearance of cell debris during muscle repair. The anti-inflammatory M2 macrophages, accumulate at the site of injury after the necrotic tissues have been removed and participate in the regeneration and remodeling of tissues. It was observed that in the regenerating muscle, M1 macrophages are close to proliferating MuSCs, while M2 macrophages reside near the regenerating area containing differentiated myoblasts (*64*). To further characterize the role of different subpopulation of macrophages, depletion experiments have been performed. Notably, suppression of the ability of macrophages to switch to M1 phenotype reduces muscle fiber growth without affecting the removal of necrotic tissues (*65*). In turn, the depletion of MuSCs was shown to attenuate macrophage transition to the M2 phenotype, suggesting the existence of a regulatory feedback by which myogenic cells affect the polarization of macrophages (*66*).

1.3.2 Muscle inflammation and muscular diseases

Many muscular diseases are associated with chronic inflammation and impaired muscle regeneration. Among them, DMD is the most studied form of muscular disorder. In DMD, the conflicting signals simultaneously secreted by degenerative and regenerative environments disrupt macrophage polarization (*62*), leading to the perturbation of the inflammatory process, enhancement of myofiber degeneration, decline in myogenesis, stimulation of fibrosis and eventually acceleration of the disease. Different studies have proven that, by directing macrophages towards anti-inflammatory M2 phenotype, which restored the balance of macrophage polarization, muscle functions could be improved (*67, 68*). In addition to muscular diseases, ageing is also associated with progressive degeneration of skeletal muscles. Evidence suggests that altered composition of macrophages during ageing also causes dysfunctional MuSCs and hence defective muscle regeneration (*69*). Considering the detrimental effects of macrophages in dystrophic and ageing muscles, modulating macrophage phenotype could be another potential strategy to treat DMD and age-associated sarcopenia.

1.4 The energy metabolism of skeletal muscle

1.4.1 Basic energy metabolism of muscles

Muscle contraction relies on the breakdown of adenosine triphosphate (ATP) and the concomitant release of free energy (*70*). The intracellular store of ATP is small, and will be depleted in two seconds if the muscle is fully activated (*71*). Therefore, to sustain muscle contraction, other metabolic pathways must be activated. In skeletal muscles, there are two main energy pathways to replenish ATP: the anaerobic and aerobic pathways. The anaerobic pathway can more rapidly generate ATP, and hence dominates during high-intensity physical activity of short duration, whereas the aerobic pathway dominates during prolonged submaximal exercise (*72*). The major anaerobic pathways to regenerate ATP are the degradation of phosphocreatine and the conversion of glucose to pyruvate. Oxidative metabolism of carbohydrates and lipids dominates in ATP-producing system during aerobic metabolism (*73*).

To cope with a variety of activities, ranging from supporting the body weight to performing explosive movements in response to an unexpected threat, skeletal muscle is composed of fibers with different metabolic profile, contractile speed and cellular Ca^{2+} handling (*74*). Currently, the skeletal muscle fiber classification is based on the myosin heavy chain (MyHC) isoforms. In general, the muscle fibers are classified into type I, IIa, IIx and IIb, among which, type I is the slowest, type IIa is intermediate and IIx/b is the fastest at cross-bridge cycling (*72*). In addition to the different MyHC isoform, there are other important differences between fibers related to energy metabolism. For example, fast-twitch fibers consume ATP more rapidly compared to the slow ones (*75*); the major ATP-consuming protein in skeletal muscles, the sarcoplasmic reticulum (SR) Ca^{2+} pump, also has two isoforms, SERCA1 in fast type II fibers and SERCA2 in slow type I fibers, and the density of pumps is also higher in fast than in slow fibers (*76*). In summary, skeletal muscle fibers exhibit distinct metabolic profiles, suited for their diverse roles in physical activity (Table 1.2).

Table 1.2 Metabolic characters of different types of muscle fibers

	Type I fibers	Type II a fibers	Type II x fibers	Type II b fibers
Contraction time	Slow	Moderately Fast	Fast	Very fast
Size of motor neuron	Small	Medium	Large	Very large
Resistance to fatigue	High	Fairly high	Intermediate	Low
Activity Used for	Aerobic	Long-term anaerobic	Short-term anaerobic	Short-term anaerobic
Maximum duration of use	Hours	<30 minutes	<5 minutes	<1 minute
Power produced	Low	Medium	High	Very high
Mitochondrial density	High	High	Medium	Low
Capillary density	High	Intermediate	Low	Low
Oxidative capacity	High	High	Intermediate	Low
Glycolytic capacity	Low	High	High	High
Major storage fuel	Triglycerides	Creatine phosphate, glycogen	Creatine phosphate, glycogen	Creatine phosphate, glycogen
Myosin heavy chain, human genes	MYH7	MYH2	MYH1	MYH4

Adapted from website Strong By Science (https://www.strongerbyscience.com/muscle-fiber-type/)

1.4.2 Mitochondria and skeletal muscle health

Skeletal muscle mitochondria are highly dynamic organelles that are essential for maintaining muscle energy homeostasis. To meet energy and contraction demands of the muscles, mitochondria usually undergo remarkable remodeling in response to various physiological and pathophysiological stress (*77*). The changes in energy demand mostly depend on changes in physical activities. For instance, endurance exercise training is associated with increased mitochondrial content and mass while obesity, diabetes, and ageing are characterized by decreases in mitochondrial content and oxidative energy metabolism (*78*). Mitochondrial biogenesis alone is not sufficient to support mitochondrial homeostasis. A highly regulated quality control system to remove damaged mitochondria is required in muscles. Mitochondria mainly adopt two mechanisms for quality control, including proteolysis and mitophagy. These mechanisms respond to damage caused by oxidative stress, misfolded or damaged proteins, or defects in the electron transport chain. Finally, at the organelle level, mitochondrial quality is sustained through the coordination of mitochondrial biogenesis and the elimination of damaged mitochondria. Here, we will focus on mitophagy.

As an important mitochondrial quality-control mechanism, mitophagy has been extensively studied for decades. Mitophagy is defined as the selective removal of mitochondria *via* autophagy. In mammals, both ubiquitin-dependent and ubiquitin-independent pathways have been identified (*79*). In the ubiquitin-dependent pathways, PTEN-induced putative kinase 1 (PINK1), a mitochondrial serine/threonine-protein, and PARKIN, known as a cytosolic E3-ubiquitin ligase, play essential roles in mitophagy (*80, 81*). Under normal conditions, PINK1 is transported into mitochondria for degradation. Upon acute mitochondrial stress (Figure 1.6), depolarization of the mitochondrial membrane stabilizes PINK1, which subsequently phosphorylates ubiquitin on serine 65 (Ser65) and then recruits PARKIN onto mitochondria (*82*). Recruited PARKIN is phosphorylated and activated by PINK1 on the mitochondrial membrane, and then it polyubiquitinates its substrates (*83*). The polyubiquitination of substrates leads to their degradation by proteasome, further inducing the removal of damaged mitochondria (*84*). In the ubiquitin-independent pathway, diverse LC3 receptors, including BNIP3, FUNDC1, are located on the mitochondrial membrane and directly bind to LC3, recruiting the damaged mitochondria to autophagosomes (Figure 1.6) (*85*).

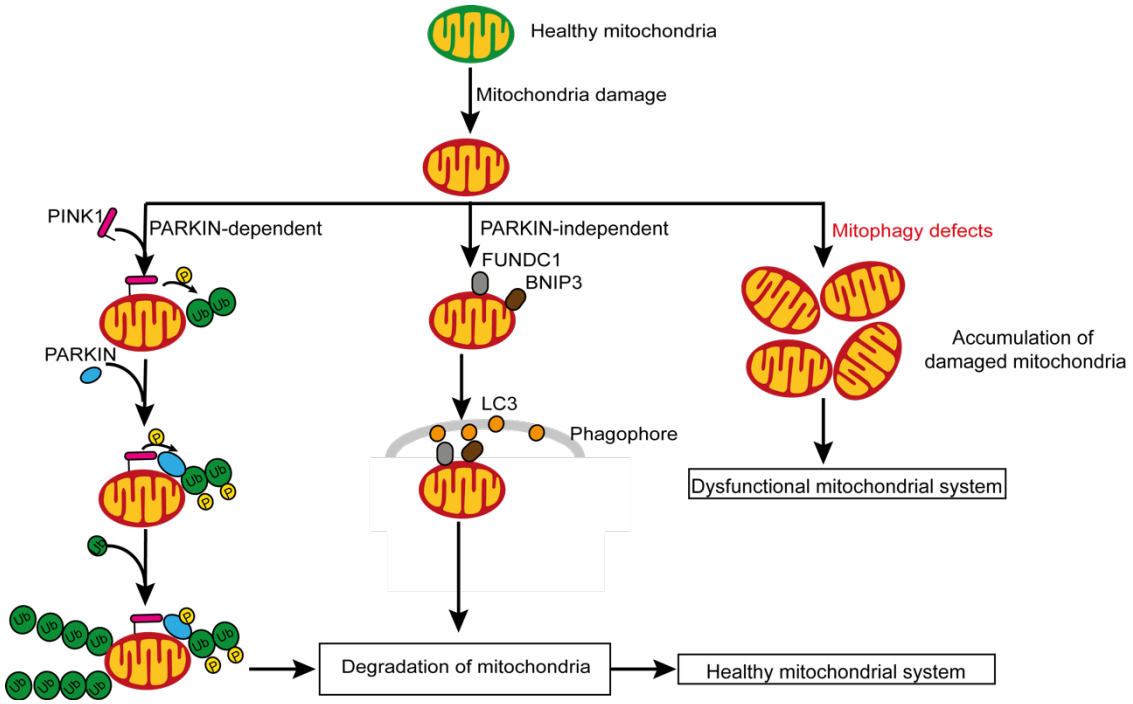

Figure 1.6. Distinct mitophagy pathways. In response to mitochondrial damage, there are generally two mitophagy pathways, including PARKIN-dependent or PARKIN-independent pathways, which both result in the degradation of dysfunctional mitochondria and maintain a healthy mitochondrial system. However, with defective mitophagy, damaged mitochondria will accumulate, which eventually lead to a dysfunctional mitochondrial system.

Apart from participating in the control of mitochondrial quality, mitophagy has also been involved in some physiological activities, such as cell development and stem cell differentiation (*86, 87*). Defective mitophagy is associated with various pathological conditions, among which neurodegenerative diseases are the most extensively explored. PINK1 and PARKIN are known to exert neuron protective effects in a mitophagy-dependent way, and mutations in PINK1 and PARKIN cause Parkinson's disease (*88*). Furthermore, during the progress of Alzheimer's disease, PARKIN is required for the removal of mitochondria and its overexpression ameliorates the symptoms of this disease (*89*). Abnormal mitophagy was also observed in Huntington's disease (*90*). In addition to neurodegenerative disease, decreased mitophagy is also linked with metabolic reprogramming in cancer cells (*91*). Besides, mitophagy protects renal cells from damage caused by acute kidney injury and metabolic acidosis, a cause of chronic kidney disease (*92*). In non-alcoholic fatty liver disease (NAFLD), stimulation of mitophagy has also been observed to relieve the disease symptoms (*93*). Although dysfunctional mitophagy has been found to be relevant to multiple diseases, the role of mitophagy in muscle diseases still remains to be explored.

1.4.3 Dysfunctional mitochondria and muscle diseases

Since mitochondria play a critical role in the energy metabolism of skeletal muscle, dysfunctional mitochondria have been implicated in the pathogenesis of many diseases, including muscular dystrophy, atrophy, type 2 diabetes, and age-related sarcopenia. Here, I will discuss the relationship between mitochondrial remodeling and muscular dystrophy and ageing.

The absence of dystrophin in DMD disease causes sarcolemmal tears, which consequently leads to an overload of calcium in dystrophic muscles, further causing mitochondrial swelling, increased production of mitochondrial ROS and other markers of mitochondrial stress (*94*). Indeed, previous studies provided evidence that DMD is characterized by mitochondrial dysfunction, including increase in membrane potential, decrease in respiratory rate, and reduced ATP production (*95*), which further exacerbates muscular dystrophy (*96*). Numerous studies have demonstrated that ameliorating aberrant mitochondrial function in *mdx* mice could partially reverse dystrophic pathology (*97, 98*). For example, boosting the level of nicotinamide adenine dinucleotide (NAD^+), a metabolic cofactor shown to boost

mitochondrial function in muscle, was shown to enhance functional capacity of muscles in muscular dystrophy (*97*). In spite of the diminished mitochondrial functions, mitochondrial content is not evidently reduced in *mdx* mice (*99*). Considering the reduced mitochondrial biogenesis and conserved mitochondrial content in dystrophic muscles, one might expect that elimination of damaged mitochondria might be compromised in DMD.

Sarcopenia is defined as age-related decline in muscle mass and function. Studies on muscle specimens from healthy individuals revealed age-related decreases in mitochondrial mass, oxygen consumption, ATP synthesis, and enzymes activities of tricarboxylic acid cycle (*100*). Decreased mitochondrial function correlates with slow speed and reduced muscle volume in older persons (*101*). In addition to declined mitochondrial biogenesis, mitophagy pathway is also impaired in ageing (*102*), contributing to the defective turnover of mitochondria in ageing muscles.

The deficits in mitochondrial function and content in muscle diseases make therapeutic targeting of mitochondria-related pathways attractive. Diverse approaches, particularly, pharmacological strategies, have been shown to enhance muscle mitochondrial function. For instance, Urolithin A (UA), a fruit derived metabolite and a potent activator of mitophagy, has been demonstrated to increase mitochondrial and skeletal muscle function in both aged rodents and elderly humans (*103, 104*). There has also been intense interest in activating the sirtuin pathway as a mechanism to boost bioenergetics. The primary method to achieve this is the use of NAD^+ boosters, for example, nicotinamide riboside (NR) to activate Sirtuin1. Recent studies from our lab have shown that NR is able to restore the functions of muscle and MuSCs in aged mice and also extend the lifespan of mice (*105*). NR supplementation in *mdx* or DKO mice can also improve the mitochondrial functions and therefore ameliorate the dystrophic phenotypes (*97*). These data warrant further investigations of compounds that are able to rescue mitochondrial functions, in conditions of impaired muscle functions, including DMD, other muscular dystrophies and sarcopenia.

1.5 Modulation of energy metabolism in skeletal muscles

Mitochondria are the organelles where ATP synthesis occurs with the supply of carbohydrates and lipids, both of which are important substrates for fueling the energy demand of skeletal muscles (*106*). In addition to serving as energy substrates, recent discoveries in lipidology have identified a bioactive role for specific cellular lipids. In the past decades, most interest has focused on the bioactive role of sphingolipids.

1.5.1 Sphingolipid signaling pathway

Sphingolipids, major constituents of cellular membranes (*107*), are a diverse group of naturally occurring glycolipids, characterized by their sphingoid base (Figure 1.7). Bioactive sphingolipids constitute a family of lipids, including sphingosine, ceramide, sphingosine-1-phosphate (S1P) and ceramide-1-phosphate (*108*) (Figure 1.7). Ceramide, a mediator of various stress responses, particularly in ageing, occupies a central position in sphingolipid metabolism (*109*) (Figure 1.8). Mammalian sphingolipid metabolism has three major metabolic pathways: the *de novo* pathway, the salvage pathway and the sphingomyelin pathway (Figure 1.8).

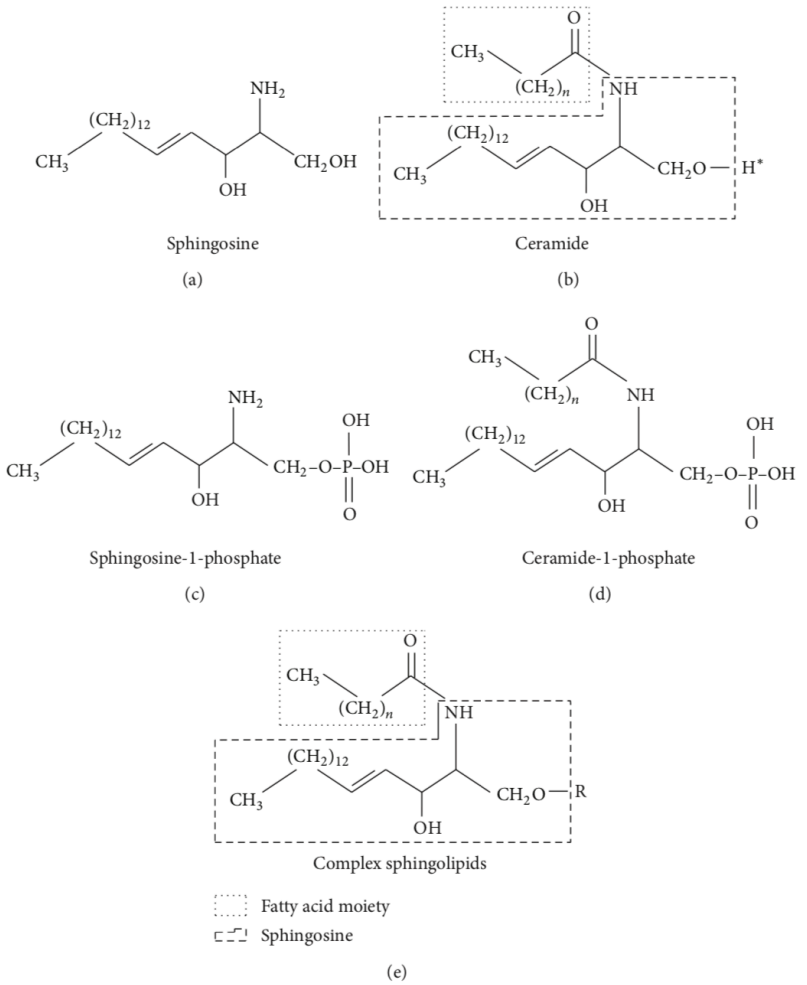

Figure 1.7. Structure of key sphingolipid molecules Sphingoid backbone is the basal unit of all sphingolipids, and sphingosine is the main sphingoid base in mammals. (a) Sphingosine transforms into ceramide through acquiring a long chain fatty acid *via* amide linkage. (b) Complex sphingolipids are obtained by replacement of hydrogen group of ceramide (H^*) with various functional head groups (represented as R group in (e)). Complex sphingolipids vary in the nature of the polar head groups. For example, in sphingomyelin the head group is phosphocholine whereas in glycosphingolipids the head group could be one or more sugar residues. The phosphorylated derivatives, namely, sphingosine-1- phosphate (c) and ceramide-1-phosphate (d), are obtained by action of respective kinases on sphingosine and sphingosine-1-phosphate. Adapted from Journal of Lipids, 2013, R. Rao et al (*110*).

Sphingolipid *de novo* synthesis initiates with the condensation of a serine and palmitate, catalyzed by the serine palmitoyl-CoA transferase (SPT) a heterodimer encoded by the genes *SPTLC1*, *SPTLC2* and the recently identified *SPTLC3 (111)*. The following step in the synthesis is performed by 3-ketodihydrosphingosine reductase (KDHR), producing dihydrosphingosine. Then, dihydrosphingosine is further acylated by six different ceramide synthases CerS1-6. In mammals, each individual ceramide synthase has a distinct function in the synthesis of dihydroceramide (*112*). For instance, CerS1 has preference for C18 acyl chains (*113*); CerS2 is primarily responsible for the formation of very long chain, such as C24- ceramides (*114*); CerS5 and CerS6 preferentially generate C16- and C14-ceramide species (*115*). Dihydroceramide Δ4-desaturase (DEGS), which is encoded by the gene *DEGS1,* catalyzes the formation of ceramides through producing double bond in the C4-C5 position of dihydroceramide (*116*). Finally, ceramides will serve as the substrates for the synthesis of the heterogeneous and complex glycosphingolipids (Figure 1.8). The biophysical and signaling property of sphingolipids allows them to participate in the regulation of various cellular procedures, such as cell proliferation, differentiation, migration, death, and senescence (*117*).

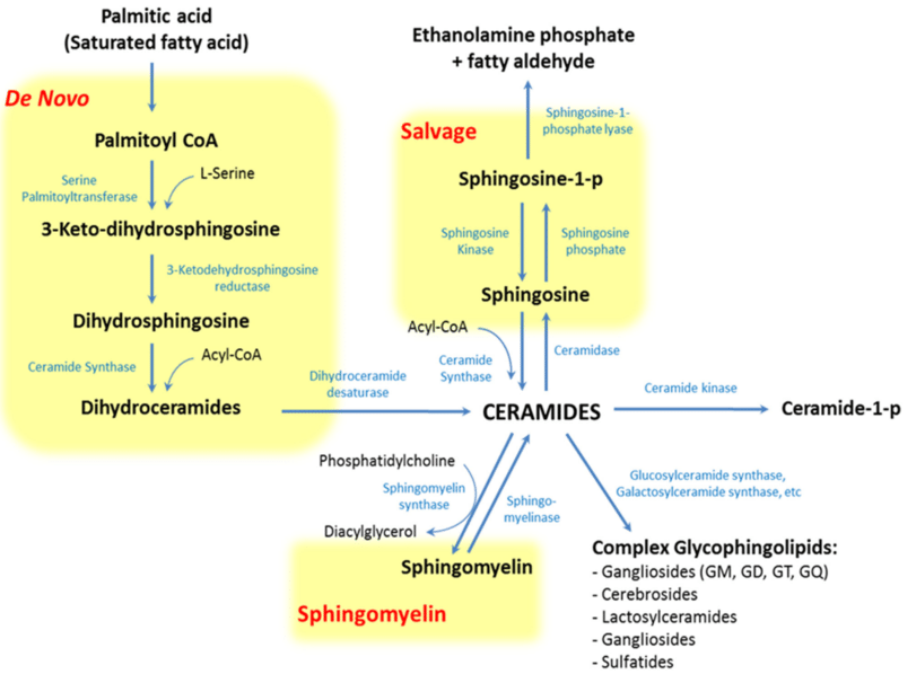

Figure 1.8. The pathways of sphingolipid metabolism. Sphingolipid metabolism primarily consists of three pathways: the *de novo* pathway coming from saturated fatty acids, the salvage pathway and the sphingomyelin pathway, all of which converge in ceramides. Adapted from Frontier in Neuroscience 2016, R. Castillo (*118*).

1.5.2 The role of sphingolipids in muscle and MuSC physiology

Ceramides serve as the hub of sphingolipid metabolism, and were among the first sphingolipids to have their bioactive role characterized (*108*). Increased ceramide levels have been implicated in different complex diseases, ranging from cardiovascular disease (*119*), diabetes (*120*), to Alzheimer's disease (*121*). In spite of advances in understanding the association between increased ceramide levels and diseases, the role of sphingolipids in muscle diseases, such as age-related sarcopenia or muscular dystrophy, remains unproven.

Recently, some groups reported that ceramide is involved in the regulation of myogenic differentiation. The differentiation of short-chain ceramide treated C2C12 myoblasts was noticed to be suppressed (*122*). Moreover, the cellular content of ceramide displayed a decrease during myogenic differentiation. Inhibition of ceramide *de novo* synthesis by the administration of myriocin or fumonisin B1, decreased cellular ceramide levels and enhanced the onset of myogenic differentiation (*123*). However, the current understanding of the role of ceramide in MuSCs regulation is still limited. As the most abundant component in sphingolipid pathway and the precursor of ceramide, sphingomyelin is enriched in plasma membranes of quiescent MuSCs, yet it markedly decreased after the activation of MuSCs (*124*). In addition to sphingomyelin, S1P was also reported to promote the proliferation of MuSCs and therefore to improve muscle regeneration (*125*). The deficiency of S1P is also involved in the pathology of muscular dystrophy, such as DMD (*126*).

1.5.3 Inhibition of sphingolipid *de novo* synthesis

Due to the characterization of most of the enzymes involved in the synthesis and degradation of sphingolipids, specific inhibitors of these enzymes have been developed and utilized to analyze the role of different metabolites within sphingolipid metabolism. Among these inhibitors, myriocin is the most frequently used in academic research.

Myriocin, a fungal metabolite of the Chinese herb *Iscaria sinclarii*, is identified as a potent and highly selective inhibitor of SPT, the first and rate-limiting enzyme in sphingolipid biosynthesis. Initially, myriocin was identified as an antibiotic with an immunosuppressive function (*127*). Since the potential

of myriocin in blocking sphingolipid synthesis has been discovered, it has been employed to treat animal models of different diseases. Available literature has demonstrated that myriocin has produced beneficial effects in mouse models of cardiovascular disease, including atherosclerosis, and myocardial ischemia reperfusion injury (*128, 129*). Other studies have provided evidence that inhibiting *de novo* synthesis of sphingolipids by myriocin improved glucose homeostasis and enhanced whole-body insulin responsiveness in rodent models of type 2 diabetes (*130*). Furthermore, it has been demonstrated that myriocin can reverse hepatic steatosis in diet induced nonalcoholic fatty liver disease (NAFLD) (*131*). In recent studies, myriocin has even been proven to prevent muscle ceramide accumulation during short-term mechanical unloading (*132*), suggesting that myriocin might be capable of rescuing dysfunctional muscles. Despite these advances, the role of sphingolipids in aging and age-related disease has not been addressed. My thesis work provides the first comprehensive characterization of sphingolipid in aging and muscular dystrophies. We have identified novel mechanisms how sphingolipids contribute to aging and muscle disease, and provide evidence how sphingolipid metabolism could be an emerging therapeutic target for pharmacological interventions of age-related muscle diseases.

Chapter 2. Urolithin A improves muscle function by rescuing mitophagy in muscular dystrophy

This part of work has received revision feedback from Science Translational Medicine (STM) and is under preparation to resubmit to STM.

One Sentence Summary:

Mitophagy reverts muscular dystrophies.

Authors:

Peiling Luan[1]†, Davide D'Amico[1,2]†, Penelope A. Andreux[2], Pirkka-Pekka Laurila[1], Martin Wohlwend[1], Chris Rinsch[2], Johan Auwerx[1]*

Affiliation:

[1]Laboratory for Integrative and Systems Physiology, Institute of Bioengineering, Ecole Polytechnique Fédérale de Lausanne (EPFL), CH-1015 Lausanne, Switzerland; [2]Amazentis SA

*Correspondence to Johan Auwerx at admin.auwerx@epfl.ch

† These authors contributed equally to this work.

2.1 Abstract

Duchenne muscular dystrophy (DMD) is the most common muscular dystrophy and despite advances in genetic and pharmacological disease-modifying treatments, its management remains a major challenge. Mitochondrial dysfunction contributes to DMD yet the exact mechanisms by which this occurs remain elusive. Our data in experimental models and patients with DMD show reduced expression of genes involved in mitochondrial autophagy or mitophagy, contributing to mitochondrial dysfunction. Mitophagy markers were not only reduced in skeletal muscle, but also in muscle stem cells (MuSCs) of a mouse model of DMD. Administration of the mitophagy activator, Urolithin A (UA), rescued mitophagy in DMD worms, mice and in primary myoblasts of DMD patients and improved mitochondrial function and MuSCs regenerative ability, resulting in the recovery of muscle function in DMD models. These data indicate that restoration of mitophagy alleviates symptoms of DMD and suggest that UA may have potential therapeutic applications for muscular dystrophies.

2.2 Introduction

Duchenne muscular dystrophy (DMD) is an X-linked recessive disease that affects approximately 1 in 5000 male living births (*133, 134*). DMD is the most frequent muscle disease in children and currently with no cure (*135*). Patients affected by DMD develop progressive muscle weakness in early childhood and have a dramatically reduced lifespan as a consequence of fatal respiratory complications or cardiac failure (*134*). The disease is caused by mutations in the gene encoding for dystrophin, a cytoskeletal protein connecting the muscle fibers to the underlying basal lamina. These mutations cause muscle structural defects, that in turn lead to progressive fiber damage and membrane leakage (*136*). DMD disease progression is also triggered by the reduction of functional muscle stem cells (MuSCs) and their limited ability to regenerate damaged dystrophic muscles (*61*).

Growing evidence suggests that altered mitochondrial function plays a critical role in the pathogenesis of experimental models (*96, 137, 138*) and human patients (*139, 140*) affected by DMD. DMD muscles are typified by reduced mitochondrial respiration (*96, 97*), decreased NAD^+-mediated mitochondrial biogenesis (*97, 141*) and altered organelle localization (*142*). Despite the drastic reduction in mitochondrial function, markers of mitochondrial mass were reported to be only mildly decreased or unchanged (*142, 143*). In addition, mitochondria are significantly larger (*144*) and have reduced membrane potential (*145*) in muscles of DMD compared to control animals. This evidence suggests that mitochondrial dysfunction might not only be caused by reduced *de novo* mitochondrial production, but also by the accumulation of dysfunctional mitochondria that are not properly cleared by mitochondrial autophagy, *i.e.* mitophagy.

Here, we first asked whether defective mitophagy is a marker of DMD. Then, we selectively enhanced mitophagy in worm and mouse models of DMD using Urolithin A (UA), a first-in class activator of mitophagy, tested in both mice (*103*) and humans (*104*). We explored the effects of UA on myofiber metabolism, regenerative ability of MuSCs, and muscle function in animal models of DMD. Mitophagy is tightly coordinated with mitochondrial biogenesis (*146, 147*), and essential for mitochondrial homeostasis in health and several disease conditions (*148*). We hypothesize that reactivating proper levels of mitophagy in dystrophic muscles would remove damaged mitochondria, replenish cells with functional organelles, and alleviate DMD disease symptoms.

2.3 Results

2.3.1 Reduced mitophagy is a hallmark of Duchenne muscular dystrophy

To study the role of mitophagy in the context of muscular dystrophies, we first examined the gene expression levels in skeletal muscle biopsies of patients diagnosed with DMD or Becker Muscular dystrophy (BMD), a genetically similar yet milder disease than DMD (*149*), and compared them to healthy control subjects, focusing on selected genes belonging to the Gene Ontology (GO)-Category “Autophagy of mitochondrion” from the GEO dataset GSE3307 (*150*). Key markers of mitophagy, such as *PINK1*, *PARK2*, *PARK7* and *BNIP3*, were downregulated in dystrophic muscles (Fig. 2. 1A). The reduction in their transcript levels was more pronounced in DMD than BMD patients, suggesting that transcript abundance of genes involved in mitophagy is dose-dependently associated with disease severity. A similar, yet less striking, decrease was observed in mRNA levels of general autophagy genes (Fig. 2. 1A). The expression of mitophagy-related genes was also reduced in skeletal muscle of DMD patients in another dataset comparing controls and DMD patients (fig. 2. S1A, from GSE1004 (*151*)). Furthermore, *DMD* mRNA levels were positively correlated with the expression of mitophagy and some autophagy-related genes (Fig. 2. 1B), including *PINK1*, *PARK2, BNIP3* and *SQSTM1* (Fig. 2. 1C). Interestingly, mitophagy genes were already downregulated in quadriceps biopsies of individuals diagnosed with DMD before the onset of symptoms (0-3 years of age) (Fig. 2. 1D from GSE6011 (*152*)), suggesting that mitophagy is involved in DMD pathogenesis rather than a mere reactive response to disease progression.

Expression of specific mitophagy genes was also reduced in primary myoblast cells derived from DMD patients as compared to those from control subjects (Fig. 2. 1E). Defective mitophagy in DMD *vs* control cells was visible, both in basal condition and upon FCCP-mediated induction of mitophagy, as

assessed by staining against phospho-S65-Ubiquitin (Fig. 2. 1F and fig. 2. S1, B, C), a marker of PINK1-dependent phosphorylation of ubiquitinated mitochondrial proteins (*153*) and by analyzing the levels of mitochondrial phospho-S65-Ubiquitin, PARKIN and BNIP3 (fig. 2. S1D). These data show that defective mitophagy in skeletal muscle is a prevalent feature of human DMD. In addition, compared to healthy individuals, mitophagy markers were also significantly downregulated in other muscle dystrophies and neuromuscular diseases, such as Acute Quadriplegic Myopathy (AQM) and Juvenile Dermatomyositis (JDM) to various extent, suggesting a role for mitophagy in these human disorders as well (fig. 2. S1E).

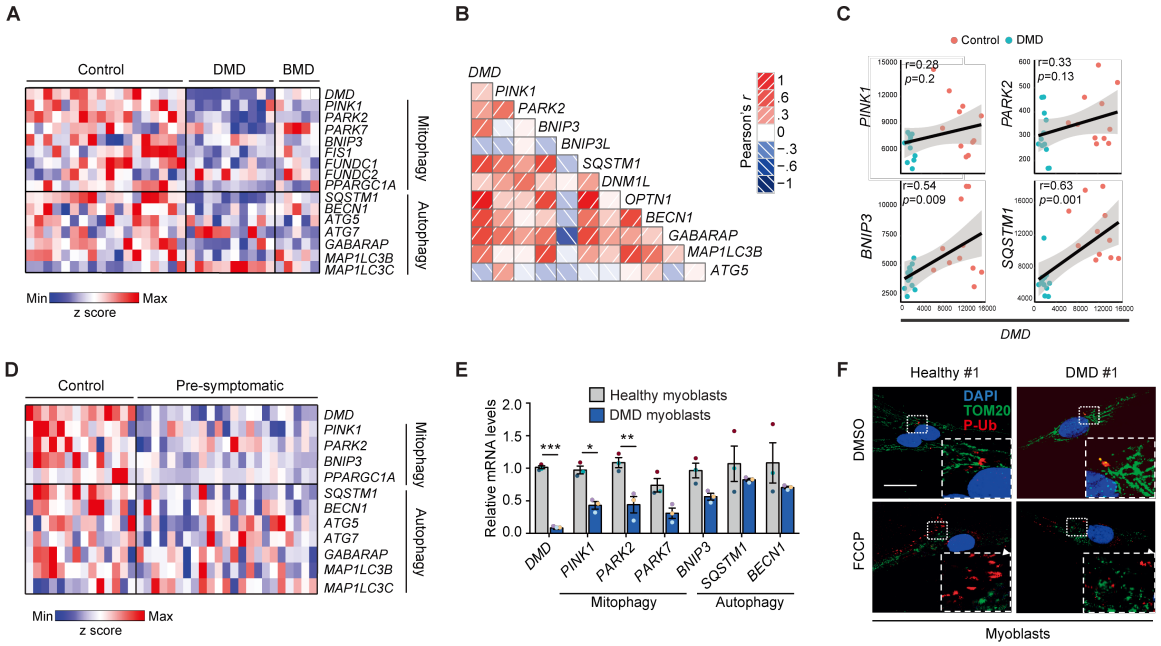

Fig.2.1. Mitophagy is downregulated in human DMD. (**A**) Heatmap showing the expression of mitophagy and autophagy genes manually curated from the GO category "Autophagy of mitochondrion" (GO:0000422) in human controls and patients affected by Duchenne or Becker muscular dystrophy (DMD and BMD, respectively) from the dataset (GSE3307). (**B**) Corrgram indicating Pearson's correlations between the *DMD* gene and the indicated mitophagy/autophagy gene expression, from human muscle biopsies of DMD patients and controls (GSE1004). (**C**) Corresponding correlation analysis of mRNA expression levels of *DMD* and *PINK1*, *PARK2*, *BNIP3* and *SQSTM1*. Controls and DMD patients are represented by red and blue dots, respectively. (**D**) Heatmap, showing the expression levels of the indicated mitophagy and autophagy genes in pre-symptomatic DMD patients (from GSE6011) (n=23). (**E**) mRNA expression levels of the *DMD* gene and of mitophagy (*PINK1, PARK2, PARK7, BNIP3*) and autophagy (*SQSTM1, BECN1*) genes in primary myoblasts from healthy human donors and patients affected by DMD. Dot color indicates different individuals (n = 3). All data are shown as mean ± SEM (error bars). **P* < 0.05; ***P* < 0.01; ****P*< 0.001; by two-way ANOVA. (**F**) Staining of phospho-S65-Ubiquitin, TOM20 and DAPI in primary myoblasts as in Fig.2. 1E, in basal condition or after treatment with FCCP (2h, 10μM). Scale bar =10μm.

2.3.2 UA rescued mitophagy defects and muscle function in *dys-1;hlh-1* mutant *C. elegans*

To study whether impaired mitophagy is characteristic of animal models of DMD, we used *mdx* mouse model and the *C. elegans dys-1;hlh-1* model, lacking the mouse and worm orthologues of the human *DMD* gene, respectively. Consistent with the data in humans, *mdx* mice showed significantly lower levels of mitophagy and some autophagy-related genes (fig. 2. S1F). Likewise, *dys-1;hlh-1* worms expressed lower levels of *pink-1* and *pdr-1* (the orthologues of human genes, *PINK1* and *PARK2*, respectively) with no or modest changes in the expression of autophagy genes, *bec-1* and *vps-34,* compared to wild-type N2 worms (Fig. 2. 2A).

Given the reduction in mitophagy markers, we hypothesized that UA, a natural compound able to stimulate mitophagy in cells, worms and mice (*103, 154*), could restore these mitochondrial defects in DMD. Indeed, UA-treatment of *dys-1;hlh-1* worms increased the expression of *pink-1* and *pdr-1* mitophagy genes to the levels seen in control N2 nematodes, with no significant impact on the expression of autophagy genes (Fig. 2. 2A). The upregulation of mitophagy genes was accompanied by an improvement in mitochondrial network (Fig. 2. 2, B, C and fig. 2. S2A), mitochondrial respiration

(Fig. 2. 2D) and citrate synthase activity (Fig. 2. 2E), demonstrating the ability of UA to reverse the DMD-associated mitochondrial dysfunction. UA had a positive impact on muscle function, as it rescued disease-associated muscle fiber degeneration (Fig. 2. 2F and fig. 2. S2B) and increased the motility of the dystrophic worms (Fig. 2. 2G). Of note, this UA-mediated increase in fitness was abolished upon silencing of either *pink-1* (Fig. 2. 2H) or *pdr-1* (fig. 2. S2C), demonstrating that UA-dependent beneficial effects are mediated by mitophagy.

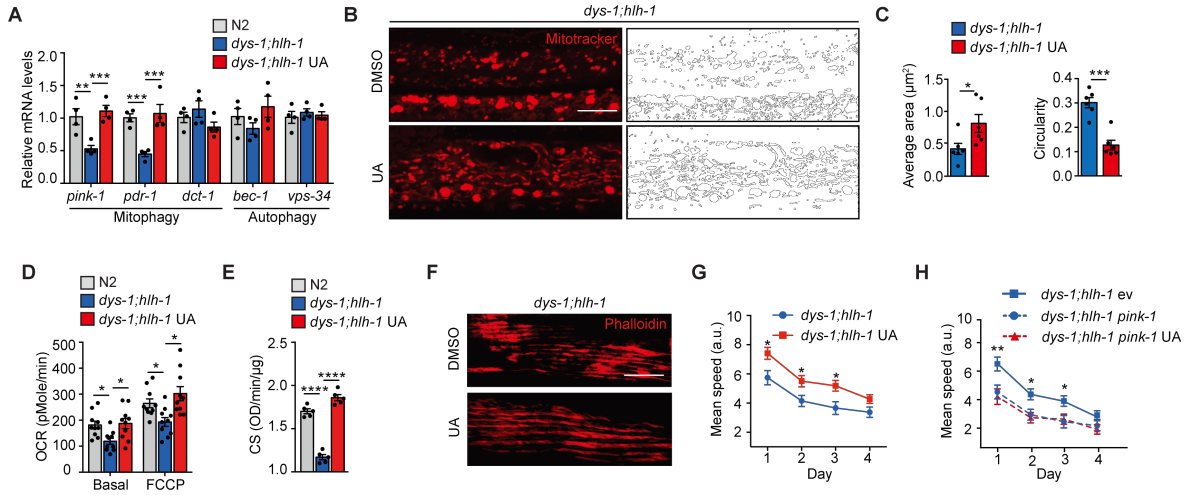

Fig.2.2. UA treatment rescued mitophagy, mitochondrial and muscle functions in *C. elegans* model of DMD. (**A**) mRNA levels of mitophagy (*pink-1, pdr-1, dct-1*) and autophagy (*bec-1, vsp-34*) genes in N2 and *dys-1;hlh-1* treated with DMSO or UA (25µM) since the maternal L4 stage (n=4). $^{**}P \leq 0.01$, $^{***}P \leq 0.001$; by two-way ANOVA test. (**B**) Mitotracker red staining and corresponding mitochondrial network contour of *dys-1;hlh-1* strain worms, exposed to DMSO or UA (25µM) to assess mitochondrial morphology. Scale bar = 20µm. (**C**) Scoring of mitochondrial morphology of six worms based on average area of the mitochondrial network and on the circularity assessment, where 1=perfect circle and 0=line (n=6 worms). $^{*}P \leq 0.05$, $^{**}P \leq 0.01$, $^{***}P \leq 0.001$; by two-tailed t-test. (**D,E**) Oxygen consumption rate at basal and maximal level (FCCP, 2µM) (n=10) (**D**) and citrate synthase activity (n=5) (**E**), in *dys-1;hlh-1* worms treated as in Fig. 2. 2A. $^{*}P \leq 0.05$, $^{****}P \leq 0.0001$; by two-way ANOVA for Fig. 2. 2D and one-way ANOVA test for Fig. 2. 2E. (**F**) Muscle fibers stained by rhodamine-coupled phalloidin (n=6) of worms treated as in Fig. 2. 2B. Scale bar = 20µm. (**G,H**) Motility of vehicle- and UA-treated *dys-1;hlh-1* worms, from day 1 to day 4 of adulthood (n=40-60 worms per experiment) (**G**) and of *dys-1;hlh-1* fed with either empty vector as control or with *pink-1* RNAi and treated with UA (25µM) or DMSO as indicated (**H**). $^{*}P \leq 0.05$, $^{**}P \leq 0.01$; by two-way ANOVA test.

2.3.3 UA restored mitophagy and mitochondrial function in *mdx* mice muscle

To test whether UA induces mitophagy in a mammalian DMD model, we treated *mdx* mice with UA supplemented in diet (50mpk/d) for 10 weeks. Wild-type BL10 mice were used as controls (Fig. 2. S3A). Similar to what we observed in *C. elegans*, UA increased the expression of mitophagy related genes, and to a lesser extent, of autophagy transcripts in the forelimb muscle of *mdx* mice (Fig. 2. 3A). To confirm UA-mediated mitophagy in *mdx* mice, we isolated mitochondrial fractions from skeletal muscles. Compared to controls, *mdx* mice showed reduced levels of mitochondrial phospho-S65-Ubiquitin, PARKIN and BNIP3 that were increased with UA treatment (Fig. 2. 3B). Autophagy was activated in *mdx* mice, as shown by the increased LC3-II/LC3-I ratio (fig. 2. S3B), supporting the presence of compensatory effects or of stalled autophagy during muscular dystrophy (*155, 156*). However, UA was not able to further induce autophagy in the *mdx* mice (fig. 2. S3B), highlighting its specific effect on mitophagy in this particular context. UA-treatment led to increased ATP levels (fig. 2. S3C), and to robust elevation of citrate synthase activity (Fig. 2. 3C), a marker of mitochondrial function. UA induced mitophagy also in myoblast cells from human DMD patients, as evidenced by increased expression of mitophagy genes (Fig. 2. 3D) and phospho-S65-Ubiquitin signal (Fig. 2. 3, E, F and fig. 2. S3D), implying that UA might also have beneficial effects on human DMD.

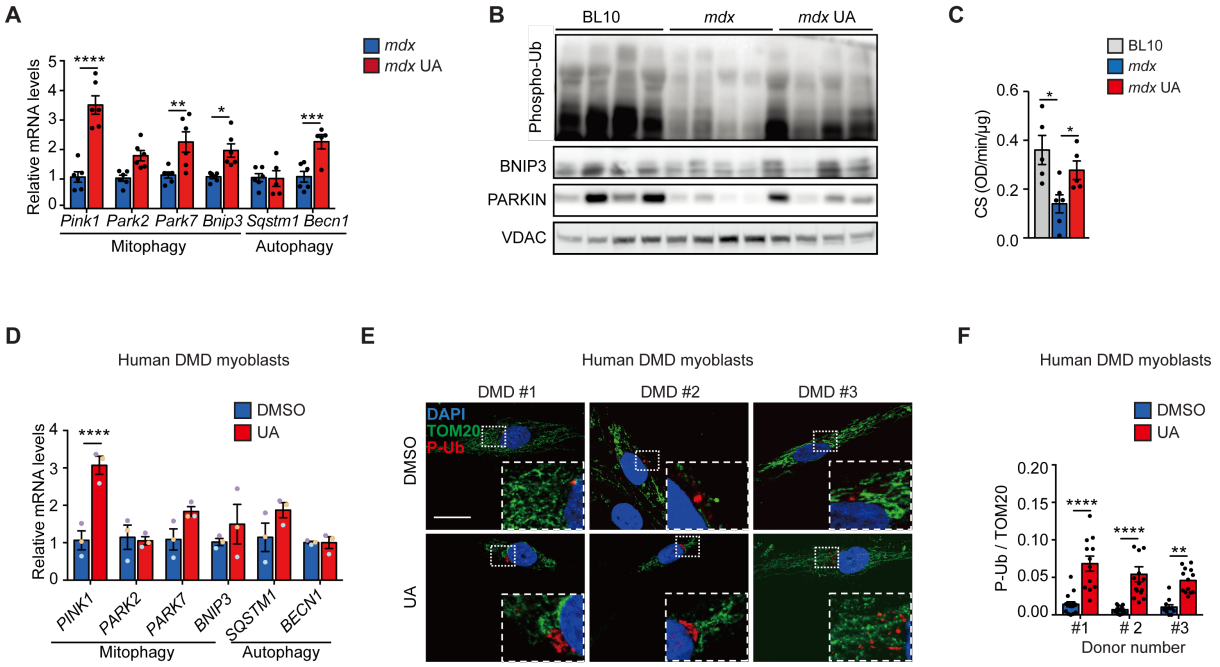

Fig.2.3. UA treatment rescued mitophagy, mitochondrial and muscle functions in mice models of DMD. (**A**) mRNA levels of mitophagy (*Pink1, Park2, Park7, Bnip3*) and autophagy (*Sqstm1, Becn1*) genes from forelimbs of *mdx* mice treated with or without UA (50mpk/d) for 10 weeks. (n=6). *$P \leq 0.05$, **$P \leq 0.01$, ***$P \leq 0.001$, ****$P \leq 0.0001$; by two-way ANOVA test. (**B,C**) Western blot of mitochondrial phospho-S65-Ubiquitin, BNIP3, PARKIN and VDAC as loading control (n=4) (**B**), and citrate synthase activity (n=5) (**C**) of mice treated as in Fig. 2. 3A. BL10 mice were as controls. * P ⩽ 0.05; by one-way ANOVA test. (**D**) Transcript levels of mitophagy (*PINK1, PARK2, PARK7, BNIP3*) and autophagy (*SQSTM1, BECN1*) genes in human myoblasts derived from DMD patients treated with DMSO or UA (25µm, 24h) (n=3). Dot color indicates different individuals. ****P ⩽ 0.0001； by two-way ANOVA. (**E**) Representative images of DMD patients-derived myoblast cells treated as in Fig. 2. 3D, stained against phospho-S65-Ubiquitin, TOM20 and DAPI. Scale bar = 10µm. (**F**) Corresponding quantification of the fluorescent signal in myoblasts from Fig. 2. 3E. **P ⩽ 0.01, ****P ⩽ 0.0001； by two-way ANOVA.

2.3.4 UA enhanced both mitophagy and regenerative ability of muscle stem cells in *mdx* mice

Muscle stem cells (MuSCs) are capable of giving rise to mature muscle cells, and they manifest considerable variation in mitochondrial function in different physiological conditions (*105, 157*). FACS-purified MuSCs from *mdx* mice expressed reduced levels of the mitophagy markers *Pink1*, *Park2*, *Park7* and *Bnip3* compared to control MuSCs (Fig.2. 4A). Conversely, UA-treatment of *mdx* mice reestablished the expression levels of these mitophagy genes to physiological levels in MuSCs (Fig. 2. 4A). In DMD, MuSCs have lower proliferative potential, which leads to progressive MuSCs exhaustion (*27, 158*). UA reverted this phenotype, by increasing the expression of the stemness marker, *Pax7,* and of the early myogenic marker, *Myod*, while at the same time decreasing the levels of the differentiation marker, *Myog,* and of the cyclin-dependent kinase inhibitor and senescence activator, *p21,* in MuSCs of dystrophic animals (Fig. 2. 4B). A similar induction of PAX7 and MYOD and reduction of MYOG expression was present at the protein level in human myoblasts treated with UA (Fig. 2. 4C). These data support the hypothesis that UA links enhanced mitophagy to MuSCs activation.

In line with this rationale, UA-treated *mdx* mice had more MuSCs, *in vivo*, as measured both by PAX7 immunostaining (fig. 2. S4A) and by FACS of $Lin^{-}Sca\text{-}1^{-}VCAM^{+}$ cells normalized to muscle weight (Fig. 2. 4D). The increase in MuSCs number was also observed *ex vivo* in single muscle fibers isolated from *mdx* mice and treated with UA for 24 hours (fig. 2. S4, B, C). To validate the effects of UA on MuSCs function during muscle regeneration, MuSCs isolated from UA-treated and control aged C57BL/6JRj mice were transplanted into cardiotoxin (CTX) damaged *mdx* mice (fig. 2. S4D). Seven and fourteen days after transplantation, mice receiving UA-treated MuSCs had reduced muscle inflammation (Fig. 2. 4, E, F and fig. 2. S4E), increased average cross section area (CSA) of muscle fibers (Fig. 2. 4G) and higher levels of eMyHC (Fig. 2. 4, H, I and fig. 2. S4F), a marker of regenerative capacity, and of dystrophin (Fig. 2. 4, J, K and fig. 2. S4G). Such changes are reflective of enhanced muscle

regeneration. In summary, these data unveil a novel function of UA in regulating MuSCs function, in addition to its known effects on terminally differentiated muscle fibers.

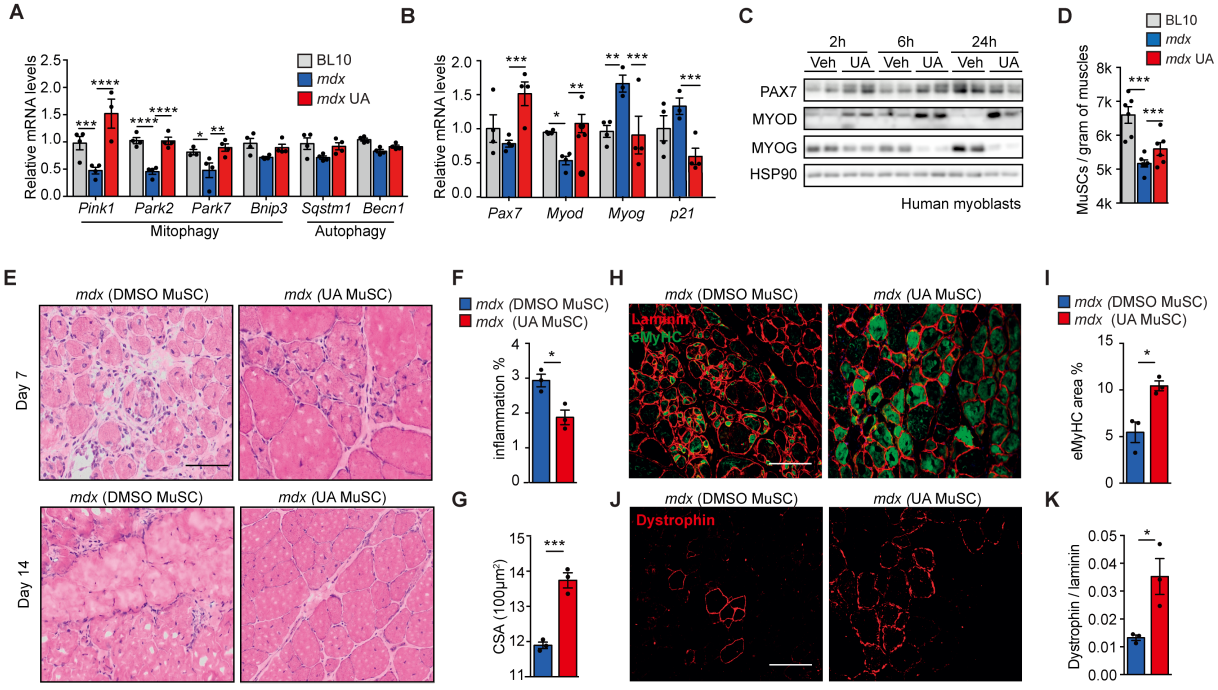

Fig.2.4. UA induced mitophagy and mitochondrial function in muscle stem cells (MuSCs) of *mdx* mice. (**A**) Transcript levels of mitophagy (*Pink1, Park2, Park7, Bnip3*) and autophagy (*Sqstm1, Becn1*) genes in MuSCs isolated from hindlimbs of BL10, as control, and *mdx* mice untreated or treated with UA (50mpk/d) for 10 weeks (n=4). *$P \leq 0.05$, **$P \leq 0.01$, ***$P \leq 0.001$, ****$P \leq 0.0001$; by two-way ANOVA test. (**B**) mRNA expression of stemness (*Pax7*, *Myod*), differentiation (*Myog*) and senescence (*p21*) markers in MuSCs from mice treated as above (n=4). *$P \leq 0.05$, **$P \leq 0.01$, ***$P \leq 0.001$; by two-way ANOVA. (**C**) Western blot of PAX7, MYOG, MYOD, and HSP90 (as loading control) in human primary myoblasts treated with DMSO or UA (25µM) at the indicated times (n=2). (**D**) FACS-based quantification of freshly isolated MuSCs from hindlimb muscles of *mdx* or BL10 mice treated as in Fig. 2. 4A, normalized to the weight of hindlimb muscles (n=6). ***$P \leq 0.001$; by one-way ANOVA. (**E**) H&E staining in TA muscle sections of *mdx* mice receiving stem cells from control untreated donors or UA-treated donors treated with UA at 50mpk/d, 7 and 14 days after transplantation. Scale bar = 50µm. (**F,G**) Quantification of the inflammation area (**F**) and average cross sectional area (CSA) of muscle fibers (**G**) in sections from mice sacrificed 7 days after MuSCs transplantation. *$P < 0.05$; ***$P \leq 0.001$; by two-tailed t-test. (**H**) Immunostaining images and (**I**) corresponding quantification of eMyHC signal in mice treated as in Fig. 2. 4E. Scale bar = 50µm. *$P < 0.05$; by two-tailed t-test. (**J**) Immunostaining images and (**K**) corresponding quantification of the dystrophin signal normalized to laminin in mice treated as in Fig. 2. 4E. Scale bar = 50µm. *$P < 0.05$; by two-tailed t-test.

2.3.5 UA improved myocellular quality and muscle function in *mdx* mice

Finally, we investigated whether the molecular and cellular effects of UA had an impact on the clinical features of DMD. UA-treatment (50mpk/d) of 3-weeks-old *mdx* mice reduced the number of inflammatory cells in muscle, as demonstrated by decreased signal of the general immune cell marker CD45 (Fig. 2. 5, A, B and fig. 2. S5A). UA increased the expression of the structural proteins, α-dystrobrevin (α-DB) and β-dystroglycan (β-DG), indicating that UA promotes the maintenance of proper muscle morphology (Fig. 2. 5, C, D). Muscle integrity, a characteristic feature of dystrophic muscles, was reverted by UA treatment, as reflected by reduced permeability of Evans blue in the gastrocnemius and quadriceps muscles (Fig. 2. 5, E, F and fig. 2. S5B). Fibrosis of the diaphragm, which contributes to respiratory failure in the majority of DMD patients, was diminished after UA supplementation in *mdx* mice (Fig. 2. 5, G, H and fig. 2. S5C). Furthermore, UA reduced the levels of creatine kinase in both untrained (fig. 2. S5D) and post-trained (Fig. 2. 5I) *mdx* animals, reflecting its protective effect against muscle damage. The muscle fiber CSA was increased in UA treated *mdx* mice (fig. 2. S5E), and this enhanced muscle fiber size continued to show uniformity as manifested by the distribution of minimal Feret diameter (fig. 2. S5F). The UA-treated *mdx* mice also had a lower percentage of fibers with centralized nuclei in the tibialis anterior (TA) muscles (Fig. 2. 5J). Finally, UA significantly improved both grip strength (Fig. 2. 5K) and running performance (Fig. 2. 5L) of *mdx* mice, demonstrating its ability to reverse DMD-associated muscle dysfunction.

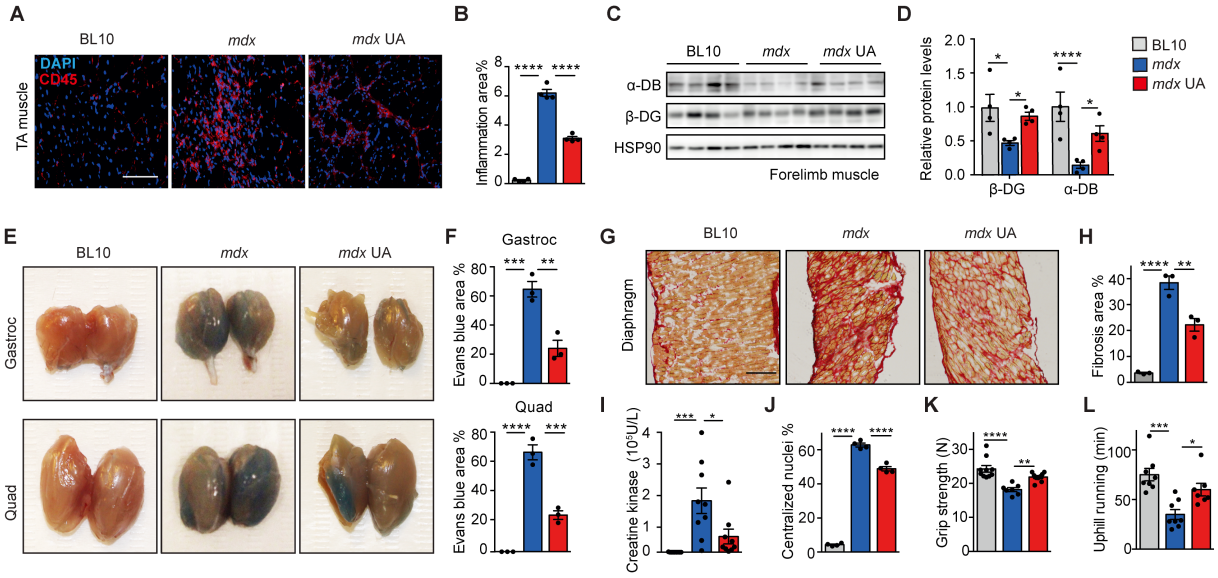

Fig.2.5. UA reduced muscle damage and recovered muscle function in *mdx* mice. (**A,B**) CD45 staining of infiltrated inflammatory cells in TA muscles of BL10 and *mdx* mice treated with vehicle (DMSO) or with UA (50mpk/d) for 10 weeks. Representative images (**A**) and corresponding quantification (**B**) (n=4). ****$P \leq 0.0001$; by one-way ANOVA test. Scale bar = 50μm. (**C,D**) Western blot of the structural proteins, α-dystrobrevin (α-DB) and β-dystroglycan (β-DG), from forelimb muscles in the mice used in Fig. 2. 5A (**C**) and corresponding quantification of protein levels (**D**) (n=4) *$P \leq 0.05$, ****P ≤ 0.0001; by two-way ANOVA. (**E,F**) Evans blue staining of quadriceps and gastrocnemius muscles of mice treated as in Fig. 2. 5A (**E**) and corresponding quantification (**F**) (n=3). **$P \leq 0.01$, ***$P \leq 0.001$, ****$P \leq 0.0001$; by one-way ANOVA test. (**G,H**) Representative images of picrosirius red staining of the diaphragms, showing fibrosis of the diaphragm, in the indicated mouse cohorts (**G**) and corresponding quantification of the area of fibrosis (**H**) (n=3). **$P \leq 0.01$, ****$P \leq 0.0001$; by one-way ANOVA test. Scale bar = 200μm. (**I**) Plasma creatine kinase levels in post-exercised (downhill running) mice treated as in Fig. 2. 5A. (n=8-10). *$P \leq 0.05$, ***$P \leq 0.001$; by one-way ANOVA test. (**J**) Percentage of muscle fibers with centralized nuclei in TA muscles of mice as in Fig. 2. 5A (n=4). ****P ≤ 0.0001; by one-way ANOVA test. (**K**,**L**) Grip strength (**K**) and uphill running ability (**L**) of mice treated as in Fig. 2. 5A (n=7-10). *P ⩽ 0.05, **P ⩽ 0.01, ***P ⩽ 0.001，****P ⩽ 0.0001; by one-way ANOVA test.

2.4 Discussion

Our data show that defective mitophagy is a common feature of DMD in both experimental models of the disease and in human DMD patients, in line with previous reports analyzing mitophagy in the muscle (*159*) and heart (*155*) of dystrophic mice.

Muscle dystrophies are characterized by a dysregulation of general autophagy (*156, 160*) and several publications suggests the use of autophagy inducers to treat these disorders (*156, 159, 161, 162*). However, both our data and previous works show that autophagy markers are reduced only in late stages of DMD and are induced in the early stages of the disease (*156*). This supports the notion that autophagy contributes to the initial compensatory phase of the disease (*156*) and might work better mostly as disease-modifying agent during DMD late stages.

We show that mitophagy declines in human patients already during early stages of DMD, suggesting that dysfunctional mitophagy contributes to DMD pathogenesis prior to the manifestation of severe phenotypes. We propose that reverting mitophagy defects could be an efficient approach to restore mitochondrial function and slow down DMD symptoms. Strategies to boost mitophagy were recently shown to improve muscle dysfunction in aging and other degenerative disorders (*97, 163-165*), supporting our hypothesis. To test our model, we treated DMD worms and mice with the mitophagy enhancer UA. UA is a natural, microflora-derived, metabolite shown to stimulate mitophagy and improve muscle health in preclinical models of aging (*97*). Here, we provide evidence that UA rescues mitochondrial and muscle defects also in dystrophic animals. A randomized, double-blind, placebo-controlled clinical study shows that UA supplementation in healthy elderly is safe, bioavailable and induces a molecular signature of improved mitochondrial and cellular health (*104*). This evidence implies translational potential of UA in humans.

The present study indicates that mitophagy is reduced not only in differentiated muscle fibers but also in MuSCs of DMD mouse models. Defective mitochondrial clearance was already reported in aged

MuSCs (*105, 157*) and other stem cell types (*86, 105, 166, 167*), but not in MuSCs of DMD. Importantly, UA-treatment of *mdx* mice rescues MuSCs mitophagy levels and increases their regenerative ability. This evidence is relevant in the context of muscular dystrophies, since the onset of these diseases is linked with the exhaustion of the pool of functional MuSCs (*27, 168*).

Gene and cell-based therapies hold great promise to target some upstream DMD genetic defects, by editing and correcting the mutated dystrophin gene or mRNA (*169*). However, these tools still have low targeting efficiency and can correct only one or a subset of mutations at the time (*170, 171*). Moreover, it is still unclear whether correcting the primary disease-causing mutation is sufficient to revert pathogenic secondary symptoms, such as mitochondrial dysfunction (*172*). Combination therapies are hence proposed to optimize the treatment efficacy (*173*) and further studies would be relevant to test the synergistic effect of combined UA and gene/cell-based treatment.

In summary, our data provide evidence that UA, a natural compound with proven biosafety (*104, 174*), restores mitophagy in DMD models, and suggests mitophagy boosting to be a potential treatment strategy, alone and/or in combination with other therapies, for DMD and other muscular dystrophies.

2.5 Materials and Methods

***C. elegans* strains and RNAi experiments.**
C. elegans strains were cultured at 16 °C on nematode growth media agar plates seeded with *E. coli* strain OP50 unless stated otherwise. Strains used in this study are wild-type N2 and *dys-1;hlh-1*. Strains were provided by the Caenorhabditis Genetics Center (University of Minnesota). Bacterial feeding RNAi experiments were carried out as described (*175*). Clones used were *pdr-1* (K08E3.7), *pink-1* (EEED8.9) and were purchased from GeneService and sequenced before use.

Pharmacological treatment of *C. elegans*.
Urolithin A (3,8-dihydroxy-6H-dibenzo[b,d]pyran-6-one; UA) was provided by Amazentis SA, and added at 25 μM just before pouring the plates. Parental F0 L4 worms were allowed to reach adulthood and lay eggs on the treatment plates. The derived F1 worms were therefore exposed to the compound during the full life from eggs until death. To ensure a permanent exposure to the compound, plates were changed twice a week. UA was dissolved in a DMSO stock solution. The control population was treated with the corresponding concentration of DMSO at 1% final.

Oxygen-consumption and mobility assays.
C. elegans movement was performed as described (*176*). The experiment was repeated at least twice. Oxygen consumption was measured using the Seahorse XF96 equipment (Seahorse Bioscience) as described (*175, 177*). Each well contained 10 worms and respiration rates were calculated as average values of 5 repeated measurements. Each experiment was repeated at least twice.

Mitotracker imaging of *C. elegans*.
For each experimental condition, a population of 20 worms at L4 stage was transferred on plates containing MitoTracker Red CMTMRos (Thermo Scientific) at a final concentration of 2μg μl^{-1}. Plates were incubated at 16 °C and after 24 h worms were collected and washed in 200μl of M9 buffer in order to remove the residual bacteria. Worms were then incubated for 30 min on regular NGM plates at 16°C and mounted on an agar pad for imaging by confocal microscopy. For each condition, up to 20 worms were observed and imaged. Tracing of the mitochondrial network contour was done by the use of Gaussian blur filter followed by the application of Laplacian operator. Image processing was performed with the Fiji software Mito-Morphology (http://imagej.nih.gov/ij; version 1.47b). Each experiment was repeated at least twice.

Phalloidin staining of *C. elegans*.
For phalloidin staining, a population of 20 L4 worms was washed in M9 and frozen in liquid nitrogen, subsequently, they were lyophilized using a centrifugal evaporator and permeabilized using acetone. 2U of phalloidin (Thermo Scientific) was resuspended in 20μl of a buffer containing Na-phosphate pH 7.5 (final concentration 0.2 mM), $MgCl_2$ (final concentration 1 mM), SDS (final concentration 0.004%) and dH_2O to volume. The worms were incubated for 1 h in the dark and then washed twice with PBS. Following the immobilization, worms were observed using confocal laser microscopy.

Mouse studies.
UA was admixed to CD (Research Diet 3242) at a dose of 50mpk/d. Pellets with or without UA were given to 3-week-old male C57BL/10ScSn or C57BL/10ScSn-Dmd^{mdx}J mice (Janvier) for 10 weeks. A total of 30 mice were housed by groups of 4 or 5 animals per cage and randomized to 10 animals per group according to their body weight and composition. Body composition was assessed by EchoMRI before and after the treatment. Muscle strength was assessed by a grip strength behavior task. The grasp strength of each mouse for all four limbs was measured on a pull-grid assembly connected to a grip strength meter (Columbus Instruments). The mouse was drawn along a straight line parallel to the grid until the grip was broken, providing the peak force in grams. This was repeated 3 times with 5 min intervals between measurements. Exercise capacity was assessed after 7 weeks of treatment by monitoring the running distance on uphill treadmill. The exercise regimen commenced at a speed of 9 cm/s with an inclination of 5 degrees. The speed was gradually increased 3 cm/s every 12 min. Mice were considered to be exhausted and removed from the treadmill, following the accumulation of 5 or more shocks (0.1mA) per min for two consecutive minutes. The distance traveled and time before exhaustion were registered as maximal running distance and period. Downhill running was performed 9 weeks after treatment. Mice began the exercise at a speed of 15 cm/s with a declination of 5°. The

speed gradually increased after each period of 12 minutes of racing by 3cm/s. The duration of each step of this protocol was 1 min. The distance traveled and the number of shocks received over 1 min intervals were registered. All mice were set to run for 90 min except if a mouse got 5 shocks (0.1mA) during two consecutive steps, which was considered exhausted and withdrawn from the experience. Mice were familiarized with the treadmill one day before recording the running activity. Animals were killed after 10 weeks of treatment after an overnight fasting. Experiments were authorized by the Veterinary office of the Canton of Vaud, Switzerland (authorization no. 2890). Animals that showed signs of severity predefined by the animal authorization no. 2890 were euthanized. These animals, together with those who died spontaneously during the experiments, were excluded from the calculations. These criteria were established before starting the experiments.

Creatine kinase.
Creatine kinase was measured on plasma collected before and after downhill running using the Creatine Kinase Flex Reagent Cartridge (Siemens Healthcare Diagnostics AG) on the Dimension Xpand Plus Instrument (Siemens Healthcare Diagnostics AG).

Human cells.
Primary human myoblast cells derived from three male healthy individuals and three male DMD patients were provided by Hospices Civils de Lyon. The three DMD patients and healthy individuals were all from 4- to 7-year-old-males. The human myoblast cells used in Fig. 3C were from a 20-year-old male and were provided by Lonza. Cells were cultured in F-10 medium supplemented with 12% FBS and penicillin/streptomycin. Cells were treated with 25 μM UA for 2, 6 and 24 hours or FCCP for 2 h.

Bioinformatic analysis.
Heatmaps were obtained using the heatmap2 function of R/gplots. The correlogram was obtained using the corrgram function of R/corrgram. Pearson's r was used to establish correlations between *DMD* and either *PINK1, PARK2, BNIP3* or *SQSTM1* mRNA levels in muscle biopsies from the GEO dataset GSE1004 and gene expression was normalized using MAS5 normalization algorithm.

Quantification of ATP levels and citrate synthase enzymatic activity.
Total ATP content and citrate synthase (CS) enzymatic activity of the forelimbs from treated mice were measured as described (39). Total ATP content was measured by the CellTiter-Glo luminescent cell viability assay (Promega), and CS was determined using the CS assay kit (Sigma). Each experiment was repeated twice and normalized to protein quantity.

Extraction of mRNA for quantitative real-time PCR.
For *C. elegans,* a total of ≈1000 worms per conditions were manually recovered from 15 NGM plates and split into three biological replicates. Each experiment was repeated twice. Total RNA was extracted from MuSCs by sorting cells directly into TriPure RNA isolation reagent (Roche) or from cultured primary human myoblasts, *C. elegans* or mouse muscle tissue using TriPure reagent according to the product manual. Total RNA was transcribed to cDNA using QuantiTect Reverse Transcription Kit (Qiagen). Expression of selected genes was analyzed using the LightCycler480 system (Roche) and LightCycler® 480 SYBR Green I Master reagent (Roche).

FACS analysis.
Gastrocnemius, soleus, quadriceps, and tibialis anterior (TA) muscles from both hindlimbs were excised and transferred into PBS on ice. All muscles were trimmed, minced and digested with 0.1mg/ml of type II collagenase (Sigma) in PBS for 1 h at 37°C. Samples were then centrifuged at 750 *g* for 5 min and further digested in 1 mg/ml of collagenase/dispase (Roche) for 1 hour at 37°C. Muscle slurries were sequentially filtered through 100 and 40 μm cell strainers. The isolated cells were then washed in washing buffer (PBS + 2.5% FBS) then resuspended in 200 μl of washing buffer and immediately stained with antibodies, including CD31 (1:800, eBioscience, eFluor450 conjugated); CD45 (1:200, eBioscience, eFluor450 conjugated); Sca-1 (1:1000, eBioscience, PE-Cy7 conjugated); and VCAM-1 (1:200, MBL) for 40 min at 4°C. Secondary staining was performed with propidium iodide (PI, Sigma) for 15 min at 4°C in the dark. Stained cells were analyzed and sorted using the FACS Aria II instrument (BD Biosciences). Debris and dead cells were excluded by forward scatter, side scatter and PI gating.

Single muscle fiber isolation.
Single fiber isolation was performed as described (*178*). Myofibers were isolated from TA and extensor digitorum longus (EDL) muscles with a glass pipet in DMEM with 2% L-Glutamine, 4.5% glucose containing 20% FBS and then cultured at 37°C in 24-well plates containing DMEM supplemented with 2% L-glutamine, 4.5% glucose, 20% FBS, 1% chick embryo extract and 1% penicillin/streptomycin. After 24 hours, the medium was supplemented with either UA (25 μM) or 1% DMSO. 24 h later fibers were washed with PBS, fixed using 4% PFA for 15 min and permeabilized in 0.5% Triton-X100 for 15 min. Fibers were blocked in PBS containing 10% BSA for 30 min. Fibers were incubated in primary antibodies PAX7 (DSHB, University of Iowa) diluted in blocking solution overnight at 4°C. Samples were subsequently washed with PBS and stained with secondary antibody (Alexa fluor) together with DAPI for 1 hour at room temperature. Samples were washed in PBS and mounted with Dako mounting medium prior imaging with the ZEISS DMI4000 microscope.

Cardiotoxin-induced muscle damage and MuSCs transplantation.
mdx mice were anesthetized using isoflurane in oxygen from a precision vaporizer. 50 µl of 20 µM Naje mossambica mossambica cardiotoxin (CTX) (Latoxan) was injected intramuscularly into TA muscle. 24 h after CTX injection, equal amount of MuSCs isolated from 20-month-old C57BL/6JRj mice treated with UA (50mpk/d) for 10 weeks, were injected intramuscularly into the TA muscle of 12-month-old *mdx* mice. Recipient mice were sacrificed at 7 and 14 days after injury. TA muscles were immediately embedded in Thermo Scientific™ Shandon™ Cryomatrix™ and frozen in isopentane, cooled in liquid nitrogen, for 2 min before being transferred to dry ice and stored at -80°C.

Histology.
Histological specimens were prepared and analyzed as described (*105*). Muscle integrity was assessed with 1% solution of Evans blue dye (EBD), which was injected into the peritoneal cavity, using 1% volume to body weight, 24 hours before sacrifice. EBD was dissolved in phosphate-buffered saline (PBS) [0.15 M NaCl, 10 mM phosphate buffer (pH 7.4)] and sterilized by passage through membrane filters with a 0.2 µm pore size. Upon sacrifice, the hind leg skin of the mice was removed, and the animals were photographed for dye uptake into skeletal muscles, indicated by blue coloration. Muscle sections from EBD-injected animals were then incubated in 4% PFA at -20°C for 15 min, washed three times for 10 min with PBS, counterstained with DAPI, laminin (1:200, Sigma), CD45 (1:100, eBioscience), dystrophin (1:100, Spring Bioscience) or eMyHC (1:50, DSHB, University of Iowa) and mounted with Dako Mounting Medium. Microscopy images of red emission fluorescence from EBD-positive muscle fibers were analyzed using the ImageJ software. Centralized nuclei percent, minimal Feret diameter and cross-sectional area in TA muscles were determined using the ImageJ software quantification of laminin and DAPI-stained muscle images from VS120-S6-W slides scanner (Olympus). A minimum of 2000 fibers were used for each condition and measurement. The minimal Feret diameter is defined as the minimum distance between two parallel tangents at opposing borders of the muscle fiber. This measure has been found to be resistant to deviations away from the optimal cross-sectioning profile during the sectioning process.

For immunofluorescence, cells were fixed with 4% PFA for 15 min, permeabilized with 0.25% Triton X-100 for 10 min and blocked with PBS containing 10% BSA for 30 min. Samples were stained using the primary antibodies targeting Phospho-S65-ubiquitin (Millipore, ABS1513-I 1:200) and TOMM20 (Santa Cruz sc-11415, 1:50). Quantification of phospho-S65-ubiquitin signal by calculating the area percent normalized to the TOM20 signal. All samples were imaged with a ZEISS LSM 700 UP. Images were analyzed using ImageJ software. For immunofluorescence quantification, positively stained cells were defined as those with an intensity that was higher than a given threshold, which was then applied to all images. Thresholds were set up using sample slides before analyzing experimental data.

Mitochondria isolation and western blotting.
Mouse forelimb muscles were placed in homogenizer glass-Teflon potter tubes with 5 ml of a buffer prepared by adding 10 ml of 0.1 M Tris–MOPS and 1 ml of EGTA-Tris to 20 ml of 1 M sucrose and bringing the volume to 100 ml with distilled water. Homogenization was performed at 280 *g* for 5 min. The samples were then centrifuged for 10 min at 600 *g* and the supernatants were collected. A second centrifugation at 7,000*g* for 10 min was performed on the supernatants in order to precipitate the mitochondrial fraction. All steps were performed on ice or at 4 °C. The resulting samples were lysed in lysis buffer [50 mM tris (pH 7.4), 150 mM KCl, 1 mM EDTA, 1% NP-40, 5 mM NAM, 1 mM sodium

butyrate, protease inhibitors]. Proteins were separated by SDS-PAGE and transferred onto nitrocellulose or polyvinylidene difluoride membranes. Blocking and antibody incubations were performed in 5% milk solution except Phospho-S65-ubiquitin was diluted in 5% BSA. Primary antibodies applied: Phospho-S65-ubiquitin (Millipore ABS1513-I), BNIP3 (Cell Signaling 3769 and Abcam ab8399), PARKIN (Cell Signaling 4211), HSP90 (Cell Signaling 4874), PAX7 (DSHB, University of Iowa), MOYD (Santa-Cruz SC-377460), MYOG (Santa Cruz SC-12732) LC3I/II (Cell Signaling 4108S), β-dystroglycan (Santa Cruz sc-33702), α-dystrobrevin (Santa Cruz sc-13812), VDAC (Abcam, ab14734). Antibody detection reactions were developed by enhanced chemiluminescence (Advansta) using x-ray films or imaged using the c300 imaging system (Azure Biosystems).

Statistics.
Differences between two groups were assessed using two-tailed *t*-test. Differences between more than two groups were assessed using one-way analysis of variance (ANOVA). To compare the interaction between two factors, two-way ANOVA tests were performed. GraphPad Prism 6 was used for all statistical analyses. All *P* values <0.05 were considered significant. *$P \leq 0.05$, **$P \leq 0.01$, and ***$P \leq 0.001$, ****$P \leq 0.0001$.

2.6 Acknowledgements

We thank the team of the Phenotyping Unit, Center of PhenoGenomics, School of Life Sciences, Ecole Polytechnique Fédérale de Lausanne (EPFL) for their technical and scientific expertise in the mouse experiments. Work in the Auwerx laboratory is supported by the Ecole Polytechnique Fédérale de Lausanne, the Fondation Marcel Levaillant, the Swiss Foundation for Research on Muscle Diseases (FSRMM) and was co-financed by the Commission for Technology and Innovation (CTI) (15171.1 PFLS-LS).

2.7 Supplementary Materials

Fig. 2. S1: Mitophagy is downregulated in human and mouse DMD and in other neuromuscular dystrophies.

Fig. 2. S2: UA recovers mitophagy, mitochondrial and muscle morphology in DMD worm models.

Fig. 2. S3: UA activates mitophagy and enhances mitochondrial functions in human and mouse DMD models.

Fig. 2. S4: UA induces mitophagy, mitochondrial function and regenerative ability in MuSCs from *mdx* mice.

Fig. 2. S5: UA reduces muscle damage and ameliorated DMD symptoms in *mdx* mice.

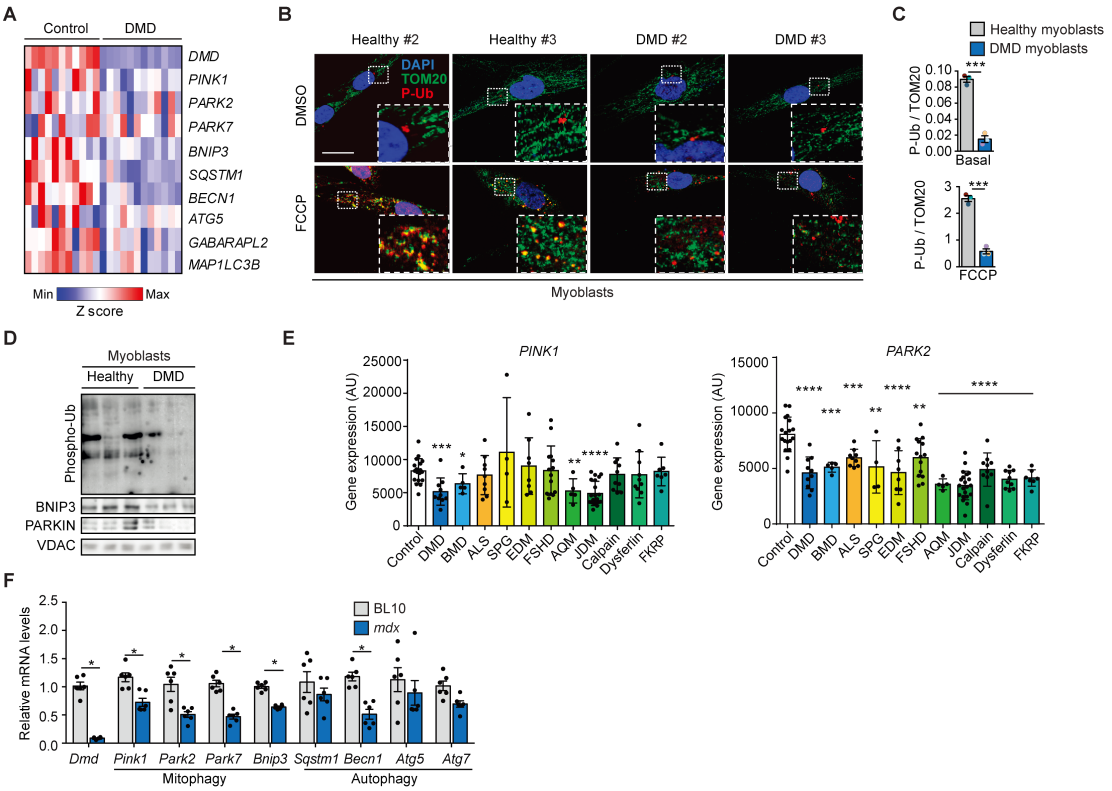

Fig. 2. S1. Mitophagy is downregulated in human and mouse DMD and in other neuromuscular dystrophies. (**A**) Heatmap showing the expression of DMD and selected mitophagy and autophagy genes from the GO category "Autophagy of mitochondrion" (GO:0000422) in human controls and patients affected by Duchenne muscular dystrophy (DMD) from the dataset GSE1004. (**B**) Staining of phospho-S65-Ubiquitin, TOM20 and DAPI of primary myoblasts as in Fig. 2. 1F, in basal condition or after treatment with FCCP (2h, 10μM). Scale bar = 10μm. (**C**) Corresponding quantification of phospho-S65-Ubiquitin normalized to TOM20 signal in basal condition (top) and upon FCCP-treatment (bottom). ***P ⩽ 0.001; by two-tailed t-test. (**D**) Western blot of mitochondrial fractions showing phospho-S65-Ubiquitin, BNIP3, PARKIN and VDAC as loading control, of myoblast cells derived from healthy individuals and DMD patients as in Fig. 2. 1E (n=3). (**E**) mRNA expression levels of *PINK1* and *PARK2* in healthy individuals and patients affected by different neuromuscular diseases from GSE3307. ALS (amyotrophic lateral sclerosis), SPG (spastic paraplegia), EDM (Emery-Dreifuss dystrophy), FSHD (facioscapulohumeral muscular dystrophy), AQM (acute quadriplegic myopathy), JDM (Juvenile Dermatomyositis), Calpain (calpain-related disease), Dysferlin (dysferlinopathy) and FKRP (FKRP-related myopathies). *P ⩽ 0.05, **P ⩽ 0.01, ***P ⩽ 0.001, ****P ⩽ 0.0001; by two-tailed t-test. (**F**) mRNA expression levels of the *Dmd* gene and of mitophagy (*Pink1, Park2, Park7, Bnip3*) and autophagy (*Sqstm1, Becn1, Atg5, Atg7*) genes in forelimbs from 13-weeks-old BL10 control and *mdx* mice. All data are shown as mean ± SEM (error bars). *P < 0.05; by two-way ANOVA.

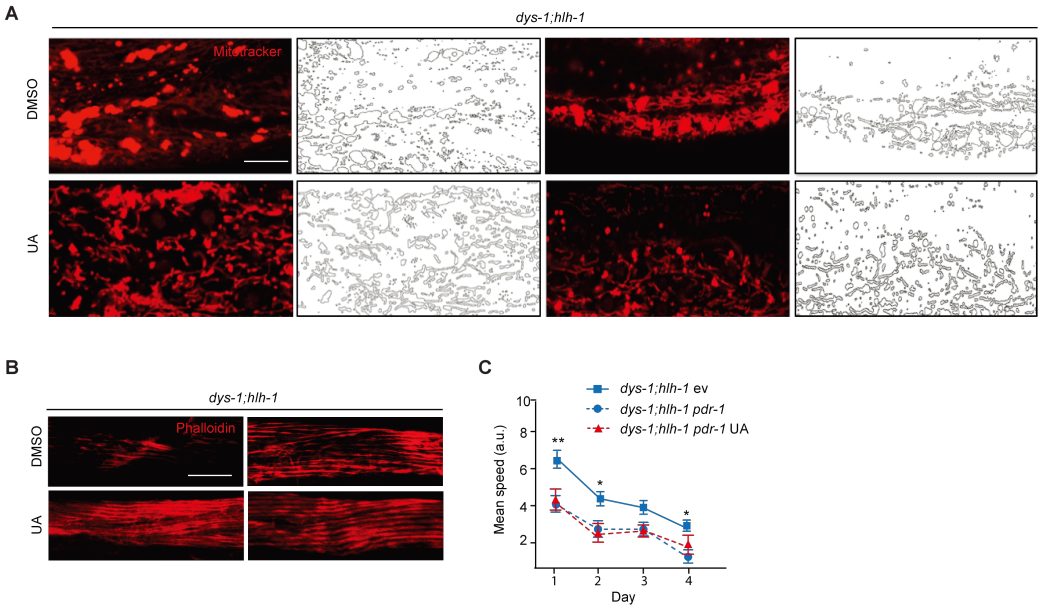

Fig. 2. S2. UA recovered mitophagy, mitochondrial and muscle morphology in DMD worm models. (**A**) Mitotracker red staining and corresponding mitochondrial network contour of *dys-1;hlh-1* strain worms, exposed to DMSO or UA (25μM) to assess mitochondrial morphology, as in Fig. 2. 2B. Scale bar = 20μm. (**B**) Muscle fibers stained by rhodamine-coupled phalloidin (n=6) of worms treated as in Fig. 2. S2A. Scale bar = 20μm. (**C**) Motility of *dys-1;hlh-1* fed with either empty vector as control or with *pdr-1* RNAi and treated with UA or DMSO as indicated. **P* ≤ 0.05, ***P* ≤ 0.01; by two-way ANOVA test.

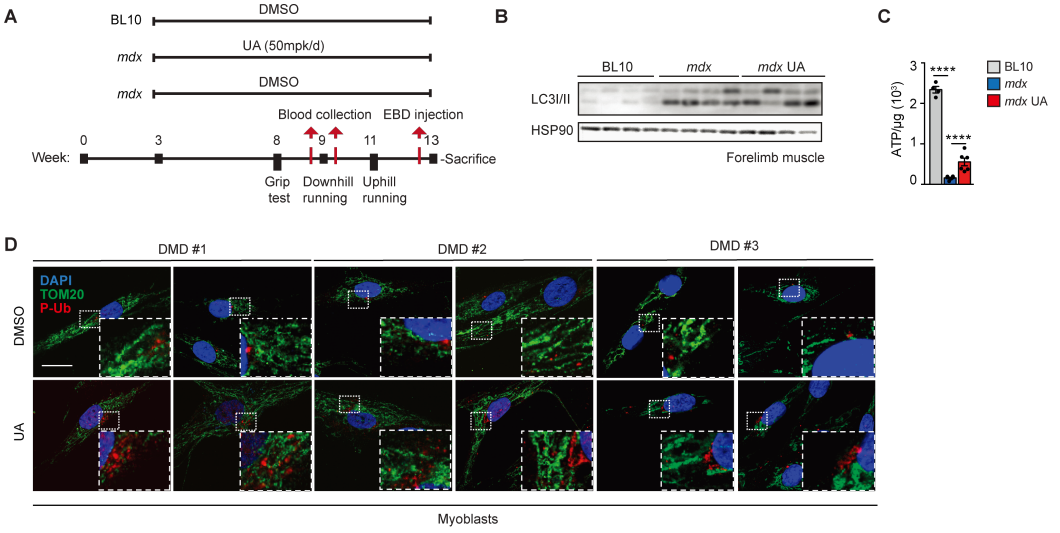

Fig. 2. S3. UA activated mitophagy and enhanced mitochondrial functions in human and mouse DMD models. **(A)** Summary of the mouse study on control BL10 and *mdx* mice including dosage and duration of UA-treatment and phenotyping pipeline. EBD = Evans blue dye. (**B**) Western blot analysis of LC3I/II and HSP90 (as loading control) of forelimb muscles from BL10 and *mdx* mice treated as shown in fig. 2. S3A. (**C**) ATP level of forelimb muscles of BL10 and *mdx* mice treated as shown in fig. 2. S3A. *****P* ≤ 0.0001; by one-way ANOVA test. (**D**) Representative images of human myoblasts derived from three different DMD patients (#1, #2 and #3), treated with DMSO or UA (25μM) and stained for phospho-S65-Ubiquitin, TOM20 and DAPI, as in Fig. 2. 3E. Scale bar = 10μm.

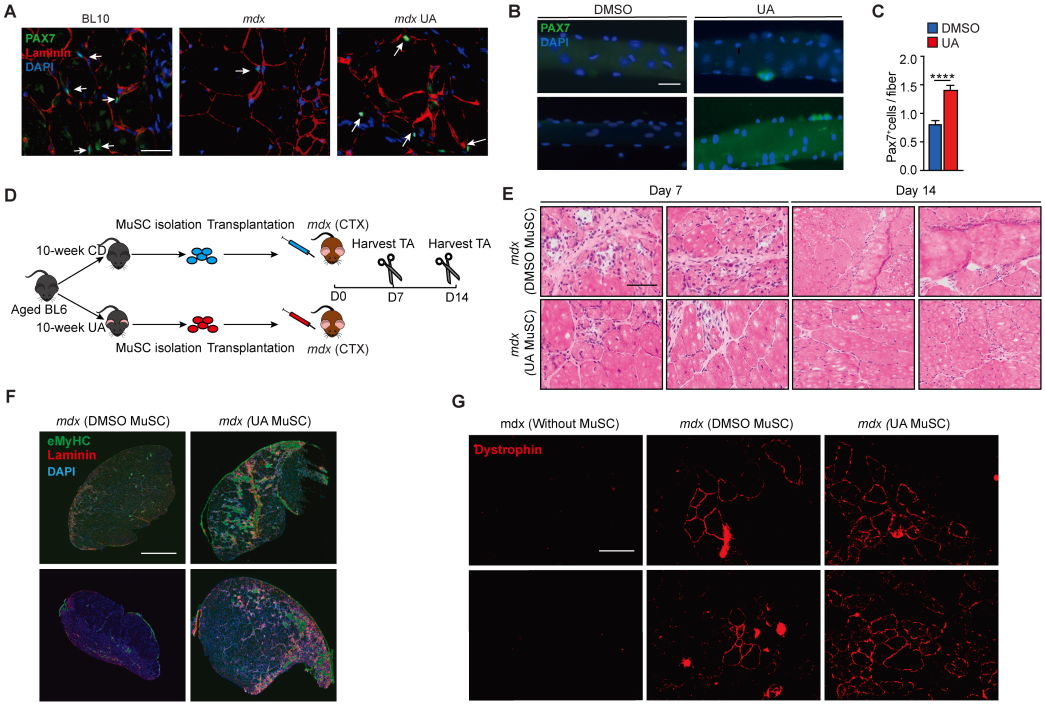

Fig. 2. S4. UA induced mitophagy, mitochondrial function and regenerative ability in MuSCs from *mdx* mice. (**A**) PAX7, laminin and DAPI staining in TA muscles of BL10 and *mdx* mice treated as shown in fig. 2. S3A. White arrows indicate $PAX7^{+}DAPI^{+}$ MuSCs. Scale bar = 50μm. (**B, C**) Single muscle fibers isolated from *mdx* mice and treated, *ex vivo*, with UA (25μM) or vehicle for 24h and stained against PAX7. Nuclei counterstained with DAPI. Scale bar = 20μm. Representative images (**B**) and corresponding quantification of MuSCs number per fiber (**C**). Number of fibers quantified = 50. ****$P \leqslant 0.0001$; by two-tailed t-test (n=50). (**D**) Timeline of MuSCs transplantation assay. MuSCs were sorted from control and UA-treated C57BL/6 aged mice respectively and transplanted into CTX-damaged TA muscles of 1-year old recipient *mdx* mice. Seven and fourteen days after MuSCs transplantation, TA muscles were harvested from the *mdx* mice for histological analysis. (**E, F, G**) Representative images of H&E (**E**), eMyHC and laminin (**F**) and dystrophin (**G**) stainings in TA muscles from recipient *mdx* mice sacrificed seven days after MuSCs transplantation. Scale bar = 250μm for fig. 2. S4F and scale bar = 50μm for fig. 2. S4E, G.

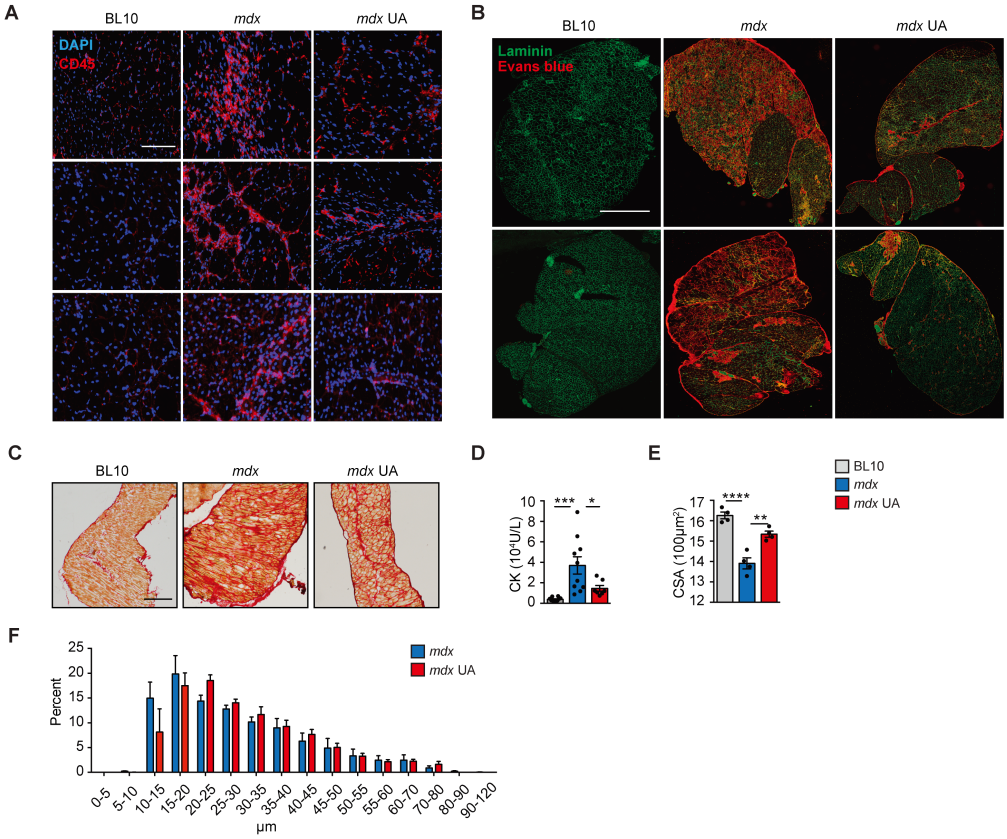

Fig. 2. S5. UA reduced muscle damage and ameliorated DMD symptoms in *mdx* mice. (**A**) Representative images of CD45- and DAPI-stained immune cells in TA muscles of BL10 and *mdx* mice treated with or without UA as in Fig. 2. 5A. Scale bar = 50μm. (**B**) Sections of whole gastrocnemius muscles of BL10 and *mdx* mice treated as in Fig. 2. 5A showing Evans blue dye (red) and counterstained for laminin (green). Scale bar = 200μm. (**C**) Representative images of diaphragms from BL10 and *mdx* mice treated as in Fig. 2. 5A, stained with picrosirius red. Scale bar = 200μm. (**D**) Pre-exercise (downhill running) creatine kinase levels of BL10 and *mdx* mice treated as in Fig. 2. 5A (n = 8-10). $*P \leq 0.05$, $***P \leq 0.001$ by one-way ANOVA test. (**E,F**) Average cross sectional area (CSA) of TA muscle fibers (**E**) and distribution of muscle fiber minimal Feret diameter (**F**) of mice treated as in Fig. 2. 5A (n=3).

Chapter 3. Sphingolipid depletion reverses age-associated sarcopenia and improves muscle regeneration

This part of work has been submitted to Nature Medicine and is under revision.

Pirkka-Pekka Laurila[1], Peiling Luan[1], Martin Wohlwend[1], Maroun Bou-Sleiman[1], Johanna Tuhkanen[2], Sèbastien Herzig[1], Michal K. Handzlik[3], Eleonora Porcu[4,5], Davide D'Amico[1], Nadège Zanou[6], Minna Salonen[7], Zoltan Kutalik[4,8], Nicolas Place[6], Christian M. Metallo[3], Thomas O. Eichmann[9,10], Jari Lahti[2,11], Johan G. Eriksson[12,13,14], Johan Auwerx[1]

1. Laboratory of Integrative Systems Physiology, École polytechnique fédérale de Lausanne (EPFL), Lausanne, Switzerland
2. Department of Psychology and Logopedics, University of Helsinki, Helsinki, Finland
3. Department of Bioengineering, University of California, San Diego, La Jolla, CA 92093, USA
4. Swiss Institute of Bioinformatics, Lausanne, Switzerland
5. Center for Integrative Genomics, University of Lausanne, Lausanne, Switzerland
6. Institute of Sport Sciences, Department of Physiology, Faculty of Biology-Medicine, University of Lausanne, Lausanne, Switzerland
7. Chronic Disease Prevention Unit, National Institute for Health and Welfare, Helsinki, Finland
8. University Center for Primary Care and Public Health, University of Lausanne, Lausanne, Switzerland
9. Institute of Molecular Biosciences, University of Graz, Graz, Austria
10. Center for Explorative Lipidomics, BioTechMed-Graz, Graz, Austria
11. Turku Institute for Advanced Studies, University of Turku, Turku, Finland
12. Department of General Practice and Primary Health Care, University of Helsinki and Helsinki University Hospital, PO Box 20, 00014 University of Helsinki, Finland
13. Folkhälsan Research Center, University of Helsinki, PO Box 20, 00014 University of Helsinki
14. National University Singapore, Yong Loo Lin School of Medicine, Department of Obstetrics and Gynecology, Singapore, SG

Correspondence to Johan Auwerx, admin.auwerx@epfl.ch

3.1 ABSTRACT

Sarcopenia, the loss of muscle mass and function, is a major cause of physical incapacitation in elderly, and currently lacks viable treatment strategies. Here we report the involvement of sphingolipids in aging and sarcopenia. Sphingolipids accumulate in skeletal muscle upon aging, and pharmacological inhibition of sphingolipid synthesis prevents age-related decline in muscle mass and function, enhancing exercise capacity and muscle strength. Sphingolipid depletion confers muscle stem cells increased regenerative capacity, priming them to repair injury in aged muscle. In human and mouse myoblasts, inhibition of sphingolipid synthesis activates the myogenic program, leading to hypertrophic myotubes. The relevance of sphingolipid depletion in human aging is demonstrated in the Helsinki Birth Cohort Study in which genetic variants associated with lower expression of genes encoding sphingolipid synthesizing enzymes confer increased fitness to 70-year-old individuals. These findings identify sphingolipid depletion as an attractive therapeutic strategy for age-related sarcopenia and co-occurring pathologies.

3.2 INTRODUCTION

Healthy aging, defined as 'freedom from disease or disease-disability, high cognitive and physical functioning, and active engagement with life (*179*),' will remain the major goal of the public health sector due to the aging of the population, with the proportion of individuals aged 60 years or older expected to rise to 22% in the next four decades (*180*). This goal is encumbered by multimorbidity, the coexistence of 2 or more chronic conditions, such as diabetes, cardiovascular and neurodegenerative diseases, whose prevalence is increased upon aging (*181*). During the course of these diseases, there is a significant rise in the incidence of a common debilitating comorbidity, sarcopenia.

Sarcopenia, the decline of skeletal muscle mass with age, is one of the most important causes of functional decline and loss of independence in aged individuals (*182*). Sarcopenia is considered a component of the frailty syndrome (*182*), an even more accurate predictor of all-cause mortality than age alone (*183*). Pre-sarcopenia is characterized by low muscle mass; sarcopenia with low muscle strength or low physical performance in addition to low muscle mass; and severe sarcopenia encompasses all three criteria (*182*). The loss of muscle mass in sarcopenia has been thought to arise from blunted synthetic response to feeding and exercise (*184*). In addition, upon aging, skeletal muscle becomes depleted of muscle stem cells (MuSCs) (*185*), and muscle regeneration is impaired (*186*). Other triggers of sarcopenia are thought to include mitochondrial abnormalities, hormonal changes, loss of neuromuscular junctions, and activation of inflammatory pathways (*182*). Several pharmacological approaches have been proposed to slow the onset of sarcopenia, such as treatment with sex hormones, including testosterone, and growth hormone, but since the results from these trials have been variable and only marginally effective (*187*), there is an urgent need for new therapeutic strategies. As patients with sarcopenia frequently have multiple comorbidities (*188*) and take several medications (*189*), optimal treatment strategies for sarcopenia would also be effective on coexisting conditions to reduce the burden of polypharmacy.

Sphingolipids are bioactive lipids participating in diverse cellular functions such as inflammation, proliferation, cell growth, and cell death (*108*). Ceramides serve as the hub of sphingolipid metabolism, and were among the first sphingolipids to have their bioactive role characterized (*108*). Increased ceramide levels have been implicated in many complex diseases, including cardiovascular disease (*119*), diabetes (*190*), and Alzheimer's disease (*121*), and in recent years, attention has increasingly focused on inhibiting ceramide generation *in vivo* to combat metabolic disease. Inhibition of serine-palmitoyl transferase (SPT), the first and rate-limiting enzyme of sphingolipid *de novo* biosynthesis pathway, leads to reduced atherosclerosis (*129*), improved glucose tolerance (*191*), and fatty liver (*192*) in mouse models. Mice deficient of ceramide synthase 6 (CERS6) are protected from glucose intolerance (*193, 194*), and the inhibition of dihydroceramide desaturase (DEGS1) was recently reported to improve glucose homeostasis and liver fat accumulation (*195*). While the emerging role of sphingolipid depletion in the treatment of metabolic disorders has been under intensified research efforts (*196, 197*) with pharmacologic inhibition of CERS1 observed to produce beneficial effects (*198*), the role of sphingolipids in aging and sarcopenia, despite their frequent co-occurrence with metabolic disease, has remained unproven.

In the present study, we establish the link between sphingolipid metabolism and sarcopenia. We show that ceramides accumulate in skeletal muscle upon aging, and that pharmacological inhibition of sphingolipid *de novo* biosynthesis pathway by myriocin counteracts age-related loss in muscle mass and function in mice. Systemic inhibition of sphingolipid synthesis leads to elevated MuSC count, accompanied by higher MuSC regenerative capacity. The effects of sphingolipid depletion on muscle differentiation are cell-autonomous, demonstrated by sphingolipid depletion triggering a muscle differentiation program in freshly isolated MuSCs *ex vivo* as well as in mouse and human myoblasts. We demonstrate the relevance of the sphingolipid synthesis in human aging by showing that genetic variants associated with decreased transcript abundance of serine palmitoyltransferase, are associated with improved fitness and muscle function in elderly individuals. Our findings implicate sphingolipid *de novo*

biosynthesis inhibition as a novel therapeutic strategy for age-associated sarcopenia. Given the diverse cellular functions of ceramides and involvement in multiple diseases (*108*), treatment of many diseases by targeting only one biological pathway presents an attractive therapeutic strategy to combat age-related multimorbidity.

3.3 RESULTS

3.3.1 Ceramides accumulate in skeletal muscle upon aging

Sphingolipid *de novo* synthesis pathway produces ceramides and other sphingolipids by using fatty acids and amino acids as substrates (Figure 3. 1a). SPT converts L-serine and palmitoyl-CoA to 3-ketosphinganine, which is rapidly converted to sphinganine. Coupling of sphinganine to long-chain fatty acid is accomplished by one of 6 distinct mammalian ceramide synthases of which *CERS2* is the most abundant in skeletal muscle (Figure 3. 1b). To study how aging affects the sphingolipid *de novo* synthesis pathway *in vivo*, we compared total ceramide content of different organs in young (2-month-old) and aged (2-year-old) mice. Upon aging, we observed a decrease of ceramides in the liver, no change in brain, and an increase in skeletal muscle (Figure 3. 1c). Given that the effects of modulating ceramide quantity and quality in liver are established (*195, 199*), we here focused on skeletal muscle sphingolipids and potential benefits upon their reduction.

The trend of age-dependent increase in skeletal muscle ceramides was global, comprising ceramide species with different acyl lengths (Figure 3. 1d). The most pronounced increase upon aging was observed for Cer(d18:1/24:1), and the most abundant ceramide in muscle, Cer(d18:1/18:0), displayed a 20% increase upon aging (Figure 3. 1d). Differences in skeletal muscle sphingomyelin (SM), a sphingolipid consisting of phosphocholine and ceramide, were less consistent between young and aged mice (Figure 3. S1a-b). Deoxysphingolipids are synthesized by SPT through conjugation of L-alanine rather than L-serine with fatty acid, and have been implicated in disease conditions, such as diabetes (*200*). Similar to canonical sphingolipids, there was a trend of deoxysphinganine (doxSA) accumulation in skeletal muscle upon aging (Figure 3. S1c).

We next compared transcript abundance of the enzymes of sphingolipid *de novo* biosynthesis pathway between young and aged human individuals in a publicly available dataset (GSE25941). Consistent with increased muscle ceramides, many transcripts of these enzymes were upregulated upon aging, including *SPTLC1*, *KDSR*, *CERS2*, and *CERS5* (Figure 3. 1e). The only down-regulated enzyme was *CERS1* (Figure 3. 1e) whose expression is relatively low in skeletal muscle in human Genotype-Tissue Expression (GTEx) database (Figure 3. 1b). In general, there was a strong positive correlation between different transcripts of the sphingolipid *de novo* biosynthesis pathway in post-mortem skeletal muscle biopsies in human GTEx dataset (n=491) (Figure 3. 1f). Only *CERS1* transcript displayed a negative correlation with the other enzymes. Similarly, in the mouse BXD strains (*201*), a recombinant inbred mouse population with substantial genetic heterogeneity, the transcripts were directly correlated with each other (Figure 3. 1g). These results suggest that sphingolipid *de novo* biosynthesis pathway is under tightly coordinated transcriptional control.

Following the strong correlations between transcripts of the pathway, we conducted principal component analysis of the sphingolipid *de novo* biosynthesis pathway in humans (Figure 3. 1h) and mice (Figure 3. S1d-f). The first principal component of the expression of different enzymes of the sphingolipid *de novo* synthesis pathway (*SphPC1*) explained 30.6% of the variance in human skeletal muscle expression (Figure 3. 1i). Of the transcripts of the pathway, *SPTLC1* contributed the most, accounting for 21% of *SphPC1* variability (Figure 3. 1j). In the BXD mouse reference population we observed negative correlation between *SphPC1* and both gastrocnemius and soleus muscle masses, as well as performance on a treadmill and maximal aerobic capacity (Figure 3. 1k). The expression of *Sptlc1* in skeletal muscle showed

similar correlations with these phenotypes (Figure 3. 1l). These findings demonstrate that the expression of sphingolipid *de novo* biosynthesis is inversely correlated with muscle mass and function, and suggest its involvement in sarcopenia.

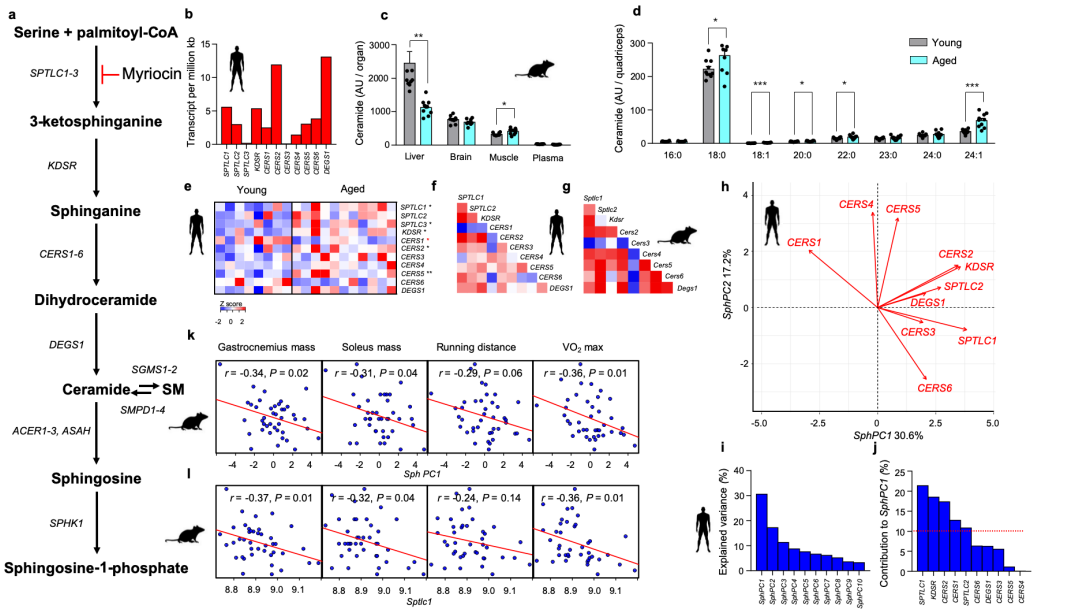

Figure 3. 1. Sphingolipid *de novo* synthesis is activated upon aging in skeletal muscle. (**a**) Scheme of the sphingolipid *de novo* synthesis pathway. (**b**) Transcript abundance of enzymes of sphingolipid *de novo* synthesis pathway in human skeletal muscle from individuals in the Gene-Tissue Expression (GTEx) project (n=491). (**c**) Total ceramide levels in liver, brain, skeletal muscle, and plasma of young (8-week old, n=10) and aged (24-month-old, n=10) C57BL/6JRj mice. (**d**) Concentrations of individual ceramide species in mouse quadriceps muscle. (**e**) Transcript abundance of enzymes of sphingolipid *de novo* synthesis pathway in skeletal muscle of young and aged individuals. (**f**) Correlation of transcripts of sphingolipid *de novo* synthesis pathway in human skeletal muscle (GTEx, n=491). (**g**) Correlation of transcripts of sphingolipid *de novo* synthesis pathway in skeletal muscle of 42 genetically diverse BXD strains. (**h**) A factor loading plot (biplot) showing the effects of the enzymes of sphingolipid *de novo* synthesis pathway on two first principal components (*SphPC1* and *SphPC2*) in human skeletal muscle (GTEx). (**i**) Proportion of variance explained by each principal component of the sphingolipid *de novo* synthesis pathway. (**j**) Contribution of each transcript to the *SphPC1* in human skeletal muscle (GTEx). (**k**) Correlation of *SphPC1* in skeletal muscle with measurements of muscle mass and function in BXD mice. (**l**) Correlation of *Sptlc1* in skeletal muscle with measurements of muscle mass and function in BXD mice. All data are shown mean ± SEM. **P* < 0.05, ***P* < 0.01, and ****P* < 0.001 with Student's two-tailed T test.

3.3.2 Inhibition of sphingolipid *de novo* synthesis prevents loss of muscle mass and function in aging

To examine whether a causal relationship could underlie the correlation between *SphPC1* and muscle mass and function, we tested whether inhibition of sphingolipid *de novo* biosynthesis pathway could protect against age-related muscle dysfunction. We treated aged (18-month-old) chow fed C57Bl/6JRj mice for 5 months with myriocin, a specific inhibitor of SPT, the first and rate-limiting enzyme of the sphingolipid *de novo* synthesis pathway, and whose expression in skeletal muscle was negatively correlated with muscular fitness in BXDs (Figure 3. 1l). Myriocin treatment reduced total ceramide content of skeletal muscle (Figure 3. 2a) as well as individual ceramide species in a global fashion (Figure 3. 2b), confirming the efficacy of the compound in skeletal muscle. In addition to ceramides, myriocin reduced skeletal muscle deoxysphingolipid contents, yet with smaller effect than L-serine derived canonical sphingolipids (Figure 3. S1c). Myriocin did not affect concentrations of brain, liver, or plasma sphingolipids nor muscle sphingomyelins (Figure 3. 2a, Figure 3. S1g-h).

Importantly, myriocin improved the body composition of aged mice. Myriocin delayed age-dependent decline in lean body mass (Figure 3. 2c), and increased muscle mass. Myriocin treated mice displayed greater gastrocnemius and TA mass than DMSO treated

controls (Figure 3. 2d). Improved muscle morphology was evident in histological analysis of tibialis anterior (TA) muscles of myriocin treated mice (Figure 3. 2e), manifested by reduced number of centralized nuclei (Figure 3. 2f), a hallmark of muscle aging (*202*), and larger cross-sectional area of muscle fibers (Figure 3. 2g-i). Myriocin also counteracted age-related muscle dysfunction. Aged mice treated with myriocin demonstrated improved exercise performance and muscle strength, evidenced by the increased running distance and time on a treadmill (Figure 3. 2j), improved aerobic capacity (Figure 3. 2k), and grip strength (Figure 3. 2l). Myriocin treated mice also displayed better muscle coordination, as shown by their improved performance in the rotarod test (Figure 3. 2m), and faster crossing of a beam (Figure 3. 2n). Overall, myriocin treatment improved muscle morphology and counteracted age-related loss of muscle mass, strength, endurance, and coordination, indicating protection against age-related sarcopenia.

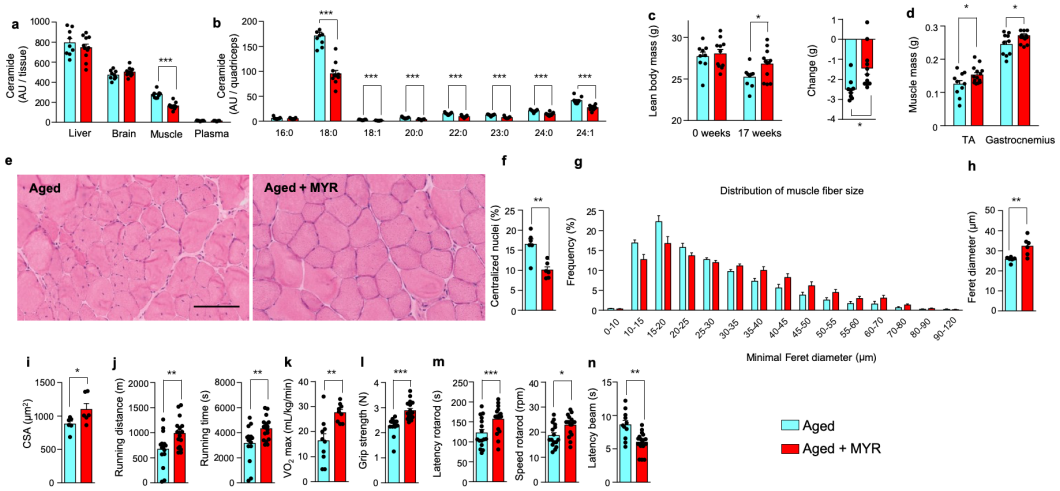

Figure 3. 2. Inactivation of sphingolipid *de novo* synthesis increases muscle mass and improves muscle function. Aged (18-month-old) C57BL/6JRj mice were treated with intraperitoneal injections of myriocin (MYR) for 5 months @ 0.4 mg/kg/3 times per week. (**a**) Total ceramide levels in liver, brain, skeletal muscle, and plasma. (**b**) Concentrations of individual ceramide species in mouse quadriceps muscle. (**c**) Lean body mass measured before and after treatment, and its change. (**d**) Gastrocnemius and tibialis anterior (TA) mass. For **a-d**, Aged mice: n=9, Aged mice + MYR: n=11. (**e**) Hematoxylin and eosin (H&E) staining of TA muscle. Scale bar, 50 µm. (**f**) Proportion of fibers with centralized nuclei. Distribution (**g**), mean of fiber minimal Feret diameter (**h**), and cross-sectional area (CSA) (**i**) in TA muscle. For **f-i**, Aged mice: n=6, Aged mice + MYR: n=11. Comparison of maximal running distance and duration (n=15/17) (**j**), aerobic capacity (n=10/9) (**k**), grip strength (n=15/17) (**l**), latency and maximal speed of rotarod test (n=16/17) (**m**), and latency of beam crossing (n=11/15) (**n**) between aged DMSO and myriocin treated mice. All data are shown mean ± SEM. **P* < 0.05, ***P* < 0.01, and ****P* < 0.001 with Student's two-tailed T test.

3.3.3 Sphingolipid reduction replenishes age-depleted MuSC pool

To identify biological pathways whose modulation could explain improved muscle function upon myriocin treatment, we compared transcriptomes of quadriceps muscle of aged myriocin and DMSO treated mice using RNA sequencing. We performed gene set enrichment analysis (GSEA) ranking transcripts based on their fold change. The most downregulated pathways by myriocin treatment were related to the extensively studied role of sphingolipids in lipid metabolism and inflammation, while upregulated pathways were related to muscle contraction and differentiation (Figure 3. 3a-b and Figure 3. S2a-c), suggesting improved regeneration. Indeed, in a targeted analysis of canonical transcription factors governing myogenesis, *Myog* and *Myf5* were upregulated in skeletal muscle upon myriocin treatment (Figure 3. 3c).

Muscle stem cells (MuSCs) are capable of giving rise to mature muscle fibers, and their regenerative capacity has been reported to be impaired upon aging (*203*). The expression of *Pax7*, a specific marker of MuSCs, was upregulated in the quadriceps of myriocin treated mice (Figure 3. 3d). Consistent with this, *PAX7* expression in skeletal muscle correlated negatively

with the first PC of the ceramide synthetic pathway in both human (Figure 3. 3e) and mouse (Figure 3. 3f) populations. To study whether increased *Pax7* transcript abundance in skeletal muscle reflects elevated MuSC count, we isolated α7 integrin/CD34 double positive cells from the hind-limbs using fluorescence-activated cell sorting (FACS). Consistent with previous reports (*105, 185*) the number of MuSCs was decreased in hindlimbs of aged as compared to young mice, and myriocin treatment restored the MuSC pool of aged mice close to that of young mice (Figure 3. 3g-i). Tissue sections of TA from myriocin treated mice revealed elevated number of PAX7^{+} muscle cells (Figure 3. 3j-k, Figure 3. S2d), suggesting increased MuSC proliferation, and MuSCs isolated from untreated aged mice and cultured *ex vivo* in myriocin containing medium resulted in higher Ki67^{+} MuSC count (Figure 3. 3l-m), indicating that myriocin treatment enhances MuSC proliferation. Upon aging, there is a decline in self-renewal and proliferative potential of MuSCs (*204*), and our findings suggest that sphingolipid depletion could counteract these defects.

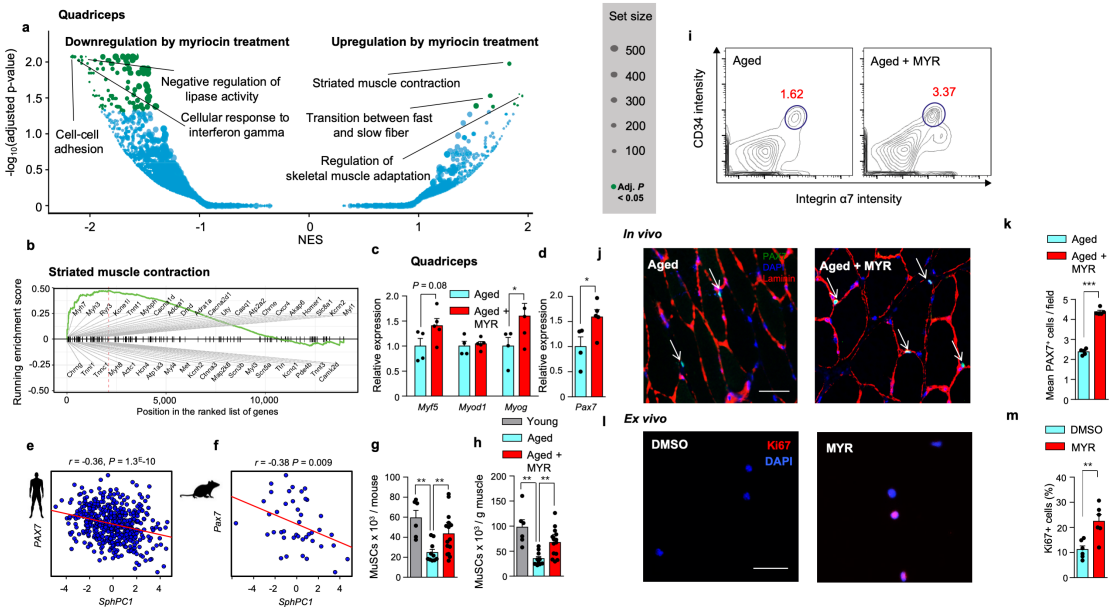

Figure 3. 3. Inhibition of sphingolipid *de novo* synthesis increases MuSC proliferation and tissue count. RNA-seq analysis from quadriceps muscle of aged mice treated with DMSO or myriocin. Volcano plot (**a**) of the genesets (GO categories) with nomalized enrichment score (NES) and adjusted p-value for each geneset given. Enrichment plot of the 'Striated muscle contraction' (**b**), the most upregulated GO category by myriocin. Comparison of transcripts of *Myf5*, *Myod1*, and *Myog* (**c**), and the MuSC marker *Pax7* (**d**) in aged and aged mice treated with myriocin as described in Figure 2. For **a-d**, Aged mice: n=4, Aged mice + MYR: n=5. (**e**) Correlation of *SphPC1*, i.e. the first principal component of the sphingolipid *de novo* synthesis pathway, with *PAX7* in human skeletal muscle (GTEx, n=491). (**f**) Correlation of *SphPC1* with *Pax7* in mouse skeletal muscle (BXD, n=42). Number of freshly isolated MuSCs from total hindlimbs musculature (**g**), normalized to muscle weight (**h**) from young, aged, and aged mice treated with myriocin. For **g-h**, Young mice: n=6, Aged mice: n=10, Aged mice + MYR: n=15. (**i**) FACS contour plot of α7 integrin^{+}CD34^{+}Sca-1^{-}CD45^{-}CD31^{-}CD11b^{-} cells which correspond to MuSCs isolated from aged and aged mice treated with myriocin. Representative images (**j**) and quantification (**k**) of PAX7-immunostained cells in TA muscle. DAPI, 4'6-diamino-2-phenylindole. Scale bar, 50 µm. Immunocytochemistry (**l**) and quantification (**m**) of Ki67 positive cells from freshly isolated MuSCs from aged C57BL/6JRj mice after 72 h incubation in DMSO or myriocin containing medium. For **k**&**m**, n=6/6. Scale bar, 50 µm. All data are shown mean ± SEM. **P* < 0.05, ***P* < 0.01, and ****P* < 0.001 with Student's two-tailed T test.

3.3.4 Myriocin primes MuSCs for accelerated regeneration

Decline in tissue regenerative potential is a major hallmark of mammalian aging (*205*), including skeletal muscle (*206*). We next asked the question whether myriocin treatment induces functional improvement of MuSCs, boosting their regenerative capacity. We isolated MuSCs from aged mice treated or untreated with myriocin for 5 months, and transplanted them into tibialis anterior (TA) muscles of recipient mice. The recipient mice were either aged (20-month-old) C57Bl/6JRj or aged (1-year-old) *mdx* mice, a mouse model of Duchenne

muscular dystrophy, lacking the dystrophin protein (Figure 3. 4a). Before MuSC transplantation, we induced injury by cardiotoxin injection into the TA of all recipient mice. After 7 days of transplantation, *mdx* mice displayed elevated count of PAX7⁺ cells, indicating more efficient MuSC proliferation (Figure 3. 4b-c and Figure 3. S3c). MuSCs isolated from myriocin treated mice stimulated myogenesis of dystrophin-positive fibers, verifying the functionality of newly transplanted MuSCs (Figure 3. 4d-e). At both 7 and 14 days after transplantation the inflammatory area was also smaller (Figure 3. S3a-b) in *mdx* recipients of MuSCs isolated from myriocin treated mice. Aged C57Bl/6JRj recipients of MuSCs isolated from myriocin treated mice exhibited similar morphologic changes in muscle to *mdx* recipients, manifested by increased count of PAX7⁺ cells per field (Figure 3. 4f-g) and per section (Figure 3. S3c), higher embryonic myosin heavy chain (eMyHC) positive area (Figure 3. 4h-i), indicating increased muscle regeneration, and smaller inflammatory area at both 7 and 14 days after injury (Figure 3. 4j-m). Thus, transplantation of MuSCs derived from myriocin treated donors induce major morphological improvements following cardiotoxin-induced muscle injury.

To test whether the functional improvement of MuSCs upon myriocin treatment also translates into better muscle function of recipient mice, we performed tests of muscle function before and 7 days after MuSC transplantation. After 7 days of MuSC transplantation, aged C57Bl/6JRj mice, which had received MuSCs from myriocin treated mice, displayed improved exercise capacity (Figure 3. 4n), grip strength (Figure 3. 4o), and increased latency in rotarod test (Figure 3. 4p). These findings demonstrate that myriocin-induced improvement in MuSC function also translates into better muscle physiological function.

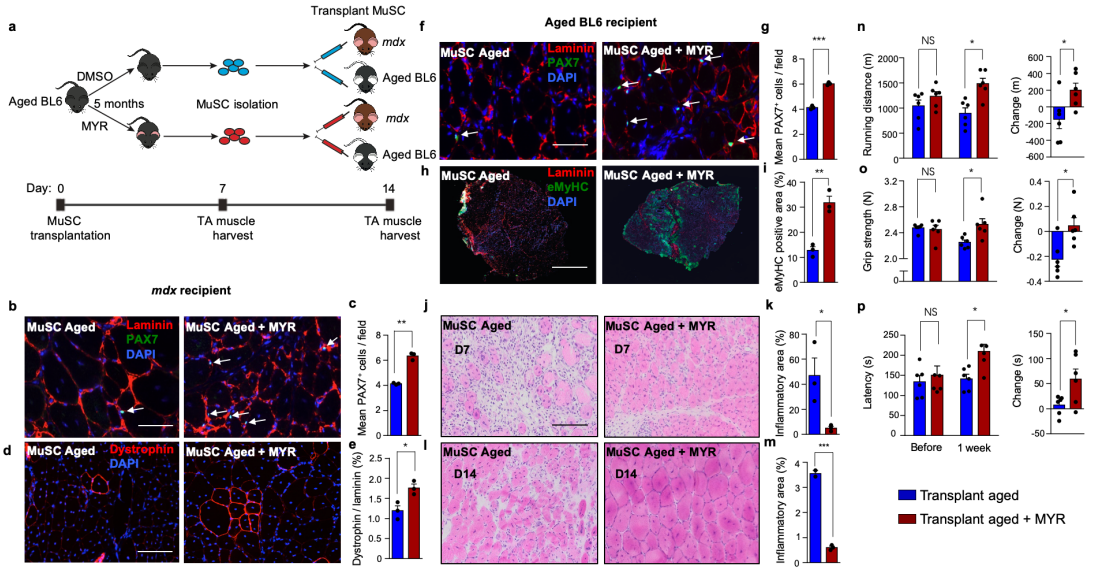

Figure 3. 4. Sphingolipid depletion improves MuSC function and regenerative capacity *in vivo*. (**a**) Aged C57BL/6JRj mice were treated with myriocin, and upon sacrifice, freshly isolated MuSCs were transplanted into the TA of either cardiotoxin damaged aged C57BL/6JRj or *mdx* recipient mice. Representative images and quantification of PAX7 (**b-c**) and dystrophin (**d-e**) immunostained TA muscle from *mdx* recipients 7 days after transplantation. Scale bar, 50 µm. Representative images and quantification of PAX7 (**f-g**) and embryonic myosin heavy chain (eMyHC) (**h-i**) in immunostained TA muscle from aged C57BL/6JRj mice at 7 days after transplantation. Scale bar, 50 µm in PAX7 staining. Scale bar, 250 µm in eMyHC staining. Representative images and quantification of H&E stained TA from aged C57BL/6JRj recipients at 7 days (**j-k**) and 14 days (**l-m**) after transplantation. Scale bar, 50 µm. For **c-m**, Recipients of Aged MuSC: n=3. Recipients of Aged + MYR MuSC: n=3. Maximal running distance (**n**), grip strength (**o**), and latency on a rotarod (**p**) before and 7 days after transplantation. The change relative to baseline is reported. For **n-p**, Recipients of Aged MuSC: n=6. Recipients of Aged + MYR MuSC: n=6. All data are shown mean ± SEM. **P* < 0.05, ***P* < 0.01, and ****P* < 0.001 with Student's two-tailed T test.

3.3.5 Sphingolipid depletion activates myogenic differentiation in muscle progenitor cells

Inhibition of sphingolipid *de novo* synthesis pathway has previously been linked to metabolic benefits, including improved insulin sensitivity (*191, 195*) which might affect muscle function. To study whether sphingolipid depletion has a cell-autonomous effect on myogenesis and muscle regeneration, we incubated freshly isolated MuSCs in 30 µM myriocin containing culture medium. Myriocin elevated both MYOD and MYOG protein levels (Figure 3. 5a-b), indicating that sphingolipid depletion primes MuSCs for myogenic differentiation. We then examined the effects of myriocin in myoblasts, a later stage myogenic progenitor cell using mouse C2C12 myoblasts. Myriocin accelerated myoblast differentiation (Figure 3. 5c), as shown by greater fusion index (Figure 3. 5d) and myotube area (Figure 3. 5e), and induced a myogenic transcript signature featuring upregulation of myogenic transcription factors, such as *Myog*, as well markers of mature myotubes, including myosin heavy chain subunits *Myh4* and *Myh1* (Figure 3. 5f).

To corroborate the effects of the sphingolipid *de novo* synthesis pathway on myogenesis, we silenced members of the pathway using polyclonal CRISPR-Cas9 genome editing. Knockout of *Sptlc1* induced myoblast differentiation (Figure 3. 5g), as determined by quantification of fusion index (Figure 3. 5h), myotube area (Figure 3. 5i), and a myogenic transcript signature similar to myriocin treated cells (Figure 3. 5j). We also silenced *Cers2*, the most abundant ceramide synthase in skeletal muscle, downstream of SPT. Inactivation of *Cers2* led to accelerated myogenesis (Figure 3. 5k-m), featuring similar gene expression signature to that observed after myriocin treatment (Figure 3. 5n). Thus, enzymes downstream of SPT are involved in myogenic programming in a cell-autonomous manner.

To further validate our findings, we generated homozygous (*Sptlc1*$^{-/-}$) and heterozygous (*Sptlc1*$^{+/-}$) single clone knockouts of *Sptlc1* using CRISPR-Cas9 in C2C12 myoblasts (Figure 3. S4a-c). The single clone knockouts promoted myogenesis in an allele dose-dependent manner, with *Sptlc1*$^{-/-}$ myoblasts displaying greater myotube area than *Sptlc1*$^{+/-}$ or EV cells (Figure 3. S4d-g). While the polyclonal *Sptlc1* and *Cers2* knockouts had milder effects on gene expression signature than myriocin (Figure 3. 5j,n), the *Sptlc1*$^{-/-}$ single clone knockouts induced changes in a similar range to myriocin treatment (Figure 3. 5f and Figure 3. S4f). Thus, SPT abundance dose-dependently influences muscle differentiation.

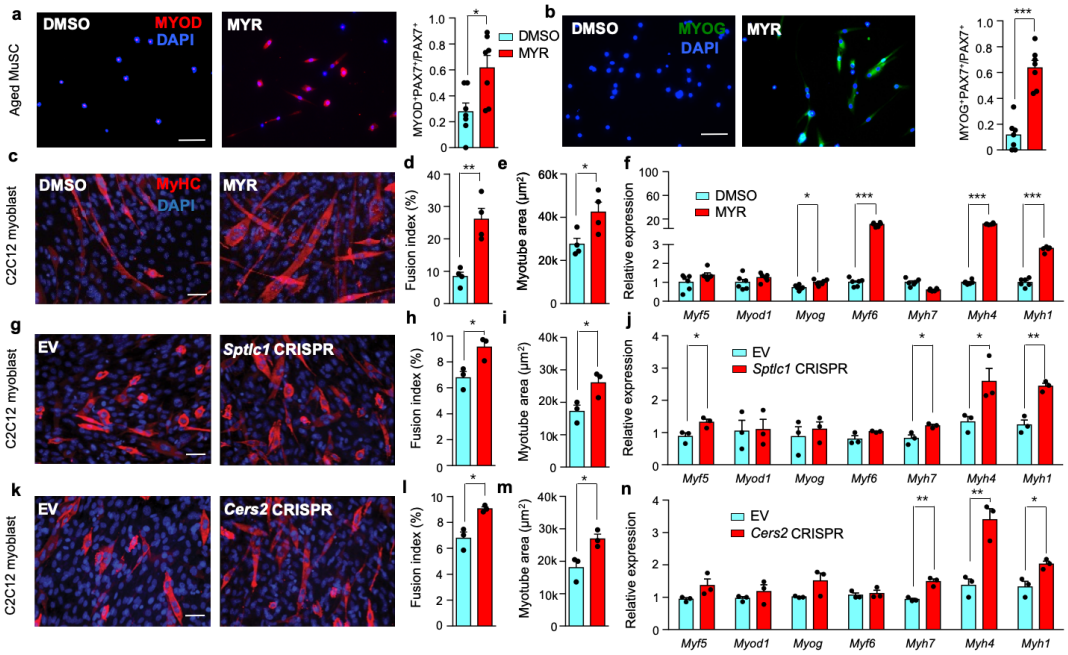

Figure 3. 5. Sphingolipid depletion cell-autonomously activates muscle differentiation in MuSCs and myoblasts. (**a**) Immunocytochemistry and quantification of MYOD from freshly isolated MuSCs from aged C57BL/6JRj mice after 72 h incubation in DMSO or myriocin containing medium. (**b**) Immunocytochemistry and

quantification of MYOG from freshly isolated MuSCs from aged C57BL/6JRj mice. For **a-b**, n=7+7. Immunocytochemistry (**c**), fusion index (**d**), myotube area (**e**), and expression of myogenesis markers (**f**) from C2C12 myoblasts grown in DMSO and myriocin containing medium. Immunocytochemistry (**g**), fusion index (**h**), myotube area (**i**), and gene expression of myogenesis markers (**j**) from C2C12 myoblasts silenced for *Sptlc1* using CRISPR-Cas9. For **d-e**, n=4+4. For **f**, n=6+6. Immunocytochemistry (**k**), fusion index (**l**), myotube area (**m**), and gene expression of myogenesis markers (**n**) from C2C12 myoblasts silenced for *Cers2* using CRISPR-Cas9. For **g-n**, n=3+3. All data are shown mean ± SEM. **P* < 0.05, ***P* < 0.01, and ****P* < 0.001 with Student's two-tailed T test. Scale bar, 50 µm.

3.3.6 Genetic variants reducing SPT expression are associated with improved fitness in aged humans

To determine whether sphingolipid depletion could stimulate muscle differentiation in human cell lines, we treated human primary myoblasts with myriocin. Consistent with mouse myoblasts, myriocin accelerated human myoblast differentiation, displaying larger myotube area (Figure 3. 6a-c). Thus, SPT inhibition could enhance muscle maintenance in human muscles.

We finally investigated whether the sphingolipid *de novo* synthesis pathway is involved in age-related muscle dysfunction in humans by gathering evidence from human genetic studies. The mammalian SPT enzyme is a heterodimer, encoded by two subunits, *SPTLC1* and *SPTLC2* (*207*). The objective was to first examine the region near *SPTLC1* and *SPTLC2* to identify loci that associate with the expression of these genes in skeletal muscle (*cis*-expression quantitative trait loci (*cis*-eQTL)), and then test whether these *cis*-eQTLs are associated with muscular fitness of aged individuals. The regions near the *SPTLC1* and *SPTLC2* were both spanned by 4 haploblocks ($r^2 > 0.2$) (Figure 3. 6d). Using skeletal muscle gene expression data from the GTEx project, we identified *cis*-eQTLs for *SPTLC1* and *SPTLC2* (Table 3. S1-2) in tight linkage disequilibrium within the gene (Figure 3. S5a-b). The *cis*-eQTL with the largest effect on *SPTLC1* expression, rs10820917, was located within a haploblock spanning 250 kb region between *SPTLC1* and its neighboring *ROR2* (Haploblock 1) while the most significant *cis*-eQTL for *SPTLC2* was located 680 kb upstream of the gene (Figure 3. 6d). The major alleles (C) of rs10820917 and rs8013312 were associated with reduced transcript abundance of *SPTLC1* and *SPTLC2*, respectively, in a dose-dependent manner (Figure 3. 6e-f). They were exclusively associated with SPT transcript levels, and not with transcript levels of any of the neighboring genes (Table 3. S 3-4). As the SPT heterodimer consists of both *SPTLC1* and *SPTLC2* encoded subunits, we constructed a two-locus genetic score indicating the total number of C alleles within *SPTLC1* rs10820917 and *SPTLC2* rs8013312 loci. The average gene expression of *SPTLC1* and *SPTLC2* was dose-dependently associated with the C allele score, individuals homozygous for C allele in both *SPTLC1* rs10820917 and *SPTLC2* rs8013312 loci displaying the lowest *SPTLC1-SPTLC2* expression (Figure 3. 6e-f).

To test the effects of the identified *cis*-eQTLs on muscular fitness upon aging, we examined individuals of the Helsinki Birth Cohort Study (HBCS; N=2,003), of whom approximately 800 between 70 to 80 years of age underwent an extensive battery of physical fitness measurements (Table 3. 1) (*208*). The objectively measured fitness tests includes arm curl, number of chair stands, chair sit and reach, back scratch, and 6-min walk test, and collectively constitutes the senior fitness test (SFT) score. We first tested the association of the *SPTLC1-SPTLC2* two-locus genetic score with SFT score in non-diabetic individuals, and observed that increased C allele count was dose-dependently associated with improved SFT score ($P = 0.01$) (Figure 3. 6e-f). Of the SFT component traits, 6-min walking distance and chair sit and reach were associated with the *SPTLC* C allele count ($P = 0.03$ and $P = 0.04$), as well as improved grip strength, a trait not included in SFT test battery ($P = 0.006$) (Figure 3. 6e). We then analyzed the most significant *cis*-eQTL of *SPTLC1* and *SPTLC2* individually. The reduced expression associated C alleles of rs10820917 and rs8013312 in *SPTLC1* and *SPTLC2*, were associated with higher SFT ($P = 0.04$ and $P = 0.004$) (Figure 3. 6e-f). Of the component traits, the major C allele of *SPTLC1* rs10820917 was associated with improved

performance in 6-min walking test (*P* = 0.03), arm curl (*P* = 0.01), as well as grip strength (*P* = 0.004) while the major C allele of *SPTLC2* rs8013312 was associated with increased 6-min walking distance (*P* = 0.003), improved flexibility in sit and reach (*P* = 0.02), and back scratch (*P* = 0.01) tests (Figure 3. 6e-f). These genetic data, demonstrating that SPT transcript reducing genetic variants improve age-related fitness, are consistent with outcomes from our pharmacological approach in the aged mice, implying that SPT inhibition in human aging could deliver considerable fitness benefits.

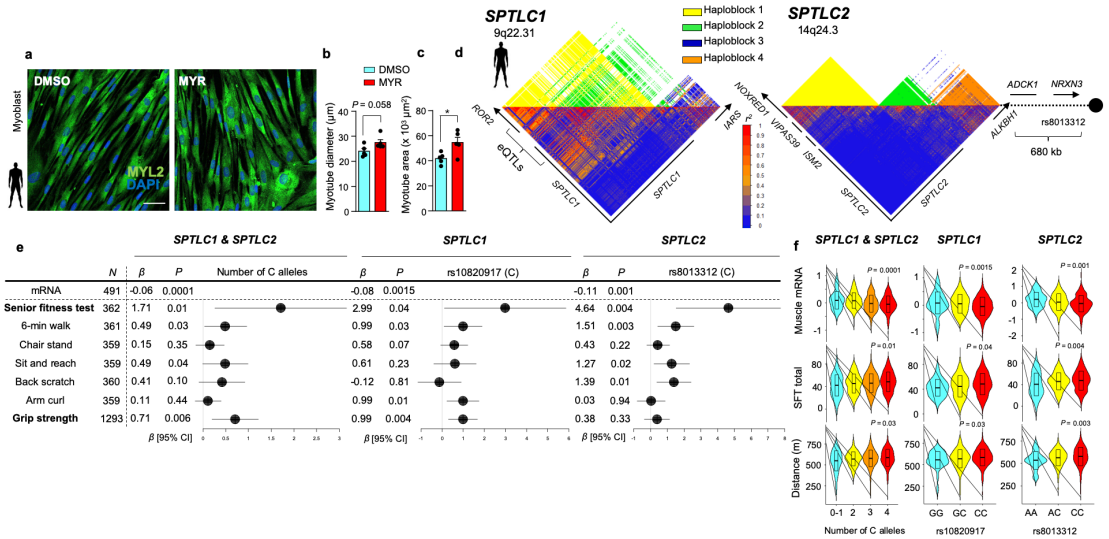

Figure 3. 6. Genetic evidence points to beneficial effects of sphingolipid depletion in humans. Immunocytochemistry (**a**), myotube diameter (**b**), and myotube area (**c**) of human primary myoblasts treated with DMSO or myriocin. For **a-c**, n=5+5. All data are shown mean ± SEM. **P* < 0.05 with Student's two-tailed T test. Scale bar, 50 µm. Haploblock structure of human *SPTLC1* and *SPTLC2* (**d**) loci. (**e**) Associations of *SPTLC1* and *SPTLC2 cis*-eQTLs rs10820917 and rs8013312 with mRNA levels of *SPTLC1* and *SPTL2* in GTEx, respectively, and senior fitness test (SFT) score, and its component traits in Helsinki Birth Cohort Study. The forest plot represents *β* with 95% confidence interval (CI). (**f**) Violin plots of skeletal muscle mRNA, SFT score, and distance in a 6-min walking test as a function of *SPTLC1* and *SPTLC2 cis*-eQTLs rs10820917 and rs8013312, respectively.

3.4 DISCUSSION

In this study we establish the relationship between sphingolipid metabolism and age-related sarcopenia. Sphingolipids have been associated with metabolic disease, cancer, and cardiovascular disease (*108*). Diabetes is reported to be a risk factor for sarcopenia (*209*), and although sphingolipids could partly contribute to the onset of sarcopenia through exacerbation of metabolic disease, our study provides evidence that sphingolipids have an independent effect on muscle regeneration. This is validated by myriocin-induced proliferation and differentiation of freshly isolated MuSCs as well as mouse and human immortalized myoblast cell lines, demonstrating the cell-autonomous effect of sphingolipid synthesis inhibition on myogenesis. The specificity of these effects to sphingolipid *de novo* synthesis pathway, and not to off-target effects of myriocin, is verified by myogenesis-promoting effects of genetic inactivation of two key enzymes of the pathway, *Sptlc1* and *Cers2*, the most abundant ceramide synthase in skeletal muscle. These findings indicate that inhibition of sphingolipid *de novo* synthesis pathway could attenuate sarcopenia through promoting muscle growth.

In mice, blocking sphingolipid *de novo* synthesis results in multiple benefits counteracting the effects of aging on MuSCs. Myriocin treatment increased the proliferative capacity of MuSCs, replenishing the age-depleted MuSC pool, and it appears to prime MuSCs to accelerated regeneration, as manifested by increased MYOD and MYOG protein levels (Figure 3. 5a-b) upon myriocin treatment, and even improvements in physiological test performance upon MuSC transplantation from myriocin treated mice (Figure 3. 4n-p). The increased myogenic potential is not limited to MuSCs, but extends to myoblasts as well, suggesting a broader myogenic effect of sphingolipid depletion on muscle progenitor cells. These findings strongly

suggest that increased regenerative capacity of progenitor cells could underlie the beneficial fitness effects of sphingolipid depletion.

Genetic analyses of participants from the Helsinki Birth Cohort Study suggest that targeting sphingolipid *de novo* biosynthesis pathway could also have fitness-related benefits in humans. Individuals carrying the major alleles of *SPTLC1* and *SPTLC2* polymorphisms displayed both reduced mRNA expression in GTEx data, and improved age-related fitness in the HBCS, represented by the SFT score. It appears that the *SPTLC1* variant shows stronger associations with muscle strength, such as grip strength and arm curl, while the *SPTLC2* variant shows stronger associations with flexibility, such as back scratch, and sit and reach. This aspect would require further study, even though the general direction of effect sizes was very uniform. In summary, the overlap between the *cis*-eQTL and QTL signals hint that genetically decreased levels of *SPTLC1* and *SPTLC2* levels could lead to improved fitness which, consistent with the *in vivo* treatment of myriocin, suggest that pharmacological approaches to inactivate sphingolipid *de novo* synthesis in humans could deliver desirable outcomes.

Our findings suggest that inhibition of SPT and sphingolipid synthesis could be a therapeutic strategy to treat age-related sarcopenia. As sarcopenia is associated with chronic comorbities, sarcopenic patients are often managed with a number of medications (*210*). Although multiple drug usage may be necessary to obtain satisfactory treatment outcomes for chronic disease, it simultaneously predisposes patients to adverse drug reaction, interactions, and prescription cascade (*210*). One way to reduce age-associated polypharmacy, while providing effective treatment to chronic diseases, could be the development of multitargeted therapeutics, i.e. single pharmaceutical agents targeting multiple diseases (*211*). Given the involvement of sphingolipids in a number of diseases (*108*), targeting sphingolipid metabolism could produce benefits far beyond sarcopenia, having the potential to moderate multiple drug prescriptions. Our study presents a strong case to embark on the development of potent inhibitors of sphingolipid synthesis for age-related sarcopenia and co-occurring pathologies.

3.5 MATERIALS AND METHODS

***In vivo* studies**

Animals. Young (2-month-old) and aged (18-month-old) male C57Bl/6JRj mice were purchased from Janvier Labs. EchoMRI measuring the fat and lean body mass, were measured before and after the treatment. The dose of myriocin was 0.4 mg/kg/3 times a week. Myriocin (Enzo Life Sciences, Farmingdale, NY) was first dissolved in DMSO which was then mixed with PBS so that each mouse received 1.5 µL DMSO per injection. Animals were fed on a standard chow diet. All animals were housed in micro-isolator cages in a room illuminated from 7:00AM to 7:00PM with ad libitum access to diet and water. All the animal experiments are authorized by animal license 2890.1 and 3341 in Canton of Vaud, Switzerland.

Measurement of sphingolipids. Plasma (100 µL) and weighed tissue samples (20-60 mg) were transferred to 2 ml Safe-Lock PP-tubes, and extracted as previously described (*212*). In brief, samples were homogenized using two 6 mm steal beads on a Mixer Mill (Retsch, Haan, GER; 2x10sec, frequency 30/s) in 700 µL MTBE/MeOH (3/1, v/v) containing 500 pmol butylated hydroxytoluene, 1% acetic acid, and 200 pmol of internal standards (IS, d18:1/17:0 ceramide, d18:1/17:0 sphingomyelin, Avanti Polar Lipids, Alabaster, AL, USA) per sample. Total lipid extraction was performed under constant shaking for 30 min at RT. After addition of 140 µL dH2O and further incubation for 30 min on RT, samples were centrifuged at 1,000 x g for 15 min to establish phase separation. 500 µL of the upper, organic phase were collected and dried under a stream of nitrogen. Lipids were resolved in 700 µL 2-propanol/methanol/water (7/2.5/1, v/v/v) for UPLC-MS analysis. Remaining tissues were dried, solubilized in NaOH (0.3 N) at 65 °C for 4 h and the protein content was determined using Pierce™ BCA reagent (Thermo Fisher Scientific, Waltham, MA, USA) and BSA as standard.

Chromatographic separation was modified after Knittelfelder et al. (*213*) using an ACQUITY-UPLC system (Waters Corporation), equipped with a Luna omega C18 column (2.1x50 mm, 1.6 µm; Phenomenex) starting a 20 min linear gradient with 80% solvent A (MeOH/H2O, 1/1, v/v; 10 mM ammonium acetate, 0,1% formic acid, 8 µM phosphoric acid). The column compartment was kept on 50°C. A EVOQ Elite™ triple quadrupole mass spectrometer (Bruker) equipped with an ESI source was used for detection of lipids in positive ionization mode. Lipid species were analyzed by selected reaction monitoring (ceramide, [M+H]+ to m/z 264.3, 22 eV, 60 ms; sphingomyelin, [M+H]+ to m/z 184.1, 20eV, 40 ms; resolution 0.7 Q1/Q3). Data acquisition was done by MS Workstation (Bruker). Data were normalized for recovery, extraction-, and ionization efficacy by calculating analyte/IS ratios (AU) and expressed as AU/g tissue or AU/mL plasma.

Measurement of deoxysphingolipids. Plasma and muscle sphingolipids were processed using a method adapted from (*214*). Briefly, 10-15 mg of muscle sample was extracted with 500 µL of -20 °C methanol, 400 µL of ice-cold saline, 100 µL of ice-cold water and spiked with internal standard deoxysphinganine d3 (Avanti lipids). An aliquot (50 µL) of homogenate was dried under air and resuspended in RIPA buffer for protein quantification using BCA assay (BCA Protein Assay, Lambda, Biotech Inc., US). To the remaining homogenate, 1 mL of chloroform was added and the samples were vortexed for 5 min followed by centrifugation at 4°C for 5 min at 15 000 x G. The organic phase was collected and 2 µL of formic acid was added to the remaining polar phase, which was re-extracted with 1 mL of chloroform. Combined organic phases were dried and the pellet was resuspended in 500 µL of methanol and subsequent extraction steps were identical as described for plasma.

Fifty microliters of plasma was mixed with 500 µL of methanol and spiked with internal standard of deoxysphinganine d3 (Avanti lipids). The samples were placed on a mixer for 1 h at 37°C, centrifuged at 2800 x G and the supernatant collected and acid hydrolyzed overnight at 65°C with 75 µL of methanolic HCl (1N HCl,10M H2O in methanol). Next, 100 µL of 10 M

KOH was added to neutralize. 625 µL of chloroform, 100 µL of 2N NH4OH and 500 µL of alkaline water were added, the sample vortex-mixed and centrifuged for 5 min at 16 000 g. The lower organic phase was washed three times with alkaline water and dried under air. LCMS analysis was performed on an Agilent 6460 QQQ LC-MS/MS. Metabolite separation was achieved with a C18 column (Luna 100 x 2.1 mm, 3µm, Phenomenex). Mobile phase A was composed of a 60:40 ratio of methanol:water and mobile phase B consisted of 100% methanol with 0.1% formic acid with 5 mM ammonium formate added to both mobile phases. The gradient elution program consisted of holding at 40% B for 0.5 min, linearly increasing to 100% B over 15 min, and maintaining it for 9 min, followed by re-equilibration to the initial condition for 10 min. The capillary voltage was set to 3.5 kV, the drying gas temperature was 350 °C, the drying gas flow rate was 10 L/min, and the nebulizer pressure was 60 psi. Sphingoid bases were analyzed by SRM of the transition from precursor to product ions at associated optimized collision energies and fragmentor voltages (Table below). Sphingoid bases were then quantified from spiked internal standards of known concentration.

Sphingoid base	Parent ion	Daughter ion	N
m17:0 doxSA	272.4	254.4	13
m18:0 doxSA	286.3	268.4	13
m18:0 doxSA d3	289.3	271.5	13

Endurance running test. The exercise regimen on a treadmill commenced at a speed of 15 cm/s. After every 12 minutes, the speed was increased by 3 cm/s. As the mice were aged, we used an inclination of 0 degrees. Mice were considered to be exhausted, and removed from the treadmill if they received 7 or more shocks (0.2 mA) per minute for two consecutive minutes. The distance traveled and time before exhaustion were registered as maximal running distance and time (*105, 215*).

Grip strength. Muscle strength was assessed by grip strength test. The grip strength of each mouse was measured on a pulldown grid assembly connected to a grip strength meter (Columbus Instruments). The mouse was drawn along a straight line parallel to the grip, providing peak force. The experiment was repeated three times, and the highest value was included in the analysis.

Rotarod test. The rotarod test measures muscle strength, coordination, and endurance (*216*). Mice were left undisturbed in the room for 30 min. The speed of the rotating cylinder (rotarod) increased from 0 to 40 rpm in 5 min. Each mouse had 3 trials per day for 3 consecutive days. The latency and speed the mouse reached it passive rotation or fall from the rotor was recorded, and the latency and speed of the best trial of the second day is presented.

Crossbar test. Crossbar test assesses active balance through the ability to balance while walking along an elevated beam to reach a dark end side where they are able hide (*217*). Since all the mice were easily able to cross a squared (3 cm) beam, and a circular beam of diameter 1.5 cm was too difficult to them, we recorded the latency to cross a circular beam of 3 cm. The mice were trained for one day before the actual trial was recorded, and the average of the latency of three trials per mouse is presented.

Stem cell isolation. Gastrocnemius, soleus, and quadriceps muscles from both hindlimbs were excised and transferred into PBS on ice. All muscles were trimmed, minced and digested with 2.5U/ml of Dispase II (Roche) and 0.2% Collagenase B (Roche) in PBS for 30 mins at 37 °C. Samples were then centrifuged at 50*g* for 5 min followed by removing the supernatant and further digested for 20 mins at 37 °C twice. Muscle slurries were sequentially filtered through 100 µm and 40 µm cell strainers. The isolated cells were then washed in washing buffer (PBS + 2.5% BSA) and resuspended in 800 µL of washing buffer. They were immediately stained with antibodies, including CD31 (1:800, eBioscience, eFluor450

conjugated); CD45 (1:200, eBioscience, eFluor450 conjugated); Sca-1 (1:1000, eBioscience, PE-Cy7 conjugated); CD11b (1:100, eBioscience, eFluor450) and CD34 (1:100, BD Pharmingen, FITC conjugated); alpha-7 integrin (1:50, RD system, eFluor700 conjugated) for 45 min at 4°C. Secondary staining was performed with propidium iodide (PI, Sigma) for 15 min at 4°C in the dark. Stained cells were analyzed and sorted using the FACSAria II instrument (BD Biosciences). Debris and dead cells were excluded by forward scatter, side scatter and PI gating.

Cardiotoxin-induced muscle damage and MuSC transplantation. MuSCs were transplanted from donor mice to recipient mice. The donor mice were aged male C57Bl/6JRj mice, whose treatment with myriocin was started at the age of 18 months. The recipient mice were either aged (18-month-old) male C57Bl/6JRj mice or 1-year-old male *mdx* mice. 50 µL of 20 µM *Naje mossambica mossambica* cardiotoxin (Sigma) was injected intramuscularly into the tibialis anterior (TA) muscle of recipient mice before transplantation. 24 h after CTX injection, equal number (1500) of freshly isolated MuSCs from donor mice were injected intramuscularly into the TA muscle. Recipient mice were sacrificed at 7 and 14 days after transplantation.

Histology. TA muscles were harvested from anesthetized mice, and immediately embedded in Thermo Scientific™ Shandon™ Cryomatrix™ and frozen in isopentane, cooled in liquid nitrogen, for 1 min before being transferred to dry ice and stored at -80 °C. 8 µm cryosections were incubated in 4% PFA for 15 min, washed three times for 10 min with PBS, incubated for antigen retrieval in pH 6.0 citrate buffer for 10 min at 95 ºC (for PAX7 antibody), counterstained with DAPI, laminin (1:200, Sigma), PAX7 (1:200, DSHB, University of Iowa), dystrophin (1:100, Spring Bioscience) or eMyHC (1:50, DSHB, University of Iowa), coupled with Alexa-488 or Alexa-568 fluorochromes (Life Technology) and mounted with Dako Mounting Medium. Microscopy images of fluorescence from muscle fibers were analyzed using the ImageJ software. Centralized nuclei percent, minimal Feret diameter and cross-sectional area in TA muscles were determined using the ImageJ software quantification of laminin, dystrophin, and DAPI-stained muscle images from VS120-S6-W slides scanner (Olympus). A minimum of 2,000 fibers were used for each condition and measurement. The minimal Feret diameter is defined as the minimum distance between two parallel tangents at opposing borders of the muscle fiber. This measure has been found to be resistant to deviations away from the optimal cross-sectioning profile during the sectioning process. The mean cross-sectional area of muscle fibers was calculated as the average cross-sectional area of 2,000 fibers per from sample. 7-8 mouse samples per condition were used for histological quantification of donor mice. The eMyHC quantification is expressed as proportion of eMyHC positive signal over total TA cross sectional area. Following MuSC injection in CTX injected recipient mice, inflammation representing the regenerative stage of muscle was quantified by ImageJ software as proportion of inflammatory area over total area of the TA muscle cross section. The PAX7-positive cells were quantified as the average number of cells per field of more than 30 randomly chosen fields from a mouse TA. For each quantification, 3 or more mice were used.

***Ex vivo* analysis of MuSCs.** MuSCs were isolated as described above, and seeded in 96- or 48-well plates. The cells were incubated in 30 µM myriocin containing medium (Ham's F-10 nutrient mixture, FBS 20%, basic fibroblast growth factor 2.5 ng/mL, penicillin 100 U/mL, streptomycin 100 µg/mL) for 72 hours. PFA 4% was applied for 15 min, the cells were washed three times for 10 min with PBS, and were blocked in 2% BSA in PBS. The cells were then incubated in primary antibodies MYOD (1:50, LabForce) and MYOG (1:50, Santa Cruz) overnight at 4 ºC. Secondary antibodies were coupled with Alexa-488 or Alexa-568 fluorochromes (Life Technology) and mounted with Dako Mounting Medium. Leica DMI 4000 microscope was used to image the cells. Quantification of the $MYOD^+$ and $MYOG^+$ cell number was based on more than 500 cells per condition.

***In vitro* studies**

Cell culture and cell transfection. The C2C12 mouse myoblast cell line was obtained from the American Type Culture Collection (CRL-1772TM). C2C12 cells or clones were cultured in growth medium consisting of Dulbecco's modified Eagle's medium (Gibco, 41966-029), 20 % Fetal Bovine Serum (Gibco, 10270-106) and 100 U/mL penicillin and 100 mg/mL streptomycin (Gibco, 15140- 122). To induce differentiation, FBS was substituted with 2% horse serum (Gibco, 16050-122). Trypsin-EDTA 0.05% (GIBCO, 25300- 062) was used to detach cells. Human skeletal muscle cells were obtained from Lonza (SkMC, #CC-2561) and cultured in growth medium consisting of DMEM/F12 (Gibco, 10565018), 20 % Fetal Bovine Serum (Gibco, 10270-106) and 100 U/mL penicillin and 100 mg/mL streptomycin (Gibco, 15140- 122). To induce differentiation, FBS was reduced to 2 % and kept in culture. All cells were maintained at 37 °C with 5% CO_2. Cell transfections were done using TransIT (Mirus) according to the manufacturer's protocol with a 3:1 ratio of transfection agent to DNA. C2C12 cells were grown confluent, and 30 µM myriocin or DMSO was added and cells were kept in growth medium for another 3 days. *Sptlc1* clones were plated to reach confluency simultaneously and were kept in growth medium for 3 days before using them for immunocytochemistry or RNA isolation. The concentration of myriocin in medium for all experiments was 30 µM. A stock solution of 20 mM myriocin in DMSO was used dissolve myriocin, and a corresponding volume of DMSO without myriocin was used as control. Cell lines were tested for mycoplasma contamination. No contamination observed.

CRISPR guide RNA design and cloning. Two guide RNAs per gene were designed with the help of the online GPP web portal tool (https://portals.broadinstitute.org/gpp/public/analysis-tools/sgrna-design) using *Streptococcus pyogenes* PAM sequence (NGG). The guide RNAs with best predicted on- and off-target scores were selected. The guide RNA sequences are listed in Table 3. S6. The oligonucleotides were synthesized (Microsynth, Switzerland) and cloned into the CRISPRv2 plasmid (addgene #52961) using the BsmBI restriction sides (*218*). The insertion by cloning was verified by Sanger sequencing (Microsynth, Switzerland). To test the efficiency of the guide RNAs, the cloned vectors were transiently transfected (TransIT, Mirus) in C2C12 cells, and 48h after transfection RNA was isolated, reverse transcribed and gene expression was measured by RT-qPCR.

Creation of single clone *Sptlc1* knockout in C2C12 myoblasts. C2C12 cells were transfected with the lentiCRISPR v2 plasmid containing the gRNAs targeting exon 1 of *Sptlc1* or the empty vector lentiCRISPR v2 plasmid as a control. 36 h after transfection cells were selected with 2 µg/mL puromycin (Invivo gene ; QLL3803A) for 3 days and single cell sorted. Five to ten different clones for each gRNA were grown without selection marker. DNA from these clones was isolated (Macherey-Nagel, 740952) and PCR amplified (see Table 3.S6). The PCR product was gel purified (Machery-Nagel, 740609) and Sanger sequencing was performed to verify the clones with deletions or insertions. In one of the clones, *Sptlc1* gRNA1 led to a homozygous knockout of *Sptlc1* (*Sptlc1*$^{-/-}$) whereas gRNA2 led to a heterozygous knockout of *Sptlc1* (*Sptlc*$^{+/-}$) in another clone.

Creation of polyclonal *Sptlc1* or *Cers2* knockouts in C2C12 myoblasts. Lentivirus particles were produced from lentiCRISPRv2 plasmids containing no gRNA (empty vector), *Sptlc1* gRNA2 or *Cers2* gRNA2 (Table 3. S7) by co-transfection with the packaging of plasmids pMD2G and psPAX2 in HEK 293T cells using Lipofectamine 2000. Viral supernatants were harvested 36 to 48 h post transfection. C2C12 were transduced with viral supernatant for 20 hours. 24 h later, cells were selected with 3 µg/mL puromycin for 3 days. Same EV control was used for both *Sptlc1* and *Cers2* knockouts. Reduction in the target protein was confirmed by Western blotting.

Western blotting. C2C12 cells were lysed on ice in RIPA buffer composed of Tris HCl 50 mM, NaCl 5 M, EDTA 5 mM, SFS 0.1%, NAF 100 mM, sodium deoxycholate 5 mg/mL, and NP40 1% containing protease and phosphatase inhibitors (Roche). Protein concentrations were determined using Bradford method, and samples were loaded on a 12% SDS-PAGE gel. After electrophoresis, proteins were separated by SDS-PAGE and transferred onto methanol activated polyvinylidene difluoride membranes. Blocking of the membranes was done in 5%

milk-TBST for 1 h, and after wash, the membranes were incubated overnight with primary antibody anti-SPTLC1 (Proteintech) 5% BSA-TBST 1:1000 or anti-CERS2 (Sigma) in 3% BSA-TBST 1:1000. Incubation with secondary anti-rabbit polyclonal antibody was done in 5% BSA-TBST 1:2000. Antibody detection reactions were developed by enhanced chemiluminescence (Advansta), and imaged using the c300 imaging system (Azure Biosystems).

RNA isolation and real time qPCR. RNA was isolated using the RNeasy Mini kit (Qiagen, 74106) and reverse transcribed with the High-Capacity-RNA-to-cDNA kit (Thermo Fisher, 4387406). Gene expression was measured by qPCR using the Power SybrGreen Master mix (Thermo Fisher, 4367659). All quantitative polymerase chain reaction (PCR) results were calculated relative to the mean of the housekeeping gene *Gapdh*. The average of two technical replicates was used for each biological data point. Primer sets for quantitative reverse transcription PCR (q-RT-PCR) analyses are shown in Table 3. S5.

Immunocytochemistry. C2C12 cells cultured on a sterilized cover slip in 6-well plates (Greiner bio-one, CELLSTAR, 657160) were fixed in Fixx solution (Thermo Scientific, 9990244) for 15 min and permeabilized in 0.1% Triton X-100 (Amresco, 0694) solution for 15min at 20ºC. Cells were blocked in 3% BSA for 1h at 20ºC to avoid unspecific antibody binding and then incubated with primary antibody over night at 4ºC with gentle shaking. MyHC was stained using the MF20 primary antibody (1:200, Invitrogen, 14-6503-82) for C2C12 cells and in Lonza muscle cells with a MYL2 antibody (1:140, Abcam, ab79935). The next day cells were incubated with secondary antibody (Thermo Fisher #A10037 for MF20 and #A-21206 for MYL2) for 1h at 20ºC and nuclei were labelled with DAPI. The immunofluorescence images were acquired using either fluorescence or confocal microscopy. The myofusion index was calculated as the ratio of nuclei within myotubes to total nuclei. The myotube diameter was measured for 8 myotubes per image using ImageJ. Myotube area was calculated as the total area covered by myotubes.

Gene expression and phenotype analysis in BXD mouse population. Quadriceps microarray data (Affymetrix Mouse Gene 1.0 ST) and phenotype data from BXD mouse genetic reference population (*201*) were analyzed for Pearson correlations with R software. The first principal component of the ceramide biosynthetic pathway representing its expression in muscle was calculated by including the following genes: *Sptlc1, Sptlc2, Kdsr, Cers1, Cers2, Cers3, Cers4, Cers5, Cers6, Degs1*.

Quadriceps transcript profiling using RNA sequencing. Quadriceps muscles were collected and snap-frozen in liquid nitrogen from C57Bl/6JRj mice undergoing intraperitoneal myriocin treatment for 10 weeks on a chow diet starting at the age of 18 months. RNA was isolated using Direct-zol RNA kit (Zymo, Irvine, CA). RNA quality was assessed using Agilent 2100 BioAnalyzer (Agilent, Santa Clara, CA). Samples with RIN ≥ 8, 28S/18S ≥ 1.0, and c ≥ 20 ng/µL were included in analyses. Using these criteria, 9 (4 DMSO and 5 myriocin) samples passed and 2 samples failed to pass quality control criteria. Sequencing libraries were prepared by BGI genomics using the DNBseq^{TM} technology. Paired end sequencing with 100 cycles was performed using the BGISEQ-500 instrument. After removal of adaptor sequences and low quality reads, we obtain at least 56 million reads per sample. SOAPnuke was used to obtain clean reads (parameters -l 15, -q 0.2, -n 0.05). Reads were mapped using STAR aligner version 2.5.2b using the mouse GRCm38 genome assembly and the release 91 GTF annotation from Ensembl. Htseq-count version 0.6.0 was used to count the number of reads mapping to genes (mode= union, type=exon, idattr=gene_id). Transcript displaying higher expression than $\log_2$(CPM+1) > 0.5 in at least 3 samples were included in analyses. Differential gene expression analysis and expression normalization was performed using using voom, 'variance modeling at the observational level' (*219*), adjusting for sacrifice date. At individual gene level, no gene passed the multiple testing correction threshold. Benjamini-Hochberg correction for multiple testing was used. For gene set enrichment analysis using gene ontology (GO) categories, transcripts were ordered according to their $\log_2$-transformed fold change, and 100,000 permutations were used. Adjusted p-value < 0.05

was considered significant. Upon publication, data will be deposited in a public repository, such as Gene Expression Omnibus database.

Human studies

Young vs. old skeletal muscle microarrays. Gene expression analysis of young vs. old human muscle biopsies was obtained from publicly available dataset GSE25941 (*220*). Briefly, a total of 36 subjects were included in the study. The young (n=15, 25±1y) participants included 7 males and 8 females. The old (n=21, 78±1y) participants included 10 males and 11 females. All subjects were healthy and had never been involved in any formal exercise. Skeletal muscle biopsies were obtained from the vastus lateralis in the basal state. Affymetrix Human Genome U133 Plus 2.0 Array platform was used to perform the microarray analysis.

Skeletal muscle gene expression in Genotype-Tissue Expression (GTEx) project. For RNA gene expression analyses, we employed 491 post-mortem skeletal muscle biopsies from the GTEx gene expression collected as described (*221*). As measures of gene expression, we used residual expression levels of transcripts adjusting for the published GTEx v7 covariates. As for eQTL analyses, we used the GTEx v7 genotypes (dbGAP, approved request #10143-AgingX).

Senior fitness phenotypes in Helsinki Birth Cohort Study (HBCS). The HBCS includes 13,435 individuals born in Helsinki between 1934 and 1944. The clinical study protocol was approved by the Ethics Committee of Epidemiology and Public Health of the Hospital District of Helsinki and Uusimaa. Written informed consent was obtained from each participant before any study procedure was initiated. The senior fitness test (SFT) describing the physical performance of the participants was performed to 695 individuals as previously described (*222*) (Table 3. 1). Here, we used a modified test battery, consisting of five components of the SFT: number of full arm stands in 30 seconds with arms folded across chest to assess lower body strength; number of biceps curls in 30 seconds while holding a hand weight (3 kg for men and 2 kg for women) to assess upper body strength; chair sit and reach to assess the lower body flexibility (from sitting position with leg extended at front of chair and hands reaching toward toes, number of cm (plus/minus) from extended fingers to tip of toe); number of meters walked in 6 minutes to measure aerobic endurance; and back scratch to assess upper body flexibility (with one hand reaching over shoulder and the other one up middle of back, distance (in cm) between extended middle fingers (plus/minus)). The result of each test was expressed as age (for each 5-year group) and sex-standardized percentile scores. An overall test score was calculated by summarizing the normalized scores of the 5 SFT components. Isometric grip strength of the dominating hand was tested by a Newtest Grip Force dynamometer (Newtest Oy, Oulu, Finland). The maximum value of three squeezes was used in analyses.

DNA was extracted from blood samples and genotyping was performed with the modified Illumina 610k chip by the Wellcome Trust Sanger Institute, Cambridge, UK, according to standard protocols. Genomic coverage was extended by imputation using the 1000 Genomes Phase I integrated variant set (v3 / April 2012; NCBI build 37 / hg19) as the reference sample and IMPUTE2 software. Before imputation the following QC filters were applied: SNP clustering probability for each genotype > 95%, Call rate > 95% individuals and markers (99% for markers with MAF < 5%), MAF > 1%, HWE $P > 1x10^{-6}$. Moreover, heterozygosity, gender check and relatedness checks were performed and any discrepancies removed.

Genetic association analyses in GTEx and HBCS studies. For the combined expression of *SPTLC1* and *SPTLC2* in skeletal muscle in GTEx data, we used the mean of the residual expression. For identification of *cis*-eQTLs we analyzed eQTLs ±1 Mb from the start and the end of *SPTLC1* and *SPTLC2*. SNPs with minor allele frequency > 10% were included, and SNPs with $r^2 > 0.2$ were incorporated in the same haploblock based on linkage disequilibrium information from the version 5 of the 1000 Genomes Project in Finns (*223*). As there were 4 haploblocks within both *SPTLC1* and *SPTLC2* region (300 kb), we used Bonferroni correction for 25 haploblocks ($P < 0.002$) within the 2 Mb region studied for identification of *cis*-eQTLs.

For phenotype associations in the HBCS, the scores of the fitness tests were classified based on 5th percentile range, with a score 1 being the worst performance (score below 5th percentile), 2 the score from the 5th to 9th percentile, and 20 the best performance (in or above the 95th percentile) as described (*208*). To reduce confounding effects, diabetics were not included in analyses. We performed linear regressions with SNPtest assuming an additive genetic model. We adjusted all models for age, sex, highest education achieved (basic or less/upper secondary/lower tertiary/upper tertiary) and smoking (yes/no).

3.6 Acknowledgments

We wish to thank the staff of EPFL histology, flow cytometry, and animal facilities for technical assistance. The work in the JA laboratory was supported by grants from the Ecole Polytechnique Federale de Lausanne (EPFL), the European Research Council (ERC-AdG-787702), the Swiss National Science Foundation (SNSF 31003A_179435), the Fondation Suisse de Recherche sur les Maladies Musculaires (FSRMM) and the Fondation Marcel Levaillant (190917). We thank all study participants as well as everybody involved in the Helsinki Birth Cohort Study. The work has been supported by Academy of Finland, the Finnish Diabetes Research Society, Folkhälsan Research Foundation, Novo Nordisk Foundation, Finska Läkaresällskapet, Finnish Foundation for Cardiovascular Research, Juho Vainio Foundation, Signe and Ane Gyllenberg Foundation, University of Helsinki, Sigrid Juselius Foundation, Ministry of Education, Ahokas Foundation, Emil Aaltonen Foundation, Paavo Nurmi Foundation, Orion Foundation, and Scottish Senior Clinical Fellowship (SCD/09). We would also like to acknowledge the Genetics Core of the Wellcome Trust Clinical Research Facility (Edinburgh, UK) who ran the 450k array for the HBCS samples. PPL was a recipient of Sigrid Juselius Fellowship.

3.7 TABLE

Table 3. 1. Clinical characteristics of the Helsinki Birth Cohort Study

Characteristic	Mean or %	SD
N	826	
Women (%)	59	
Age (years)	71	2.7
BMI (kg/m^2)	27	4.5
Waist-hip-ratio	0.96	0.08
Systolic blood pressure (mmHg)	156	22
Diastolic blood pressure (mmHg)	85	10.8
Total cholesterol (mmol/L)	5.42	1.02
Diabetic (%)	15	
SFT	45.4	17.3
6-min walk (m)	572	105
Back scratch (cm)	-3.56	4.85
Chair stand (#)	11.4	2.22
Sit and reach (cm)	-0.44	4.89
Arm curl (#)	15.7	3.52
Grip strength (N); N=1538	303	117

3.8 SUPPLEMENTARY Materials

Figure 3. S1. Sphingomyelin and deoxysphingolipid levels in skeletal muscle in aging and upon myriocin treatment.

Figure 3. S2. Inhibition of sphingolipid *de novo* synthesis increases MuSC proliferation and tissue count.

Figure 3. S3. Sphingolipid depletion improves MuSC function and muscle regeneration *in vivo*.

Figure 3. S4. Single clone CRISPR-Cas9 mediated *Sptlc1* knockout promotes muscle cell differentiation in C2C12 myoblasts in a dose-dependent manner.

Figure 3. S5. Linkage disequilibrium (LD) structure of *cis*-eQTL of human *SPTLC1* and *SPTLC2*.

Table 3. S1. *Cis*-eQTLs of *SPTLC1* in skeletal muscle.

Table 3. S2. *Cis*-eQTLs of *SPTLC2* in skeletal muscle.

Table 3. S3. Association of skeletal muscle transcripts of neighboring genes with *SPTLC1* *cis*-eQTL rs10820917. NES, normalized effect size.

Table 3. S4. Association of skeletal muscle transcripts of neighboring genes with *SPTLC2* *cis*-eQTL rs8013312. NES, normalized effect size.

Table 3. S5. List of mouse primers.

Table 3. S6. List of guide RNAs.

Table 3. S7. List of plasmids.

Table 3. S8. List of antibodies.

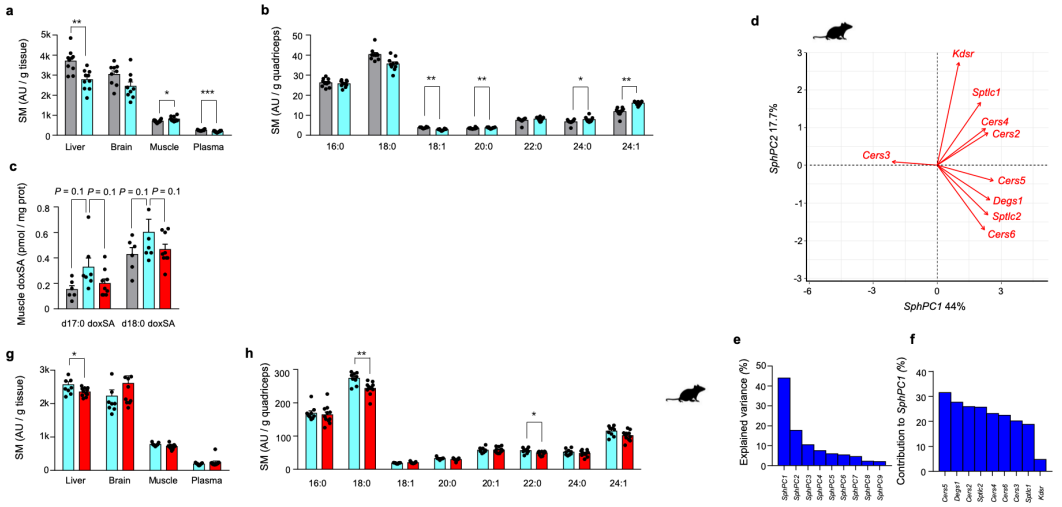

Figure 3. S1. Sphingomyelin and deoxysphingolipid levels in skeletal muscle in aging and upon myriocin treatment. Concentrations of total sphingomyelin (SM) in liver, brain, skeletal muscle, and plasma of young (8-week old, n=10) and aged (24-month-old, n=10) C57BL/6JRj mice (**a**), and concentrations of individual sphingomyelin species in quadriceps of young and aged (**b**) C57BL/6JRj mice. Concentrations of 1-deoxysphinganine (**c**) in quadriceps muscle of young, aged, and aged mice treated with myriocin. (**d**) A factor loading plot (biplot) showing the effects of the enzymes of sphingolipid *de novo* synthesis pathway on two first principal components (*SphPC1* and *SphPC2*) in BXD mouse skeletal muscle. (**e**) Proportion of variance explained by each principal component of the sphingolipid *de novo* synthesis pathway. (**f**) Contribution of each transcript to the *SphPC1* in mouse skeletal muscle (BXD). Concentrations of total sphingomyelin in liver, brain, muscle, and plasma (**g**), and individual sphingomyelin species (**h**) in quadriceps muscle of aged mice and aged mice treated with myriocin. All data are shown mean ± SEM. n=6-10 per group. **P* < 0.05, ***P* < 0.01, and ****P* < 0.001 with Student's two-tailed T test.

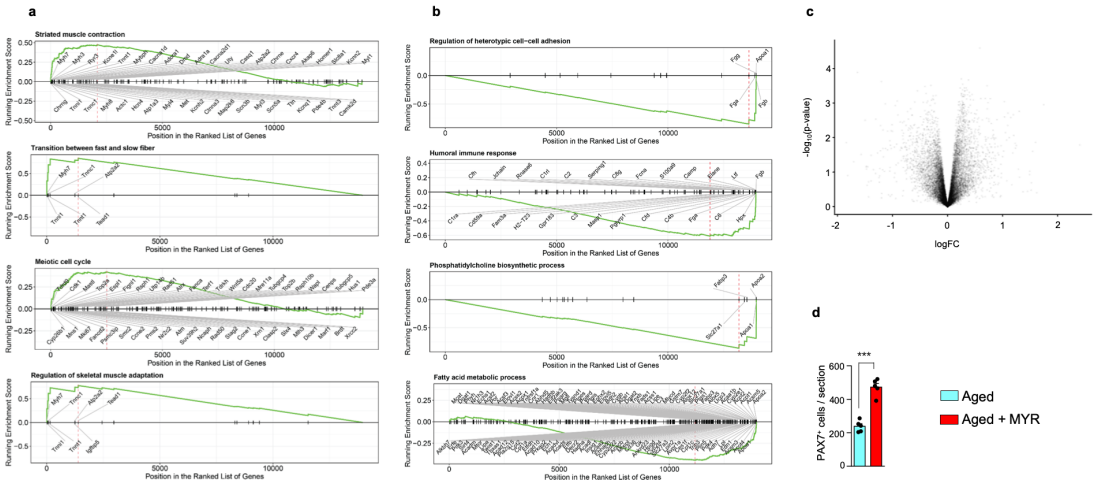

Figure 3. S2. Inhibition of sphingolipid *de novo* synthesis increases MuSC proliferation and tissue count. Upregulated (**a**) and downregulated (**b**) GO categories in quadriceps muscle of aged C57BL/6JRj mice with myriocin treatment started at 18 months of age in RNA sequencing. (**c**) Volcano plot of individual genes displaying log of nominal p-value (vertical axis) and $\log_2$ fold change (horizontal axis) in quadriceps of myriocin treated mice. (**d**) Quantification of PAX7 positive cells per section in TA muscle in aged mice and aged mice treated with myriocin. All data are shown mean ± SEM. ****P* < 0.001 with Student's two-tailed T test.

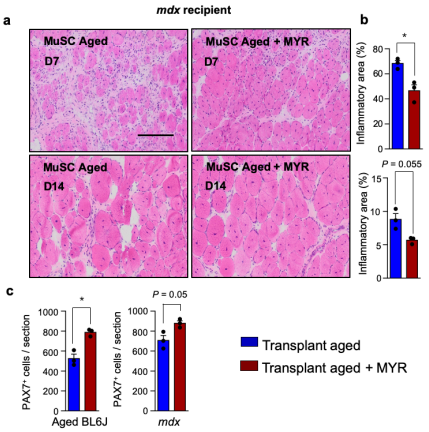

Figure 3. S3. Sphingolipid depletion improves MuSC function and muscle regeneration *in vivo*. Aged 18-month-old C57BL/6JRj mice were treated with myriocin, and upon sacrifice, freshly isolated MuSCs were transplanted to either aged C57BL/6JRj or *mdx* mice. Representative images (**a**) and quantification of inflammatory area (**b**) of H&E stained TA from *mdx* recipients at 7 days and 14 days after transplantation. Scale bar, 50 µm. (**c**) Quantification of PAX 7 positive cells per section in aged C57BL/6JRj and *mdx* recipient mice. All data are shown mean ± SEM. **P* < 0.05, ***P* < 0.01, and ****P* < 0.001 with Student's two-tailed T test.

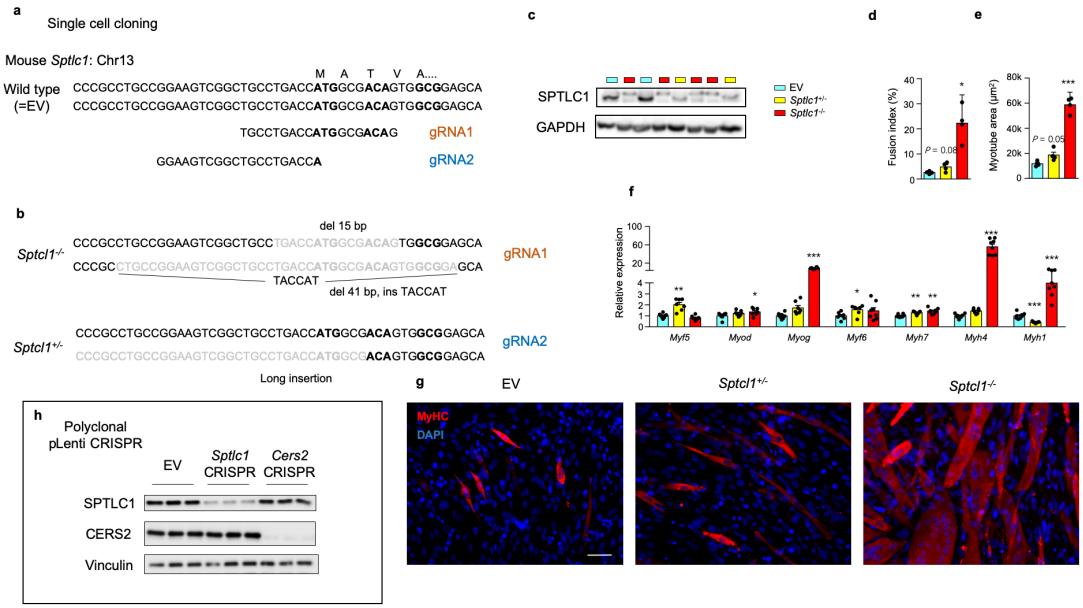

Figure 3. S4. Single clone CRISPR-Cas9 mediated *Sptlc1* knockout promotes muscle cell differentiation in C2C12 myoblasts in a dose-dependent manner. (a) Location of guide RNA (gRNA) binding sites in *Sptlc1* for two different gRNAs, gRNA1 and gRNA2. (b) Changes in DNA induced by gRNA1 and gRNA2 in C2C12 myoblasts. gRNA1 transfection induced deletions in two homologous chromosomes resulting in a homozygous *Sptlc1* knockout (*Sptlc1*$^{-/-}$). gRNA2 induced a long insertion in one homologous chromosome leaving the other chromosome intact, resulting in a heterozygous knockout (*Sptlc1*$^{+/-}$). (c) Verification of *Sptlc1*$^{+/-}$ and *Sptlc1*$^{-/-}$ knockout C2C12 cell lines using Western blot. Fusion index (d), myotube diameter (e), transcript expression of myogenesis markers (f), and immunocytochemistry (g) from C2C12 myoblasts with heterozygous and homozygous loss-of-function of *Sptlc1* using single clone CRISPR-Cas9. Scale bar, 50 µm. (h) Polyclonal silencing of *Sptlc1* and *Cers2*. Verification of knockouts using Western blot. All data are shown mean ± SEM. **P* < 0.05, ***P* < 0.01, and ****P* < 0.001 with Student's two-tailed T test.

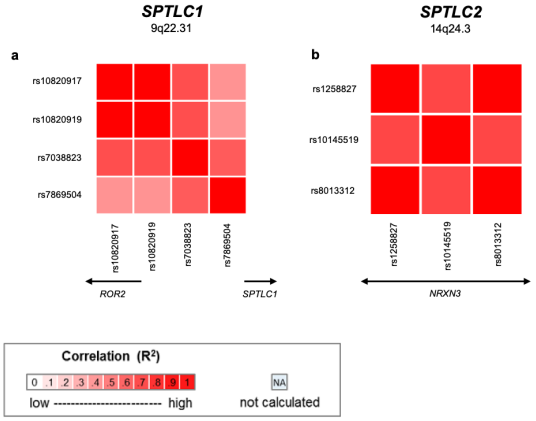

Figure 3. S5. Linkage disequilibrium (LD) structure of *cis*-eQTL of human *SPTLC1* and *SPTLC2*. (**a**) LD structure of *SPTLC1* (**a**) and *SPTLC2* (**b**) *cis*-eQTLs denoted by r^2 measurements rom Phase 3 (Version 5) of the 1000 Genomes Project.

Table 3. S1. *Cis*-eQTLs of *SPTLC1* in skeletal muscle

SPTLC1	rs10820917		rs10820919		rs7869504		rs7038823	
	β	*P*	*β*	*P*	*β*	*P*	*β*	*P*
SPTLC1 mRNA	-0.088	0.001 9	-0.088	0.001 9	-0.084	0.0012	-0.084	0.0015
SFT	2.99	0.04	2.99	0.04	0.50	0.69	1.74	0.21
6-min walk	0.99	0.03	0.99	0.03	0.74	0.06	1.00	0.02
Back scratch	-0.12	0.81	-0.12	0.81	-0.52	0.24	-0.40	0.41
Chair stand	0.58	0.076	0.58	0.077	0.21	0.44	0.31	0.31
Sit and reach	0.61	0.23	0.61	0.24	0.06	0.89	0.25	0.60
Arm curl	0.99	0.01	0.99	0.01	0.01	0.98	0.62	0.098
Grip strength	0.99	0.004 7	0.99	0.004 6	0.33	0.29	0.84	0.0079

Table 3. S2. *Cis*-eQTLs of *SPTLC2* in skeletal muscle

SPTLC2	rs8013312		rs10145519		rs12588277	
	β	*P*	*β*	*P*	*β*	*P*
SPTLC2 mRNA	-0.13	0.001 4	-0.13	0.002	-0.12	0.002
SFT	4.64	0.003 6	4.80	0.005 3	4.35	0.006

	1.51	0.002	1.36	0.012	1.40	0.005
6-min walk		7				
Back scratch	1.38	0.013	1.38	0.021	1.37	0.01
Chair stand	0.43	0.22	0.24	0.54	0.36	0.31
Sit and reach	1.27	0.02	1.71	0.004	1.21	0.029
Arm curl	0.03	0.94	0.13	0.78	-0.013	0.98
Grip strength	0.38	0.33	0.63	0.13	0.48	0.22

Characteristic	Mean or %	SD
N (Men/women)	826 (339/487)	
Age (years)	71	2.7
SFT	45.4	17.3
6-min walk (m)	572	105
Back scratch (cm)	-3.56	4.85
Chair stand (#)	11.4	2.22
Sit and reach (cm)	-0.44	4.89
Arm curl (#)	15.7	3.52
Grip strength (N); N=1538	303	117

Table 3. S3.
Association of skeletal muscle transcripts of neighboring genes with *SPTLC1* *cis*-eQTL rs10820917. NES, normalized effect size.

SPTLC1 rs10820917	NES	*P*
ASPN	-0.013	0.7
AUH	-0.014	0.67
BICD2	0.023	0.32
CENPP	0.0043	0.93
ECM2	-0.018	0.53
FGD3	-0.015	0.76
IARS	-0.027	0.37
IPKK	0.039	0.24
NFIL3	-0.013	0.64
NOL8	0.0025	0.93
ROR2	0.089	0.099
SPTLC1	0.088	0.0019
SUSD3	-0.0098	0.87
ZNF484	-0.00012	1

Table 3. S4.
Association of skeletal muscle transcripts of neighboring genes with *SPTLC2* *cis*-eQTL rs8013312. NES, normalized effect size.

SPTLC2 rs8013312	NES	*P*
ADCK1	-0.026	0.44
AHSA1	0.056	0.1
ANGEL1	0.0037	0.92
GSTZ1	0.034	0.28
IRF2BPL	-0.0038	0.92
NRXN3	0.004	0.94
SLIRP	-0.016	0.45
SNW1	-0.0019	0.92
SPTLC2	0.13	0.0014
TMED8	0.0013	0.97
TMEM63C	-0.053	0.3
VASH1	-0.024	0.48
VIPAS39	0.011	0.71
ZDHHC22	-0.065	0.22

Table 3. S5. List of mouse primers.

Gene symbol (mouse)	Forward	Reverse
Myod1	AGCACTACAGTGGCGACTC	GTGGAGATGCGCTCCACT
Pax7	TCTCCAAGATTCTGTGCCGAT	CGGGGTTCTCTCTCTTATACTCC
Myf5	TGAGGGAACAGGTGGAGAAC	TGGAGAGAGGGAAGCTGTGT
Myog	TTGCTCAGCTCCCTCAACCAGGA	TGCAGATTGTGGGCGTCTGTAGG
Myf6	AGATCGTCGGAAAGCAGC	CCTGGAATGATCCGAAACAC
Myh4	ACAAGCTGCGGGTGAAGAGC	CAGGACAGTGACAAAGAACG
Myh1	CCAAGTGCAGGAAAGTGACC	AGGAAGAGACTGACGAGCTC
Myh7	GTGGCTCCGAGAAAGGAAG	GAGCCTTGGATTCTCAAACG
B2m	TTCTGGTGCTTGTCTCACTG	TATGTTCGGCTTCCCATTCT

Table 3. S6. List of guide RNAs.

Guide RNA symbol (mouse)	gRNA sequence
Sptlc1 gRNA1	(G)TGCCTGACCATGGCGACAG
Sptlc1 gRNA2	GGAAGTCGGCTGCCTGACCA
Cers2 gRNA1	GTTAAGGAGAAAACCCGACTG
Cers2 gRNA2	(G)CTGGACGCCAGGTAGAACGC

Table 3. S7. List of plasmids.

Plasmid	Reference
Lenti CRISPR v2	Addgene # 52961
Lenti CRISPR v2 Sptlc1 gRNA1	Current study
Lenti CRISPR v2 Sptlc1 gRNA2	Current study
Lenti CRISPR v2 Cers2 gRNA1	Current study
Lenti CRISPR v2 Cers2 gRNA2	Current study
psPAX2	Addgene # 12260
pMD2G	Addgene # 12259

Table 3. S8. List of antibodies.

Antibody	Supplier	Reference #
SPTLC1 Rabbit polyclonal	ProteinTech Group	15376-1-AP
CERS2 Rabbit polyclonal	Sigma	HPA027262
Vinculin Rabbit monoclonal	Abcam	ab129002
Myosin 4 Monoclonal (MF20)	ThermoFisher Scientific	# 14-6503-82
Anti-Myosin light chain 2	Abcam	ab79935
Dystrophin	Spring Bioscience	#E2660
Laminin	Sigma	#L9393
PAX7	DSHB, University of Iowa	See supplier URL
MYOD	LabForce	#sc-377460
MYOG	Santa Cruz	#sc-13137
eMyHC	DSHB, University of Iowa	See supplier URL
CD31 (1:800, eBioscience, eFluor450 conjugated)	eBioscience	# 48-0311-82
CD45 (1:200, eBioscience, eFluor450 conjugated)	eBioscience	# 48-0459-42
Donkey anti-Mouse IgG secondary antibody	ThermoFisher Scientific	# A10037
Donkey anti-Rabbit IgG secondary antibody	ThermoFisher Scientific	# A-21206

Chapter 4. Reduction of sphingolipid *de novo* synthesis counteracts muscular dystrophy

This paper is under preparation.

Peiling Luan[1]†, Pirkka-Pekka Laurila[1]†, Nadège Zanou[2], Nicolas Place[2], Johan Auwerx[1]*

Affiliation:

[1]*Laboratory for Integrative and Systems Physiology, Institute of Bioengineering, Ecole Polytechnique Fédérale de Lausanne (EPFL), CH-1015 Lausanne, Switzerland;* [2]Institute of Sport Sciences, Department of Physiology, Faculty of Biology-Medicine, University of Lausanne, Lausanne, Switzerland

*Correspondence to Johan Auwerx at admin.auwerx@epfl.ch

† These authors contributed equally to this work.

4.1 Abstract

Duchenne muscular dystrophy (DMD) is a severe muscle disorder that affects one of every 3500 newborn boys, leading to muscle weakness and premature death following cardiac or respiratory failure. Here, we established the link between sphingolipids and muscular dystrophy. Sphingolipid biosynthesis pathways are upregulated in dystrophic muscles, and the pharmacological inhibition of sphingolipid *de novo* synthesis effectively prevents DMD-associated decline in muscle function and coordination. Sphingolipid depletion by myriocin restores Ca^{2+} homeostasis, improves MuSC microenvironment and MuSC regenerative capacity, and reduces general inflammation and fibrosis, ultimately resulting in the amelioration of DMD symptoms. Importantly, we have revealed for the first time the role of sphingolipid metabolism in macrophage polarization by showing that blockade of sphingolipid biosynthesis skews macrophages to the M2-phenotype in dystrophic muscles, reconstructing the balance between M1 and M2 macrophages. These findings identify sphingolipid depletion as an attractive therapeutic strategy for the management of DMD and other neuromuscular dystrophies.

4.2 Introduction

The persistent contraction and relaxation of skeletal muscles necessitates mechanisms that maintain the integrity of muscle membranes (*11, 224*). Dystrophin, encoded by the *DMD* gene, is a scaffolding protein that supports muscle structure by anchoring the cytoskeleton with sarcolemma. Muscular dystrophies are a heterogeneous group of inherited genetic diseases, characterized by loss of membrane integrity and muscle weakness and degeneration. Duchenne muscular dystrophy (DMD) is the most common muscular dystrophy affecting 1 in 3500 newborn boys, and is caused by one of the thousands of identified mutations in *DMD* gene (*225*). Patients diagnosed with the DMD often experience premature death due to heart or respiratory failure following protracted muscle degeneration in the heart and diaphragm (*225*). Currently, there is no cure for DMD. Despite recent advances in CRISPR/Cas9 mediated gene editing (*226*), the high allelic heterogeneity of the disease and the safety concerns of recent clinical trials (*227*) present challenges to gene therapy, suggesting that pharmacological treatment would be needed to complement these therapies as well as to help manage patients with mutations unsuitable for gene editing technologies.

Numerous biological pathways contribute to the pathophysiology of DMD. Compromised membrane integrity, aberrant calcium homeostasis, chronic inflammation, fibrosis, and impaired tissue remodeling are pathological hallmarks of the disease (*228*). Although efforts to target these pathways individually including restoration of Ca^{2+} homeostasis with Ca^{2+} channel blockers (*229*) and muscle mass with anabolic steroids (*230*) have been subject to clinical trials, they have not produced clinical benefits relevant for the overall course of the disease. Glucocorticoids with their immunosuppressive effects are currently the only pharmacological treatment for DMD incorporated the treatment guidelines (*231-233*), and even their efficacy is suboptimal and side effects are considerable. Optimally, treatment strategies would not only target one, but several pathways involved in DMD pathogenesis. The high prevalence, the debilitating nature, and premature mortality of the disease, call for urgent efforts to develop new disease-modifying treatment strategies for DMD.

Sphingolipids are bioactive lipids with pleiotropic functions, including inflammation, fibrosis and cell death (*108*). Ceramides serve as the central intermediate of sphingolipid metabolism; ceramides can be synthesized from serine and palmitate through the sphingolipid *de novo* synthesis pathway (*108*). Increased ceramide levels have been implicated in many diseases, including Alzheimer's disease, cardiovascular disease and diabetes (*110*). In recent years, a particular interest has emerged in selectively blocking the generation of sphingolipids to combat diseases characterized by abnormal sphingolipid metabolism, such as ageing and the metabolic syndrome. For example, recent studies from our lab have demonstrated that ceramides accumulate in skeletal muscles upon ageing, and pharmacological inhibition of serine palmitoyltransferase (SPT), the initiating and rate-limiting enzyme of sphingolipid *de novo* biosynthesis pathway, reverses age-related sarcopenia (chapter 3). Furthermore, it was shown that skeletal muscles also accumulate sphingolipids in obesity (*234*) and depletion of muscular sphingolipids ameliorates obesity-induced insulin resistance and improves glucose homeostasis in animals fed with high-fat diet (*235*). While intensive research efforts have focused on exploring the role of sphingolipid depletion in treating metabolic disorders or attenuating ageing, the role of sphingolipids in muscular dystrophy still remains unproven. DMD shares many biological pathways with these disorders, calling for testing whether inhibition of sphingolipid *de novo* synthesis pathway, which has many effects in cellular physiology, could restore muscle function in DMD.

In the present study we establish the link between muscular dystrophies and sphingolipid metabolism. We demonstrate that the enzymes involved in the sphingolipid *de novo* synthesis pathway are upregulated in dystrophic muscles. Inhibition of sphingolipid *de novo* synthesis by myriocin, a highly selective inhibitor of SPT, counteracts DMD-related loss in muscle function and coordination in mice. Sphingolipid depletion stabilizes muscular Ca^{2+} turnover, reverses diaphragmatic and cardiac fibrosis, and attenuates DMD-associated muscle inflammation by directing macrophage polarization towards anti-inflammatory M2 macrophages. Given that

pharmacological sphingolipid reduction alleviated dystrophic symptoms and reversed multiple pathophysiological hallmarks of DMD, we propose that inhibition of sphingolipid *de novo* synthesis could be an attractive therapeutic strategy to treat muscular dystrophies.

4.3 Results

4.3.1 Sphingolipid metabolism is dysregulated in skeletal muscle in DMD

The sphingolipid *de novo* synthesis pathway produces ceramides and other sphingolipids by using fatty acids and amino acids as substrates. Serine palmitoyltransferase (SPT) is the first and rate-limiting enzyme of the pathway, generating 3-ketosphinganine, which is rapidly converted to sphinganine. The conversion of sphinganine to dihydroceramide is achieved by one of the 6 mammalian ceramide synthases (CERS1-6), of which each has a specificity for acyl chains of different lengths. The most abundant ceramide synthase in muscle is CERS2. To evaluate the role of sphingolipid *de novo* synthesis pathway in muscular dystrophies, we compared the transcript abundance of enzymes of the sphingolipid *de novo* synthesis pathway in a publicly available dataset featuring muscle biopsies from different muscular dystrophies and neuromuscular diseases (*150*). Across all the muscle diseases, including DMD, Becker muscular dystrophy (BMD), Emery-Dreifuss dystrophy (EDMD) and Facioscapulohumeral muscular dystrophy (FSHD), we observed a universal upregulation of sphingolipid biosynthetic enzymes (Fig. 4. 1A). These findings suggest that sphingolipid *de novo* synthesis pathway is associated with muscle dysfunction.

DMD is the most common muscular dystrophy, and along with acute quadriplegic myopathy (AQM), it presented the most significant upregulation of sphingolipid biosynthesis pathway in muscle (Fig. 4. 1A). The findings were reproduced in another dataset (*236*), pointing that subunits of SPT (SPTLC1 and SPTLC2) along with CERS2, the most abundant ceramide synthase in skeletal muscle, were the enzymes in the *de novo* sphingolipid biosynthesis pathway that were most consistently changed (Fig. 4. 1B). Interestingly, in an additional dataset (*152*) consisting of boys with confirmed genetic diagnosis of DMD, but in which biopsies were obtained before the onset of symptoms, we observed an upregulation of sphingolipid *de novo* synthesis pathway (Fig. 4. 1C), indicating that the pathway is already deregulated in the early stages of the pathogenesis of DMD, and not just a mere reactive response to onset of symptoms.

Primary myoblast cells, derived from patients affected with DMD, were utilized to further examine DMD-associated deficits in sphingolipid metabolism. Compared to control subjects, in DMD myoblast cells specific transcripts encoding enzymes of the sphingolipid biosynthesis pathway were induced (Fig. 4. 1D), probably underpinning the accumulation of ceramides in these dystrophic cells. The only downregulated gene in the sphingolipid biosynthesis was *CERS1* (Fig. 4. 1D), which was consistent with the data obtained from human patient biopsies (Fig. 4. 1A-C).

Consistent with these data obtained in human myoblasts and in muscle biopsies of DMD patients, in *mdx* mice, which are deficient of *Dmd* gene, the expression of SPTLC1, 2 and the CERS2 proteins was remarkably higher than that in wild type C57BL/10SnJ mice (Fig. 4. 1E). In general, our data indicate that dysregulated sphingolipid metabolism is a feature that typifies both mouse models of and patients with DMD and other neuromuscular dystrophies, which could result in the accumulation of ceramides in dystrophic muscles.

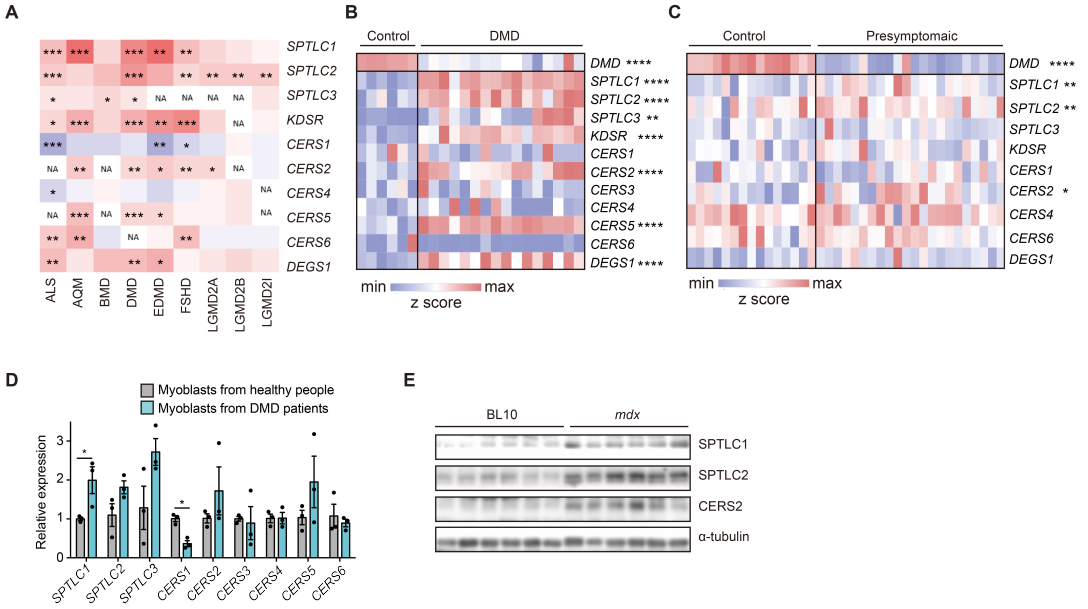

Fig. 4. 1. Sphingolipid metabolism is defective in human muscular dystrophy and in a mouse model of DMD. (**A**) Transcript abundance of sphingolipid synthesis associated enzymes from human muscle biopsies of patients affected with distinct neuromuscular dystrophies (GSE3307), normalized to healthy subjects. ALS (amyotrophic lateral sclerosis), AQM (acute quadriplegic myopathy), EDMD (Emery-Dreifuss dystrophy), FSHD (facioscapulohumeral muscular dystrophy), LGMD2A (limb-girdle muscular dystrophy type 2A), LGMD2D (limb-girdle muscular dystrophy type 2D) and LGMD2I (limb-girdle muscular dystrophy type 2I). (**B**) Transcript abundance of enzymes involved in the sphingolipid *de novo* synthesis pathway in human controls and patients affected by DMD from the dataset GSE38417 (n=16). **P $\leqslant$ 0.01, ****P $\leqslant$ 0.0001; by multiple two-way t-test. (**C**) Heatmap, showing the expression levels of the indicated genes that participate in the *de novo* synthesis of sphingolipids in pre-symptomatic DMD patients (GSE6011) (n=23). *$P \leq 0.05$, **P $\leqslant$ 0.01, ****P $\leqslant$ 0.0001; by multiple two-way t-test. (**D**) mRNA expression levels of *SPTLC1, SPTLC2, SPTLC3, CERS1, CERS2, CERS3, CERS4, CERS5* and *CERS6* in primary myoblasts from healthy human donors and DMD patients (n = 3 for both controls and DMD patients). All data are shown as mean ± SEM (error bars). *$P < 0.05$; **$P < 0.01$; ***$P< 0.001$; by two-way ANOVA. (**E**) Western blot analysis of sphingolipid *de novo* synthesis associated enzymes, including SPTLC1, SPTLC2, CERS2 and α-tubulin (as loading control), in TA muscles from C57BL/10SnJ mice and *mdx* mice treated with either DMSO or myriocin.

4.3.2 Inhibition of sphingolipid *de novo* synthesis restored muscle function in *mdx* mice

To test whether inhibition of *de novo* sphingolipid synthesis could rescue DMD-related muscle dysfunction, we treated *mdx* mice with myriocin or DMSO vehicle for four months; in addition, DMSO-treated C57BL/10SnJ mice were used as further controls (Fig. 4. 2A). Indeed, myriocin treatment improved the integrity of muscle structures, as evidenced by reduced level of serum creatine kinase (Fig. 4. 2B), and lower permeability of sarcolemma to Evans Blue (Fig. 4. 2C), indicating the membrane protective effects of myriocin administration.

Abnormal Ca^{2+} influx and release are hallmarks of DMD (*237*), primarily owing to the defects of Ca^{2+}- handling proteins, such as ryanodine receptor (RyR), a Ca^{2+} channel facilitating the release of Ca^{2+} from the sarcoplasmic reticulum (SR) into the cytosol, and the sarcoplasmic reticulum calcium ATPase (SERCA), an ion pump responsible for restoring SR Ca^{2+} stores by removing Ca^{2+} from the cytosol (*238*). As the protein levels of RyR1, SERCA1, and SERCA2 were similar in skeletal muscles of C57BL/10SnJ and *mdx* mice (Fig. 4. 2D) and myriocin treatment had no effect on these proteins (Fig. 4. 2D), we hypothesized that myriocin could restore the activity of Ca^{2+} channels in dystrophic muscles independent of protein abundance. To evaluate the performance of Ca^{2+}-release and -uptake channels, we isolated primary myofibers from WT, DMSO- and myriocin-treated *mdx* mice and stimulated them with caffeine to release Ca^{2+} from SR. The rapid caffeine-induced Ca^{2+} release observed in myofibers isolated from WT mice was blunted in *mdx* myofibers (Fig. 4. 2E, F), confirming the lower SR Ca^{2+} stores in dystrophic fibers resulted from the Ca^{2+} leak *via* RyR1 channel (*239*). Myriocin

treatment increased the amount of released Ca^{2+} (Fig. 4. 2E, F), indicating that myriocin treatment repairs the leaky RyR1 channel in *mdx* mice, hence restoring the SR Ca^{2+} content. After caffeine-triggered release of Ca^{2+}, WT myofibers pumped back 50% of cytosolic Ca^{2+} to SR while the mdx myofibers only transported back 20% (Fig. 4. 2E, G), suggesting impaired Ca^{2+} clearance from the cytosol in *mdx* mice. Myriocin treatment recovered the function of Ca^{2+}-uptake pumps, as demonstrated by the increased ability to transport Ca^{2+} from cytosol back to SR (Fig. 4. 2E, G). Overall, our results suggest that myriocin improves myocellular Ca^{2+} homeostasis in *mdx* mice by enhancing the activity of SR Ca^{2+} transport machinery.

Importantly, from a functional point angle, myriocin treated *mdx* mice showed improved exercise performance during treadmill exercise and muscle strength test, evidenced by the increased running time and distance (Fig. 4. 2H, I), and improved grip strength (Fig. 4. 2J). Moreover, *mdx* mice receiving myriocin also exhibited better muscular coordination, as shown by the improved performance in the rotarod test (Fig. 4. 2K). Thus, myriocin treatment effectively reversed DMD-associated decline in muscle function.

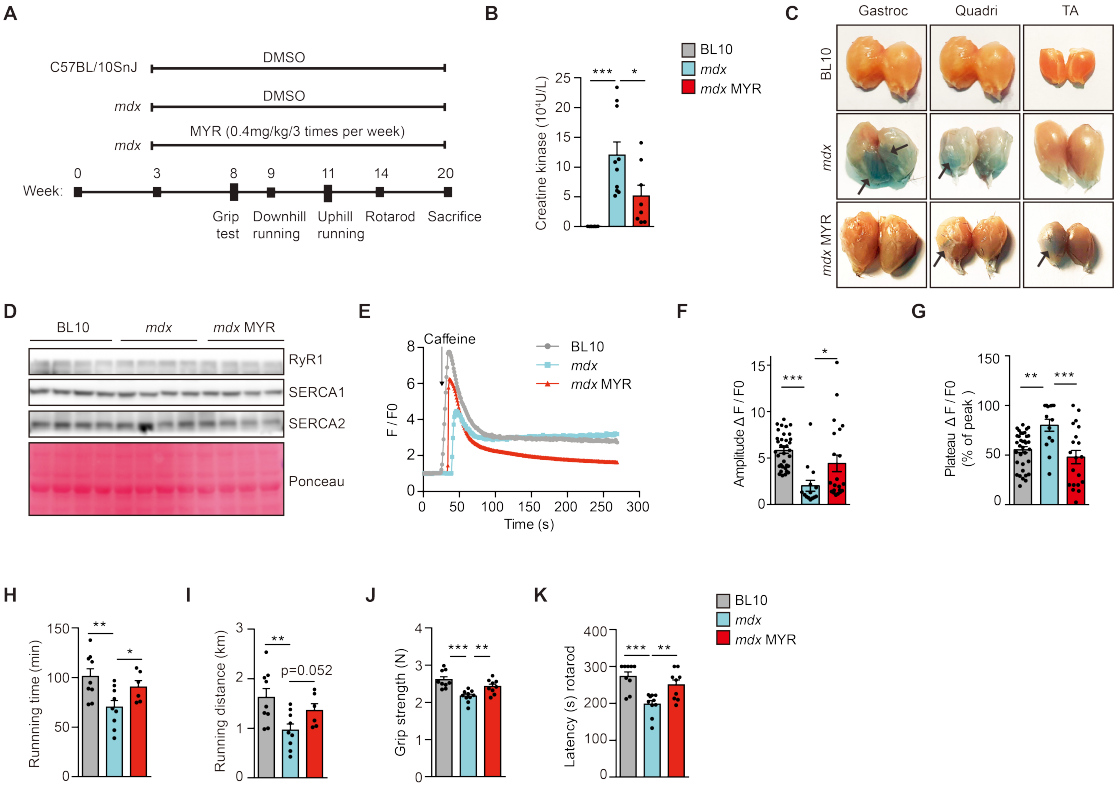

Fig. 4. 2. Inhibition of sphingolipid *de novo* synthesis restored integrity of muscle structures and improved muscle functions of *mdx* mice. (A) Summary of the mouse study on WT and *mdx* mice including dosage and duration of myriocin-treatment and the phenotyping pipeline. (B) Plasma creatine kinase level in animals treated as demonstrated in Fig. 4. 2A. (C) Evans blue dye staining of TA, quadriceps and gastrocnemius muscles of mice treated as in Fig. 4. 2A. (D) Western blot analysis of Ca^{2+} release associated proteins RYR1, and of Ca^{2+} reuptake proteins SERCA1 and SERCA2. (E) Cytosolic Ca^{2+} transients in isolated flexor digitorum brevis (FDB) fibers before and after 2.5mM caffeine stimulation. (F) Grouped data of $Ca2^{+}$ amplitude subtracting the baseline signal as shown in Fig. 4. 2E. **P* ≤ 0.05, ***P ⩽ 0.001; by one-way ANOVA test. (G) The mean fluorescence from 150 to 250s of the time lapse acquisition was calculated as a plateau of the Ca^{2+} curve. The Ca^{2+} curve plateau is expressed as a percentage of the peak signal shown in Fig. 4. 2E. **P ⩽ 0.01, ***P ⩽ 0.001; by one-way ANOVA test. Comparison of (H) maximal running distance and (I) duration between mice treated as described in Fig. 4. 2A (n=6-9). (J) Grip strength and (K) latency of rotarod test of the animals treated as described in Fig. 4. 2A. (n=6-9) **P* ≤ 0.05, **P ⩽ 0.01, ***P ⩽ 0.001; by one-way ANOVA test.

4.3.3 Myriocin improved muscle regeneration through recovering MuSC function in DMD

Impaired muscle function in DMD is tightly linked with abnormal muscle regeneration (*168*). Increased number of centronucleated fibers and the heterogeneity of myofiber area are hallmarks of defective regeneration in DMD (*240*). Histological analysis of tibialis anterior (TA) muscle (Fig. 4. 3A) revealed a pronounced reduction in the proportion of fibers with centralized nuclei, which represent fibers under regeneration, in myriocin-treated *mdx* mice (Fig. 4. 3B). In line with the decreased number of fibers with central nuclei, the distribution and average of the fiber minimal Feret's diameter and cross-sectional area were both increased by myriocin (Fig. 4. 3A, C-E). To sum up, this evidence indicates that myriocin could rescue muscle regeneration in *mdx* mice, leading to improved muscle morphology.

MuSCs are essential for muscle regeneration, and in DMD, exhaustion of MuSCs has been suggested to contribute to reduced regenerative ability of the muscle (*27*). To verify if myriocin is capable of replenishing the depleted MuSC pool in *mdx* mice, we isolated α7 integrin/CD34 double positive cells from the hindlimbs using fluorescence-activated cell sorting (FACS). The quantity of MuSCs was decreased in hindlimbs of *mdx* mice as compared to C57BL/10SnJ mice, and myriocin treatment restored the MuSC pool of *mdx* mice closed to that of WT mice (Fig. 4. 3F, G). Consistent with previous reports (*241*), *mdx* MuSCs partially lose the potential of self-renewal, manifested by a tendency towards decreased abundance of transcripts of *Pax7* (Fig. 4. 3H), a stemness marker of MuSCs. In contrast, *myogenin* (*Myog*), a well-established marker of myogenic differentiation, was strongly upregulated in *mdx* MuSCs (Fig. 4. 3H), suggesting that dystrophic MuSCs prefer terminal differentiation rather than self-renewal. The transcript levels of *Myod* and *Myf5,* the earliest markers of myogenic commitment, were not different between WT and dystrophic MuSCs. In addition to a deficiency in myogenic programs, dystrophic MuSCs also displayed a reduced ability to proliferate, as evidenced by a downregulation of *Ki67* and *CDK4* at the transcript level (Fig. 4. 3H). Myriocin rescued these alterations in transcript levels, by boosting the expression of *CDK4,* while downregulating *Myog* (Fig. 4. 3H) in dystrophic MuSCs. Interestingly, compared to MuSCs from WT mice, distinct enzymes involved in *de novo* sphingolipid synthesis were induced in *mdx* MuSCs except that *Cers1* is downregulated (Fig. 4. 3I), suggesting that aberrant sphingolipid metabolism also occurs in dystrophic MuSCs. Our findings indicate that myriocin is able to restore proliferation and myogenesis of MuSCs in *mdx* mice, consequently improving the regenerative capacity of dystrophic muscles.

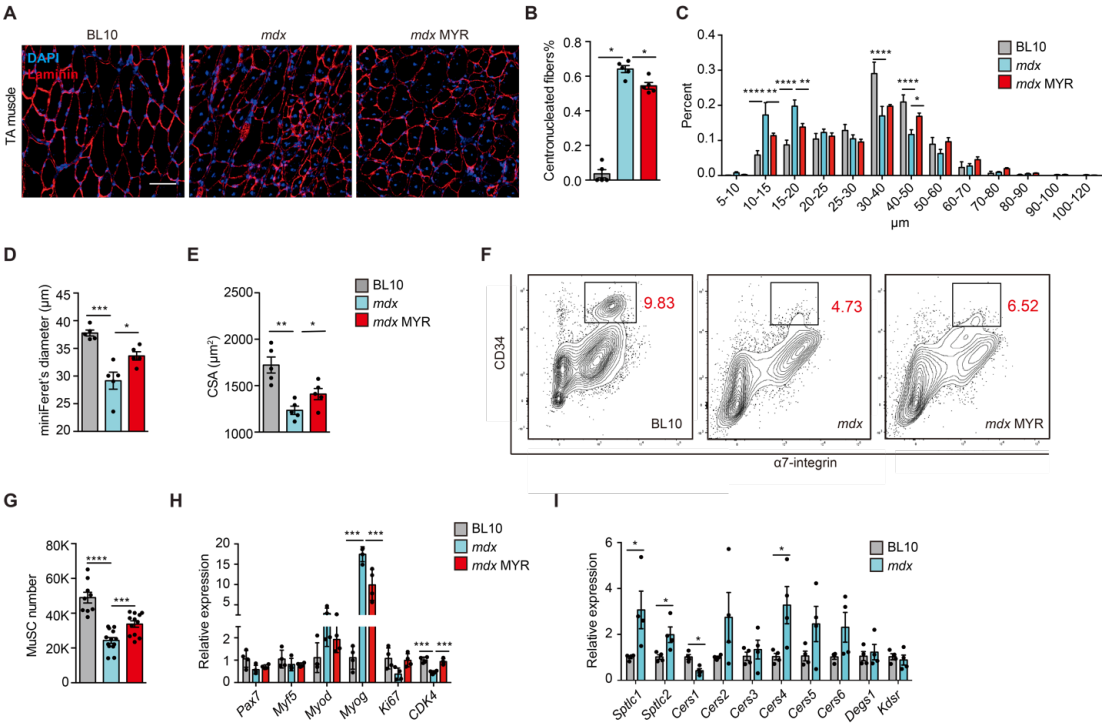

Fig. 4. 3. Myriocin rescued muscle regeneration and muscle stem cell functions in dystrophic animals. (**A**) Immunostaining of Laminin and DAPI in TA muscle of C57BL/10SnJ and *mdx* mice, showing the morphology of muscle fibers. (**B**) Proportion of fibers with centralized nuclei in WT, DMSO- and myriocin-treated *mdx* mice. (**C**)

Distribution of muscle fiber minimal Feret's diameter and (**D**) average minimal Feret's diameter and (**E**) average cross-sectional area of TA muscle fibers in animals treated as in Fig. 4. 3A. In Fig. 4. 3B-E, n=5 and *P ⩽ 0.05, **P ⩽ 0.01, ***P ⩽ 0.001, ****P ⩽ 0.0001; by one-way ANOVA test. (**F**) Representative images of FACS contour plot of α7 integrin$^+$CD34$^+$Sca-1$^-$CD45$^-$CD31$^-$CD11b$^-$ cells, which correspond to MuSCs isolated from WT and *mdx* mice treated with DMSO or myriocin. (**G**) FACS-based quantification of freshly isolated MuSCs from hindlimb muscles of *mdx* or BL10 mice treated as in Fig. 4. 3A (n=9-12). ***P ⩽ 0.001，****P ⩽ 0.0001; by one-way ANOVA test. (**H**) mRNA expression of stemness (*Pax7*), activation (*Myf5*, *Myod*), differentiation (*Myog*) and proliferation (*Ki67, CDK4*) markers in MuSCs from mice treated as above (n=4). *$P \leq 0.05$, **$P \leq 0.01$, ***$P \leq 0.001$; by multiple two-way t-test. (**I**) mRNA levels of enzymes involved in sphingolipid *de novo* synthesis, including *Sptlc1, Sptlc2, Cers1-6, Degs1* and *Kdsr*, in MuSCs from mice treated as in Fig. 4. 3A. (n=4) *P ⩽ 0.05; by multiple two-way t-test.

4.3.4 Myriocin improved the stem cell microenvironment in *mdx* muscles

During muscle regeneration, the activity of MuSCs is supported by specialized cell populations resident in the surrounding niche, such as fibroblasts, fibroadipogenic progenitors (FAPs) and immune cells (*242*). In DMD, loss of dystrophin leads to perturbed conditions of MuSC niche (*243*). Repetitive cycles of muscle degeneration and regeneration induce chronic accumulation of immune cells within dystrophic muscles, which in turn impairs muscle repair (*242*). The presence of chronic inflammation is a hallmark of DMD (*228*), and currently glucocorticoids are the only accepted anti-inflammatory therapy for DMD (*244*). Similar to glucocorticoids, myriocin also effectively reduced general inflammation in hindlimb muscles of *mdx* mice, evidenced by the decreased number of CD45$^+$ immune cells (Fig. 4. 4A, B). As key components of innate immunity, macrophages (MΦ) constitute the predominant inflammatory cell type within DMD patients (*245*). We observed that *mdx* mice display elevated levels of infiltrating macrophages (Fig. 4. 4C) and myriocin treatment reduced the absolute count of macrophages in dystrophic animals (Fig. 4. 4C), suggesting that myriocin has anti-inflammatory effects.

MΦs are capable of shifting to either proinflammatory M1 or anti-inflammatory M2 cells (*246*), and MΦ polarization plays a critical role in the procedure of muscle regeneration (*67, 247*). Pioneering work has demonstrated that, in comparison to WT mice, MΦs in *mdx* mice are characterized with a shift toward the M1 phenotype (*67*). To determine if myriocin could influence the polarization of MΦs, FACS was employed to distinguish between M1 MΦs, expressing CD11c, and M2 MΦs, expressing CD206. Our results confirmed the documented imbalance of intramuscular MΦ polarization in *mdx* mice (Fig. 4. 4D, E), and myriocin reversed this profile (Fig. 4. 4D, E). In addition, the mean fluorescence intensity (MFI) of CD11c expression in macrophages from myriocin treated *mdx* mice was significantly lower than DMSO treated ones, whereas CD206 MFI was relatively higher as compared with *mdx* controls (Fig. 4. 4F). To further investigate the alterations of macrophage polarization, we evaluated mRNA expression of typical M1 and M2 surface markers in TA muscle of *mdx* mice in the different groups. The basal level of most M1 and M2 surface markers was significantly increased above WT values in the *mdx* group (Fig. 4. 4G). Myriocin treatment attenuated most of these proinflammatory M1 markers (e.g. *Il6*, *iNos*, *Cd11*), while at the same time boosting the expression of anti-inflammatory M2 markers (e.g. *Il10*, *Cd206*) (Fig. 4. 4G). Thus, reduction of sphingolipid synthesis could switch the balance of macrophage polarization towards anti-inflammatory M2 phenotype.

In addition to the anti-inflammatory effects, myriocin treatment also reduced the number of FAPs, which are reported to cause fibrosis and fat infiltrations in dystrophic animals (Fig. 4.4H). In line with decreased accumulation of FAPs in myriocin-treated *mdx* mice, the fibrotic area of TA muscles was also reduced in response to myriocin treatment (Fig. 4. 4I). Taken together, our findings suggest that myriocin could not only improve the functional capacity of MuSC to maintain an adequate MuSC pool and regenerative capacity, but also was able to restore the homeostasis of the MuSC microenvironment in dystrophic muscles.

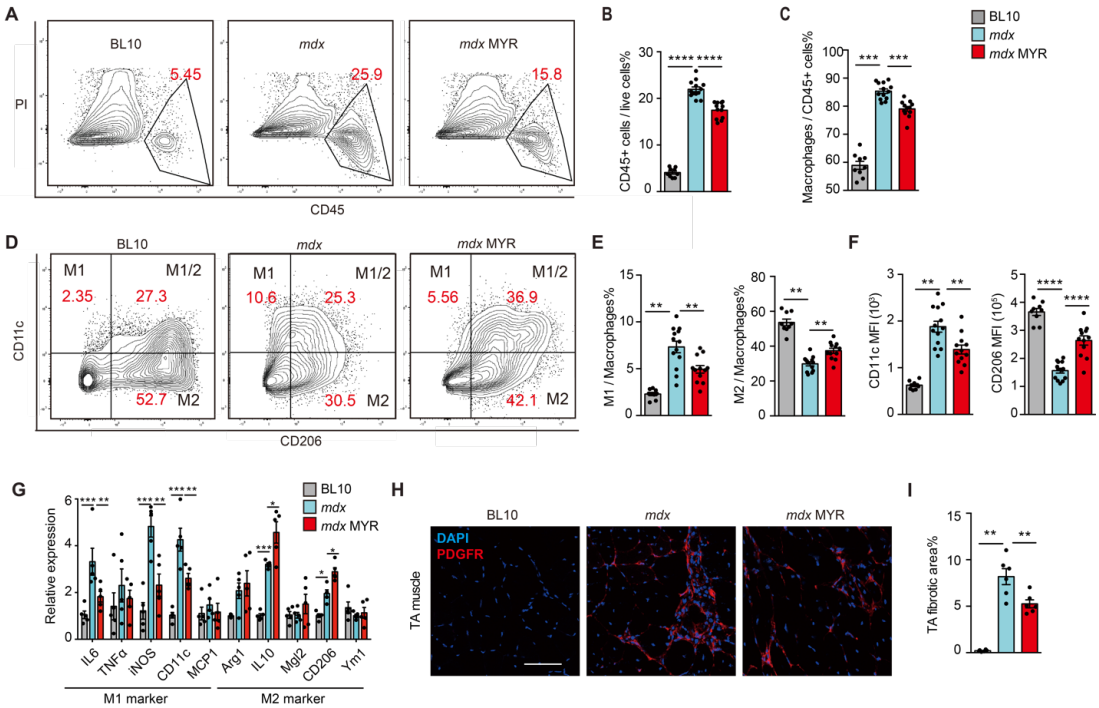

Fig. 4. 4. Myriocin exhibited anti-inflammatory effects and restored the macrophage polarization in dystrophic muscles. (**A**) Representative images of FACS contour plot of $CD45^{+}PI^{+}$ live cells and (**B**) corresponding quantification of $CD45^{+}$ cells normalized to the number of total PI^{+} live cells. ****P ≤ 0.0001; by one-way ANOVA. (**C**) FACS-based quantification of $CD11b^{+}F4/80^{+}$ macrophages, normalized to the number of total immune cells. (n=9-12) ***$P \leq 0.001$; by one-way ANOVA. (**D**) Representative images of FACS contour plot of distinct macrophage subpopulations, and (**E**) corresponding quantification of M1 and M2 cells normalized to the number of entire macrophages (n=9-12). **P ≤ 0.01 by one-way ANOVA test. (**F**) Mean fluorescent intensity of CD206 and CD11c in macrophages from WT and *mdx* mice. (n=9-12) **P ≤ 0.01, ****P ≤ 0.0001; by one-way ANOVA test. (**G**) mRNA expression of M1 markers (*IL6, TNFα, iNOS, CD11c and MCP1*) and M2 markers (*Arg1, IL10, Mgl2, CD206 and Ym1*) in TA muscles of WT and DMSO- or myriocin-treated *mdx* mice (n=5). *P ≤ 0.05, **P ≤ 0.01, ***P ≤ 0.001; by two-way ANOVA test. (**H**) Immunostaining of PDGFR that is the typical marker of FAPs, Laminin and DAPI in TA muscles of mice used in Fig. 4. 4E. Scale bar = 50 μm. (**I**) Quantification of fibrotic area in TA muscles (n=6).

4.3.5 Myriocin protected dystrophic mice from cardiac and diaphragm failure

Although DMD is characterized by progressive muscle wasting, cardiomyopathy and respiratory failure are the most important symptoms responsible for the increased mortality associated with DMD (*225*). As a commonly used animal model of DMD, *mdx* mice recapitulate some of the features observed in DMD induced cardiomyopathy (*248*). Histological evidence of interstitial cardiac fibrosis (Fig. 4. 5A, B) and cardiomyocyte necrosis (Fig. 4. 5C) was seen in *mdx* mice, which was effectively reduced by myriocin treatment (Fig. 4. 5A-C). Moreover, compared to *mdx* mice treated with vehicle, myriocin-treated mice demonstrated milder cardiac hypertrophy, as evidenced by a decrease in heart weight (Fig. 4. 5D).

In contrast to *mdx* hearts, which in general do not exhibit as severe dysfunction as that seen in DMD patients, the *mdx* diaphragm faithfully recapitulates a pattern of degeneration, fibrosis and severe functional deficits comparable to that of the diaphragm in human DMD (*249*). Myriocin treatment significantly reduced the deposition of FAPs (Fig. 4. 5E) and hence the fibrosis was significantly attenuated in *mdx* diaphragm (Fig. 4. 5F, G). In parallel, markers of inflammation and necrotic lesions were reduced in the diaphragm of myriocin-treated *mdx* mice (Fig. 4. 5H). Our results hence provide evidence that myriocin is capable of reverting the histological appearance of *mdx* heart and diaphragm. As cardiac and respiratory failures are the leading causes of death in DMD, our findings could have beneficial implications for overall mortality of DMD patients.

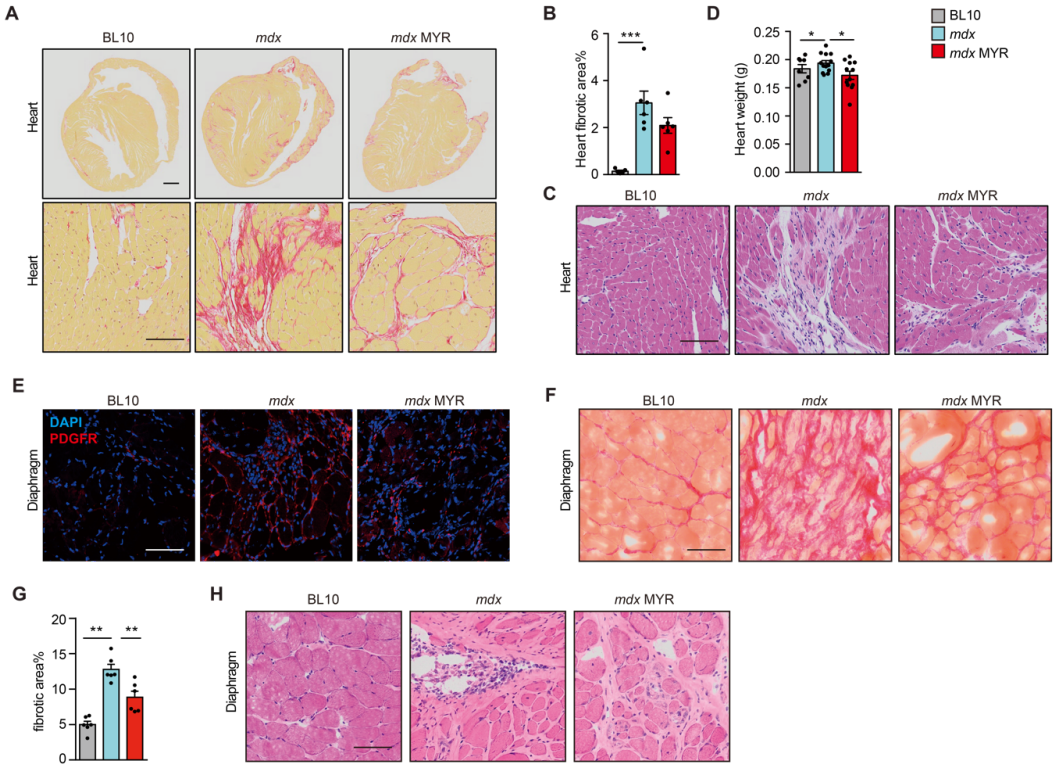

Fig. 4. 5. Myriocin ameliorated heart failure and respiratory dysfunctions in *mdx* mice. (**A**) Picrosirius red staining of hearts from control and *mdx* male mice with and without myriocin treatment. Representative images of the whole hearts and magnified sections showing fibrosis. Scale bar =100 μm. (**B**) Quantification of fibrotic area in hearts using the heart images of picrosirius red staining (n=6). ***P ⩽ 0.001; by one-way ANOVA test. (**C**) Representative images of hematoxylin and eosin (H&E) staining of heart sections from control and *mdx* male mice with and without myriocin treatment, showing heart necrosis and inflammation. Scale bar =100 μm. (**D**) Heart mass of C57BL/10SnJ and DMSO- or myriocin-treated *mdx* mice (n=7-12). *P ⩽ 0.05; by one-way ANOVA test. (**E**) Immunostaining of PDGFR, Laminin and DAPI in diaphragms of mice as in Fig. 4. 5A. Scale bar = 50 μm. (**F**) Representative images of picrosirius red staining of sections of the diaphragm from mice treated as in Fig. 4. 5A, showing fibrosis. Scale bar = 50μm. (**G**) Quantification of the fibrotic area based on the picrosirius red staining images of diaphragm as shown in Fig. 4. 5F (n=6). **P ⩽ 0.01; by one-way ANOVA test. (**H**) Representative images of H&E staining of the diaphragm sections, showing necrosis and degeneration, of mice treated as in Fig. 4. 5E. Scale bar = 50 μm.

4.4 Discussion

In the present study, we for the first time provide evidence that the aberrant sphingolipid metabolism in skeletal muscle is associated with DMD. The increased transcript and protein abundance of enzymes of the sphingolipid biosynthetic pathway in skeletal muscle of human DMD patients and *mdx* mice suggest that there could also be increased *de novo* synthesis of sphingolipid metabolites, such as ceramides. To verify if the abnormal expression of transcripts involved in sphingolipid synthesis translates into the alterations in central sphingolipid metabolites and the efficacy of myriocin on the inhibition of sphingolipid biosynthesis, measurement of diverse sphingolipids including different species of ceramides will be warranted. Accumulation of sphingolipids is associated with various diseases (*110*) and inhibition of sphingolipid synthesis has previously been shown to counteract metabolic dysfunction in the muscle (*191*), and to counteract age-associated sarcopenia (chapter 3), while the link between sphingolipids and muscular dystrophies has remained unproven. Inspired by these previous results, we hypothesized that blocking sphingolipid synthesis could be an effective strategy to treat DMD, and we used myriocin, a specific inhibitor of serine palmitoyltransferase (SPT), to evaluate our hypothesis in the *mdx* mouse and human DMD cell models.

In response to myriocin treatment, we observed improved membrane integrity in *mdx* mice, as evidenced by reduced permeability to Evans Blue and lower serum CK level and the

regeneration of dystrophic muscles is restored, leading to reduced centronucleated fibers and increased muscle fiber size. Moreover, myriocin activated the Ca^{2+} transport machinery, restoring the impaired Ca^{2+} homeostasis characteristic of dystrophic muscles. In line with improvements in cellular homeostasis, myriocin treatment also enhanced muscle strength, endurance, and coordination of *mdx* mice. Importantly, DMD-associated cardiac and respiratory failures were partially reversed by myriocin treatment, providing further support for the therapeutic potential of sphingolipid reduction in DMD.

Since repetitive cycles of regeneration and degeneration result in the exhaustion of MuSCs, restoring MuSC pool has the potential to improve the clinical course of DMD (*168*). We demonstrated that myriocin treatment replenished the reservoir of MuSC in *mdx* mice by protecting dystrophic MuSCs against premature differentiation and impaired proliferation, thus facilitating muscle regeneration in *mdx* mice. The role of the sphingolipid signaling cascade in the coordination of MuSC function has not been fully elucidated. Whereas, sphingosine-1-phosphate (S1P) was shown to induce the proliferation of MuSCs (*250*), ceramides have been associated with cell growth arrest (*251*). Since relative levels of these interconvertible metabolites can determine cell fate (*252*), it is possible that ceramide and S1P exert opposite effects on mediating MuSC proliferation. Given that *mdx* derived MuSCs display higher transcript levels of sphingolipid biosynthetic enzymes, the ensuing increased generation of ceramides in MuSCs may lead to the premature differentiation of the dystrophic MuSCs.

Apart from intrinsic mechanisms, the activity of MuSCs is also regulated by extrinsic signals. The role of MuSC niche is crucial for MuSC function, as demonstrated by similar regenerative capacities of MuSCs removed from dystrophic milieu and MuSCs derived from healthy muscles (*253, 254*). In the present study, we demonstrated that myriocin treatment modifies the microenvironment surrounding MuSCs by reducing skeletal muscle inflammation and fibrosis, and inducing a shift in macrophage polarization in the dystrophic muscles towards anti-inflammatory M2 macrophages. An imbalance of M1 and M2 macrophages, primarily linked to chronic inflammation, has been shown to stimulate the accumulation of pro-fibrotic factors and to impair MuSC activation (*255*). High levels of M1 macrophages are directly associated with defective MuSC activation and proliferation (*256, 257*), partially contributing to the exhaustion of MuSCs in *mdx* mice. In contrast, the M2 population, emerging later at the phase of receding inflammation, promotes muscle growth and regeneration, and reduces M1-dependent cytolysis of muscle cells (*258, 259*). Even though multiple studies have explored ways to shift macrophage populations towards the M2 phenotype (*260-262*), glucocorticoids remain the only pharmacological agent that has consistently demonstrated efficacy on the preservation of muscle force and ambulatory function in DMD patients (*263*). Despite the therapeutic benefits, glucocorticoids are nonspecific and have many detrimental side effects. In our preclinical study, reduction of muscle sphingolipid levels by myriocin in dystrophic animals recapitulated many effects of glucocorticoids, in particular macrophage polarization, without any notable adverse effects. Although ceramides are known to be implicated in the activation of proinflammatory pathways (*264*) and ceramide depletion has been shown to reduce the inflammatory response (*265*), the exact mechanism by which sphingolipids modulate macrophage polarization remains to be elucidated. Our results demonstrate that inhibition of sphingolipid biosynthesis can reduce the proinflammatory and boost the anti-inflammatory effects of macrophages, potentially providing a more favorable microenvironment for optimal function of muscle fibers.

Collectively, our findings provide evidence that inhibition of sphingolipid *de novo* synthesis could be an attractive treatment strategy for DMD and potentially also for other muscular dystrophies. In our study, inhibition of sphingolipid *de novo* synthesis pathway by myriocin resulted in improvements in muscle strength, endurance, and coordination, and reductions in fibrosis and inflammation by shifting macrophage polarization towards the anti-inflammatory M2 phenotype. Targeting many pathophysiological pathways by a single agent offers many advantages, such as higher efficacy, fewer side-effects, and reduction of polypharmacy. The multi-faceted benefits achieved by correcting aberrant sphingolipid metabolism could delay the

onset of symptoms, slow the progression of disease, and ultimately counteract the loss of independence and excessive mortality associated with muscular dystrophies.

4.5 Materials and methods

Animal. C57BL/10ScSn or C57BL/10ScSn-Dmd^{mdx}J mice were purchased from Janvier. Myriocin (Enzo Life Sciences, Farmingdale, NY) was first dissolved in DMSO and then was mixed with PBS. Mice were treated with myriocin from 3-weeks old for five months, during which the mice were injected with myriocin at a dose of 0.4mg/Kg or corresponding volume of DMSO three times per week. All mice were housed in micro-isolator cages in a room illuminated from 7:00am-7:00pm with *ad libitum* access to normal chow diet and water. All the animal experiments are authorized by the local animal experimentation committee of the Canton de Vaud under license 2890.1.

Grip strength test. Muscle strength was evaluated by a grip strength test after 5 weeks of myriocin treatment. The grasp strength of each mouse for four limbs was measured on a pulldown grid assembly connected to the grip strength meter (Columbus Instruments). Individual mouse was drawn along a straight line parallel to the grid until the grip was broken, providing the peak force in grams. This was repeated 3 times with 5 min intervals between each measurement.

Endurance running. The exercise capacity of each mouse was assessed after 11 weeks of myriocin treatment by monitoring the running distance on the uphill treadmill. The exercise regimen commenced at a speed of 9cm/s with an inclination of 5 degrees. The speed was gradually increased 3 cm/s every 12 min. Mice were considered to be exhausted and removed from the treadmill, following the accumulation of 7 or more shocks (0.1mA) per min for two consecutive minutes. The distance traveled and time before exhaustion were registered as maximal running distance and period. Mice were familiarized with the treadmill one day before recording the running activity.

Eccentric running and creatine kinase measurement. Downhill running was performed 15 weeks after treatment. Mice began the exercise at a speed of 15 cm/s with a declination of 5°. The speed gradually increased after each period of 12 minutes of racing by 3cm/s. The duration of each step of this protocol was 1 min. The distance traveled and the number of shocks received over 1 min intervals were recorded. All mice were set to run for 90 min except if a mouse got 7 shocks (0.1mA) during two consecutive steps, which was considered exhausted and withdrawn from the running. Mice were familiarized with the treadmill one day before recording the running activity. Blood was collected before and immediately after the eccentric running. Creatine kinase was measured on plasma collected before and after eccentric running using the Creatine Kinase Flex Reagent Cartridge (Siemens Healthcare Diagnostics AG) on the Dimension Xpand Plus Instrument (Siemens Healthcare Diagnostics AG).

Rotarod test. The rotarod test was performed after the mice were treated with myriocin for XX weeks to measure muscle strength, coordination, and endurance. Mice were left undisturbed in the room for 30 min. The speed of the rotating cylinder (rotarod) increased from 0 to 40 rpm in 5 min. Each mouse experienced 3 trials per day for 3 consecutive days. The latency and speed the mouse reached at passive rotation or fall from the rotor was recorded, and the latency and speed of the best trial of the second day is presented.

Muscle stem cell isolation. This protocol is adapted from the published literature (*266*). Both hindlimbs including gastrocnemius, soleus, and quadriceps muscles were dissected and transferred into PBS on ice. All muscles were trimmed, minced and digested with 2.5U/ml of Dispase II (Roche) and 0.2% Collagenase B (Roche) in PBS for 30 mins at 37 °C. Tissues were then centrifuged at 50*g* for 5 min followed by the removal of the supernatant and further digestion for 20 mins at 37 °C twice. Muscle slurries were sequentially filtered through 100 µm, 70 µm and 40 µm cell strainers. The isolated cells were then washed in washing buffer (HBSS + 2.5% BSA) and resuspended in 800 µL of washing buffer. They were immediately stained with antibodies, including CD31 (1:800, eBioscience, eFluor450 conjugated); CD45 (1:200, eBioscience, eFluor450 conjugated); Sca-1 (1:1000, eBioscience, PE-Cy7 conjugated); CD11b (1:100, eBioscience, eFluor450) and CD34 (1:100, BD Pharmingen, FITC conjugated); alpha-7 integrin (1:50, RD system, eFluor700 conjugated) for 60 min at 4°C. Secondary

staining was performed with propidium iodide (PI, Sigma) for 15 min at 4°C in the dark. Stained cells were analyzed and sorted using the FACSAria II instrument (BD Biosciences). Debris and dead cells were excluded by forward scatter, side scatter and PI gating.

Flexor digitorum brevis (FDB) muscle fibre dissociation. The flexor digitorum brevis (FDB) muscles were incubated for 38 min at 37°C in an oxygenated 'Krebs-Hepes' solution (in mM: NaCl 135.5, MgCl2 1.2, KCl 5.9, glucose 11.5, Hepes 11.5, CaCl2 1.8 (pH 7.3) containing 0.2% collagenase type IV (Sigma-Aldrich Corp., St Louis, MO, USA). Muscles were then washed twice in Dulbecco's modified Eagle's medium (DMEM)/HAM F12 (Sigma) supplemented with 2% fetal bovine serum (Sigma) and mechanically dissociated by repeated passages through fire-polished Pasteur pipettes of progressively decreasing diameter. Dissociated fibres were plated onto tissue culture dishes coated with Matrigel (BD Bioscience, San Jose, CA, USA) and allowed to adhere to the bottom of the dish for 2 h. For Ca^{2+} measurements, cells were plated on glass bottom MaTek disks. Culture dishes were kept in an incubator, with 5% CO_2 at 37°C for 2 hours to let the fibres to attach.

Ca^{2+} imaging using Fluo-4 AM in FDB muscle fibre. FDB fibres were loaded with the cytosolic Ca^{2+} indicator Fluo-4/AM (5μM, Invitrogen, Basel, Switzerland) solubilized in a Krebs solution (in mM: NaCl 135.5, MgCl2 1.2, KCl 5.9, glucose 11.5, Hepes 11.5, CaCl2 1.8 (pH 7.3) for 20 min in the incubator. The cells were then rinsed twice with a free-Ca^{2+} Krebs solution (in mM: NaCl 135.5, MgCl2 1.2, KCl 5.9, glucose 11.5, Hepes 11.5, 200 μM Na-EGTA, (pH 7.3)). Fluo-4 fluorescence was monitored using a confocal microscope system (Zeiss LSM 5 Live, 40x oil immersion lens, excitation wavelength was 488 nm and the emitted fluorescence was recorded between 495-525 nm). After recording the basal fluorescence, the fibres were stimulated with 2.5 mM (final concentration) caffeine to trigger Ca^{2+} release from the sarcoplasmic reticulum (SR). Zen software (products/microscopy-software/zenlite/zen-2-lite) was used for the acquisition and data were extracted to excel files for analysis using a 300s time lapse acquisition framework. The use of the single excitation/emission dye fluo-4 necessitates normalizing to pre-stimulation values to account for possible differences in dye loading and excitation strength. The amplitude of Ca^{2+} transients was calculated by subtracting the peak fluorescence from the baseline. The mean fluorescence from 150 to 250s of the time lapse acquisition was calculated as a plateau of the Ca^{2+} curve.

Macrophage isolation. Gastrocnemius, soleus, and quadriceps muscles from both hindlimbs were excised and transferred into PBS on ice. All muscles were trimmed, minced and digested with 2.5U/ml of Dispase II (Roche) and 0.2% Collagenase B (Roche) in PBS for 30 mins at 37 °C. Tissues were then centrifuged at 50*g* for 5 min followed by the removal of the supernatant and further digestion for 20 mins at 37 °C twice. Muscle slurries were sequentially filtered through 100 μm, 70 μm and 40 μm cell strainers. The isolated cells were then washed in washing buffer (HBSS + 2.5% BSA) and resuspended in 800 μL of washing buffer. They were immediately stained with antibodies, including CD45 (1:200, eBioscience, eFluor450 conjugated); F4/80 (1:200, Biolegend, FITC conjugated); CD11b (1:200, eBioscience, PE-Cyanine7) and CD11c (1:200, BD Pharmingen, APCeF780 conjugated); CD206 (1:200, Biolegend, eFluor647 conjugated) for 60 min at 4°C. Secondary staining was performed with propidium iodide (PI, Sigma) for 15 min at 4°C in the dark. Stained cells were analyzed using the LSR Fortessa instrument (BD Biosciences). Debris and dead cells were excluded by forward scatter, side scatter and PI gating.

Histology. Histological specimens were prepared and analyzed as described (*105*). Muscle integrity was assessed with 1% solution of Evans blue dye (EBD), which was injected into the peritoneal cavity, using 1% volume to body weight, 24 hours before sacrifice. EBD was dissolved in phosphate-buffered saline (PBS) [0.15 M NaCl, 10 mM phosphate buffer (pH 7.4)] and sterilized by passage through membrane filters with a 0.2 μm pore size. Upon sacrifice, the hind leg skin of the mice was removed, and the animals were photographed for dye uptake into skeletal muscles, indicated by blue coloration. Muscle sections from EBD-injected or non-injected animals were then incubated in 4% PFA at -20°C for 15 min, washed three times for 10 min with PBS, counterstained with DAPI laminin (1:200, Sigma), PDGFR (1:200, Cell Signaling) and mounted with Dako Mounting Medium. Microscopy images of red emission

fluorescence from EBD-positive muscle fibers were analyzed using the ImageJ software. Centralized nuclei percent, minimal Feret diameter and cross-sectional area in TA muscles were determined using the ImageJ software quantification of laminin and DAPI-stained muscle images from VS120-S6-W slides scanner (Olympus). A minimum of 2000 fibers were used for each condition and measurement. The minimal Feret diameter is defined as the minimum distance between two parallel tangents at opposing borders of the muscle fiber. This measure has been found to be resistant to deviations away from the optimal cross-sectioning profile during the sectioning process.

Human cells. Primary human myoblast cells derived from three male healthy individuals and three male DMD patients were provided by Hospices Civils de Lyon. The three DMD patients and healthy individuals were all from 4- to 7-year-old-males. Cells were cultured in F-10 medium supplemented with 12% FBS and penicillin/streptomycin.

Extraction of mRNA for quantitative real-time PCR. Total RNA was extracted from MuSCs by sorting cells directly into TriPure RNA isolation reagent (Roche) or from cultured primary human myoblasts or mouse muscle tissue using TriPure reagent according to the product manual. Total RNA was transcribed to cDNA using QuantiTect Reverse Transcription Kit (Qiagen). Expression of selected genes was analyzed using the LightCycler480 system (Roche) and LightCycler® 480 SYBR Green I Master reagent (Roche).

Western Blotting. DMD patient myoblast cells or mouse skeletal muscle tissues were lysed on ice in RIPA buffer composed of Tris HCl 50 mM, NaCl 5 M, EDTA 5 mM, SFS 0.1%, NAF 100 mM, sodium deoxycholate 5 mg/mL, and NP40 1% containing protease and phosphatase inhibitors (Roche). Protein concentrations were determined using Bradford method, and samples were loaded on a 12% SDS-PAGE gel. After electrophoresis, proteins were separated by SDS-PAGE and transferred onto methanol activated polyvinylidene difluoride membranes. Blocking of the membranes was done in 5% milk-TBST for 1 h, and after wash, the membranes were incubated overnight with primary antibody anti-SPTLC1 (Proteintech) or anti-SPTLC2 (Thermoscientific) or anti-CERS2 (Sigma) in 3% BSA-TBST 1:1000. Incubation with secondary anti-rabbit polyclonal antibody was done in 5% BSA-TBST 1:2000. Antibody detection reactions were developed by enhanced chemiluminescence (Advansta), and imaged using the c300 imaging system (Azure Biosystems).

Bioinformatics analysis. Heatmaps were obtained using the heatmap2 function of R/gplots.

Statistics. Differences between two groups were assessed using two-tailed *t*-test. Differences between more than two groups were assessed using one-way analysis of variance (ANOVA). To compare the interaction between two factors, two-way ANOVA tests were performed. GraphPad Prism 6 was used for all statistical analyses. All P values <0.05 were considered significant. *$P \leq 0.05$, **$P \leq 0.01$, and ***$P \leq 0.001$, ****$P \leq 0.0001$.

Chapter 5. Conclusions, discussion and future perspectives

5.1 Results achieved

Skeletal muscle is a major participant in different metabolic signaling pathways. Its damage leads to metabolic disruptions. Muscular dystrophies, due to the absence of structure proteins, usually show metabolic and endocrine disturbances. In my thesis, we established links between energy metabolism and muscle and MuSC functions, utilizing diverse pharmacological approaches to modulate mitochondrial activity and sphingolipid metabolism to treat muscular dystrophies.

In the 1st project, we provided first-hand evidence that defective mitophagy acts as a biomarker of muscular dystrophy. In DMD patients and in the *mdx* mouse model, a significant downregulation of all major players of the mitophagy pathway was observed at transcript level. Restoring mitophagy with dietary UA supplementation improved muscle function in *mdx* mice, an effect reproduced both in a *C. elegans* model of DMD and in primary myoblast cells derived from DMD patients. Together with improved muscle functions, UA also rescued dysfunctional MuSCs in *mdx* mice, alleviating DMD-related phenotypes.

In the following two projects, we identified a novel role for sphingolipids in proliferation and differentiation of muscle progenitor cells. Spingolipids are a class of bioactive lipid molecules whose diverse functions in cellular physiology are emerging. We demonstrated sphingolipids accumulated in skeletal muscle upon aging and muscular dystrophies, and that inhibition of sphingolipid biosynthesis by myriocin, an inhibitor of serine palmitoyltransferase, the first and rate-limiting enzyme of the sphingolipid *de novo* synthesis pathway, reduced sphingolipid accumulation and symptoms of age-related sarcopenia and muscular dystrophies. Interestingly, in aged mice, we found that depletion of sphingolipids also improved the regenerative ability of MuSCs by boosting both MuSC proliferation and myogenic differentiation. In dystrophic animals, MuSCs also have defective sphingolipid metabolism, typified by the upregulation of enzymes involved in sphingolipid *de novo* synthesis. Myriocin rescued the dystrophic phenotype of *mdx* MuSCs through modulating both intrinsic mechanisms and surrounding microenvironment of MuSCs. Importantly, in the 3rd project, we established the link between sphingolipid metabolism and macrophage polarization, demonstrating that inhibition of sphingolipid synthesis could effectively reconstitute the balance of M1 and M2 macrophages thus counteract the compromised tissue integrity of dystrophic muscles.

Our studies therefore not only answer basic biological questions, such as the fundamentals concerning ageing and the pathogenesis of muscular dystrophies, as well as the molecular mechanisms engaged in the regulation of MuSC self-renewal and differentiation; but also provide evidence for novel treatments for human muscle diseases and healthy ageing by restoring mitochondrial stress response or interfering with sphingolipid generation during ageing and disease.

5.2 Mitochondrial stress responses, MuSCs and muscular diseases

Healthy mitochondria are essential for functional metabolic systems in skeletal muscles of mammals. The quality of mitochondria is controlled by mitochondrial stress pathways that include mitophagy and the mitochondrial unfolded protein response (UPR^{mt}). Compromised mitochondrial stress responses are associated with age- or disease-related dysfunctions in mitochondria. Therefore, restoration of mitochondrial stress pathways could lead to the

extension of lifespan or amelioration of diseases (*267*). Our studies have shown that dystrophic muscles and MuSCs have defective mitophagy, which could be rescued by UA. MuSC is the engine of muscle regeneration, and DMD is characterized by repetitive cycles of regeneration and degeneration leading to exhaustion of MuSCs (*268*). Hence, DMD also appears to be a MuSC disease (*168*). Accordingly, the question is, how much MuSCs contribute to the restoration of dystrophic phenotypes produced by UA and how mitochondrial stress responses control MuSC functions?

To investigate the contribution of MuSCs to UA-dependent restoration of DMD, future analysis will be required. For example, *mdx* mice that are deficient of PINK1 or PARKIN specifically in MuSCs can be generated. These mice can be treated with UA, to verify if UA could still improve the functions of dystrophic muscles, revealing whether UA-dependent benefits observed in *mdx* mice are attributed to MuSCs. Additionally, *mdx* mice that overexpress mitophagy-related genes specifically in MuSCs would constitute another useful model, allowing us to investigate the role of stem cell mitophagy in the progression of muscular dystrophy. Moreover, to rule out the effects of UA on MuSC niche, proper design of experiments, such as serial transplantation, is also needed.

To explore how mitochondrial stress response regulates MuSC function, such as self-renewal and differentiation, CRISPR/Cas9 could be employed to knock out specific mitophagy-related genes in primary MuSCs. Some *in vivo* work can also be performed to examine the effects of mitophagy-deficient MuSCs on muscle regeneration.

Apart from mitophagy, previous research from our lab provided evidence that deficient UPR^{mt} leads to MuSC senescence that has been seen in aged mice (*105*). The senescence of MuSCs has also been reported in young *mdx* mice throughout the age of 4-23 weeks (*268, 269*). Taken together, we assume that dystrophic muscles and MuSCs might also have defective UPR^{mt} or even other mitochondrial stress pathways. To broaden our exploration and develop more efficient treatment, we will validate first if other mitochondrial stress pathways are also deficient in the context of muscular dystrophy through analyzing available human datasets, and it might be worth treating diseased animals with compounds that are well-established activators of mitochondrial stress responses, verifying their therapeutic effects.

5.3 Complexity of sphingolipid metabolism

Inhibition of sphingolipid synthesis by myriocin has produced beneficial effects for metabolic diseases, especially in the context of insulin resistance and atherosclerosis (*129, 191*). Our studies establish a novel role for sphingolipids in muscle differentiation, sarcopenia, and dystrophy. We demonstrate that sphingolipids accumulate in skeletal muscle in these conditions, and that inhibition of sphingolipid synthesis improves muscle function in sarcopenia and dystrophies. In our project, we primarily employed myriocin to demonstrate these concepts to produce therapeutic benefits in both ageing and *mdx* mice. With these data, we hypothesized that inhibition of other enzymes of the pathway, such as DEGS, CERS1-6 and KDSR, could result in similar benefits.

Interestingly, in contrast to the upregulation of other enzymes involved in sphingolipid synthesis, *CERS1* shows decreased transcript level in diseased or ageing skeletal muscles and is negatively correlated with other enzymes of sphingolipid biosynthesis pathway (chapter 3 and 4). CERS1 is expressed mainly in brain and at low levels in skeletal muscles and testis, and genetic ablation of CERS1 causes neurodegeneration and cerebellar atrophy (*270*). On the other hand, skeletal muscle specific deletion of *Cers1* improves glucose homeostasis in mice (*234*). These contradictory data motivated us to explore in future the role of CERS1 in promoting the development of muscle diseases, and suggested that individual enzyme might play distinct roles in the pathogenesis of different diseases.

Sphingolipid desaturase DEGS1 converts dihydroceramides to ceramides. Inactivation of *DEGS1* leads to reduced ceramide, but increased dihydroceramide, levels (*271*), and imbalance of ceramides and dihydroceramides has been implicated in the pathogenesis of diverse diseases, such as leukodystrophies (*272*). Currently, no data exists on the effects of muscle specific inhibition of DEGS1. Hence, we will measure the levels of dihydroceramides in both aged and *mdx* mice, further investigating the connection between dihydroceramide/ceramide ratio and muscle diseases. Moreover, we also plan to study the activity of individual sphingolipids, such as C18 or C24 ceramides, which are generated by different ceramide synthases and have different bioactive functions. Due to the intricacy of sphingolipid metabolism, more research is required to find out the exact roles of individual metabolites and enzymes in aging and disease.

5.4 Potential of clinical translation

Our work highlights the significant potential of mitochondrial stress response activation and sphingolipid synthesis inhibition to prevent the progression of muscular dystrophy and age-related sarcopenia. In the *mdx* mice, recovery of mitophagy by UA not only improves MuSC function, but also reduces general inflammation and fibrosis in muscle (chapter 2) and in aged rats, by activating mitophagy, administration of UA improves their exercise capacity (*103*). In addition to manipulating mitochondrial stress pathways, we also associated lipid metabolism with human ageing and muscular diseases, and presented that sphingolipids accumulate during ageing and muscle diseases. It is therefore reasonable to expect that depletion of sphingolipids in skeletal muscle might delay ageing and alleviate muscle diseases. Indeed, in aged mice, myriocin treatment enhanced MuSC proliferation and differentiation (chapter 3), leading to the amelioration of ageing-related symptoms; while in the *mdx* mice, myriocin repolarized macrophages to improve muscle regeneration, which finally reduced dystrophic phenotypes (chapter 4). Overall, UA and myriocin benefit muscular diseases and ageing through effects on both MuSCs and myofibers; besides, myriocin exhibits the potential in maintaining the balance of macrophage populations. Hence, both mitophagy-activators, such as UA, and inhibitors of sphingolipid generation, could be interventions that profit human muscular dystrophy and potentially other neuromuscular diseases as well as healthy ageing.

With all these promising data, one question naturally arose in our mind: how far are we from translating these results to the clinic?

Toxicity tests in humans are indispensable before starting a large-scale clinical trial to test the appropriateness of our compounds to age-related sarcopenia or muscle dystrophies in humans. Preliminary trials to study the safety of UA have been initiated in humans by both academic and industrial research teams. For instance, recently, the company Amazentis collaborated with our lab to announce the results of first-in-human clinical trial, revealing that oral administration of UA with daily doses of either 500mg or 1000mg both induced improved mitochondrial function and cellular health in elderly human volunteers (*104*). This study demonstrates the successful translation of benefits of mitophagy activator UA seen in rodents to humans, in particular the combination of its positive biological effects on mitochondrial health, safety and bioavailability profile.

Since the safety of UA has been confirmed with Phase I clinical trials, the validation of preventive or curative benefits of UA needs to be started. According to our data and published literature, UA might have therapeutic effects on a wide variety of diseases, including muscular dystrophy, ageing-related sarcopenia, Alzheimer's disease, osteoarthritis, prostate cancer, colon cancer and pancreatic cancer due to the involvement of defective mitophagy in these diseases (*154, 273-277*), most of which have been validated on animal models. Despite the verification of the benefits of UA on different diseases, more animal and clinical work is still required to verify whether UA and other mitophagy boosters or even activators of different mitochondrial stress responses, could also show benefits on other muscle diseases and age-associated disorders, such as cardiovascular diseases.

Sphingolipid metabolism is implicated in the pathogenesis of numerous diseases, such as neurodegenerative diseases, metabolic disorders, various cancers, immune dysfunctions, cardiovascular disorders and diseases associated with skin integrity(*108*). Despite the broad involvement of sphingolipid metabolism in the progression of diverse diseases, the development of sphingolipid-related drugs and their applications to diseases are still in its infancy. The majority of sphingolipid-related drug candidates that advanced into clinical trials or are already clinically approved (Fingolimod, the first FDA-approved oral drug that interferes with sphingolipid metabolism) are targeting cancer or used for the treatment of multiple sclerosis (*278, 279*). Accordingly, more effort is required for animal and clinical work in novel drug discovery and for widening the applications of available drugs.

Myriocin, a potent antibiotic, is an analogue of sphingosine and a selective inhibitor of serine palmitoyltranferase (SPT). Recently, beyond myriocin, some companies have developed already alternative SPT inhibitors, such as imidazopyridine and pyrazolypiperidine (*280*). Together with our work that demonstrated the benefits of myriocin in treating muscular dystrophy and ageing-associated disorders, many groups also reported the therapeutic effects of myriocin and novel SPT inhibitors on other diseases, for instance, in diabetes and cancer (*128, 129, 281, 282*). In spite of many benefits that SPT inhibitors have shown, we cannot ignore the toxicity of SPT inhibitors, for example, myriocin inhibits normal cell growth at specific dosage (*283*). Furthermore, parenteral, not oral, administration of myriocin has been used in ours and other studies reporting health benefits of myriocin (*128, 132, 281*). Oral administration of imidazopyridine and pyrazolypiperidine was also noticed to cause a gastric enteropathy in rats (*280*). This is most likely due to the potential gastrointestinal side-effects of SPT inhibitors, although no formal study on this topic has been published. While our studies identify novel conditions and diseases for which SPT inhibition could be beneficial, they also point to the necessity of developing an SPT inhibitor suitable for oral administration.

Collectively, although our work has identified novel roles for sphingolipid metabolism in myogenic differentiation and macrophage polarization, and revealed the high clinical potential of modulators of mitochondrial stress responses and sphingolipid metabolism as novel therapeutics, more explorations, both in basic and translational researches, are necessary before these compounds are approved for wide and secure applications.

References

1. B. K. Pedersen, M. A. Febbraio, Muscles, exercise and obesity: skeletal muscle as a secretory organ. *Nature Reviews Endocrinology* **8**, 457 (2012).
2. W. R. Frontera, J. Ochala, Skeletal muscle: a brief review of structure and function. *Calcified tissue international* **96**, 183-195 (2015).
3. G. D. Thomas, Functional muscle ischemia in Duchenne and Becker muscular dystrophy. *Frontiers in physiology* **4**, 381 (2013).
4. B. J. Petrof, J. B. Shrager, H. H. Stedman, A. M. Kelly, H. L. Sweeney, Dystrophin protects the sarcolemma from stresses developed during muscle contraction. *Proceedings of the National Academy of Sciences* **90**, 3710-3714 (1993).
5. J. Ehmsen, E. Poon, K. Davies, The dystrophin-associated protein complex. *Journal of cell science* **115**, 2801-2803 (2002).
6. F. Rahimov, L. M. Kunkel, Cellular and molecular mechanisms underlying muscular dystrophy. *Journal of Cell Biology* **201**, 499-510 (2013).
7. F. Galbiati, B. Razani, M. P. Lisanti, Caveolae and caveolin-3 in muscular dystrophy. *Trends in molecular medicine* **7**, 435-441 (2001).
8. B. L. Patton, Laminins of the neuromuscular system. *Microscopy research and technique* **51**, 247-261 (2000).
9. K. M. Bushby, Making sense of the limb-girdle muscular dystrophies. *Brain* **122**, 1403-1420 (1999).
10. R. A. Williamson *et al.*, Dystroglycan is essential for early embryonic development: disruption of Reichert's membrane in Dag1-null mice. *Human molecular genetics* **6**, 831-841 (1997).
11. S. Guiraud *et al.*, The pathogenesis and therapy of muscular dystrophies. *Annual review of genomics and human genetics* **16**, 281-308 (2015).
12. A. Salmaninejad *et al.*, Duchenne muscular dystrophy: an updated review of common available therapies. *International Journal of Neuroscience* **128**, 854-864 (2018).
13. T. L. Van Westering, C. A. Betts, M. J. Wood, Current understanding of molecular pathology and treatment of cardiomyopathy in duchenne muscular dystrophy. *Molecules* **20**, 8823-8855 (2015).
14. D. G. Allen, N. P. Whitehead, Duchenne muscular dystrophy–what causes the increased membrane permeability in skeletal muscle? *The international journal of biochemistry & cell biology* **43**, 290-294 (2011).
15. A. KUMAR, N. KHANDELWAL, R. MALYA, M. B. REID, A. M. BORIEK, Loss of dystrophin causes aberrant mechanotransduction in skeletal muscle fibers. *The FASEB Journal* **18**, 102-113 (2004).
16. A. Kumar, A. M. Boriek, Mechanical stress activates the nuclear factor-kappaB pathway in skeletal muscle fibers: a possible role in Duchenne muscular dystrophy. *The FASEB Journal* **17**, 386-396 (2003).
17. A. Farini *et al.*, Inositol 1, 4, 5-trisphosphate (IP3)-dependent Ca2+ signaling mediates delayed myogenesis in Duchenne muscular dystrophy fetal muscle. *Development* **143**, 658-669 (2016).
18. M. Tabebordbar, E. T. Wang, A. J. Wagers, Skeletal muscle degenerative diseases and

strategies for therapeutic muscle repair. *Annual Review of Pathology: Mechanisms of Disease* **8**, 441-475 (2013).
19. C. Pastoret, A. Sebille, Mdx mice show progressive weakness and muscle deterioration with age. *Journal of the neurological sciences* **129**, 97-105 (1995).
20. J. W. McGreevy, C. H. Hakim, M. A. McIntosh, D. Duan, Animal models of Duchenne muscular dystrophy: from basic mechanisms to gene therapy. *Disease models & mechanisms* **8**, 195-213 (2015).
21. P. Sicinski *et al.*, The molecular basis of muscular dystrophy in the mdx mouse: a point mutation. *Science* **244**, 1578-1580 (1989).
22. J. S. Chamberlain, J. Metzger, M. Reyes, D. Townsend, J. A. Faulkner, Dystrophin-deficient mdx mice display a reduced life span and are susceptible to spontaneous rhabdomyosarcoma. *The FASEB Journal* **21**, 2195-2204 (2007).
23. C. Collins, J. Morgan, Duchenne's muscular dystrophy: animal models used to investigate pathogenesis and develop therapeutic strategies. *International journal of experimental pathology* **84**, 165-172 (2003).
24. B. Bostick *et al.*, Cardiac expression of a mini-dystrophin that normalizes skeletal muscle force only partially restores heart function in aged Mdx mice. *Molecular Therapy* **17**, 253-261 (2009).
25. I. N. Rybakova, J. R. Patel, K. E. Davies, P. D. Yurchenco, J. M. Ervasti, Utrophin binds laterally along actin filaments and can couple costameric actin with sarcolemma when overexpressed in dystrophin-deficient muscle. *Molecular biology of the cell* **13**, 1512-1521 (2002).
26. N. Deconinck *et al.*, Expression of truncated utrophin leads to major functional improvements in dystrophin-deficient muscles of mice. *Nature medicine* **3**, 1216 (1997).
27. A. Sacco *et al.*, Short telomeres and stem cell exhaustion model Duchenne muscular dystrophy in mdx/mTR mice. *Cell* **143**, 1059-1071 (2010).
28. H. Yin, F. Price, M. A. Rudnicki, Satellite cells and the muscle stem cell niche. *Physiological reviews* **93**, 23-67 (2013).
29. A. Mauro, Satellite cell of skeletal muscle fibers. *The Journal of biophysical and biochemical cytology* **9**, 493 (1961).
30. Y. X. Wang, M. A. Rudnicki, Satellite cells, the engines of muscle repair. *Nature reviews Molecular cell biology* **13**, 127 (2012).
31. M. H. Snow, Myogenic cell formation in regenerating rat skeletal muscle injured by mincing II. An autoradiographic study. *The Anatomical Record* **188**, 201-217 (1977).
32. A. S. Brack, I. M. Conboy, M. J. Conboy, J. Shen, T. A. Rando, A temporal switch from notch to Wnt signaling in muscle stem cells is necessary for normal adult myogenesis. *Cell stem cell* **2**, 50-59 (2008).
33. V. G. Punch, A. E. Jones, M. A. Rudnicki, Transcriptional networks that regulate muscle stem cell function. *Wiley Interdisciplinary Reviews: Systems Biology and Medicine* **1**, 128-140 (2009).
34. M. Buckingham, F. Relaix. (2007), vol. 23, pp. 645-673.
35. N. Chi, J. A. Epstein, Getting your Pax straight: Pax proteins in development and disease. *TRENDS in Genetics* **18**, 41-47 (2002).
36. S. Oustanina, G. Hause, T. Braun, Pax7 directs postnatal renewal and propagation of

myogenic satellite cells but not their specification. *The EMBO journal* **23**, 3430-3439 (2004).
37. M.-C. Sincennes, C. E. Brun, M. A. Rudnicki, Concise review: epigenetic regulation of myogenesis in health and disease. *Stem cells translational medicine* **5**, 282-290 (2016).
38. E. Bober, H.-H. Arnold, T. Franz, P. Gruss, P. Tremblay, Pax- 3 is required for the development of limb muscles: A possible role for the migration of dermomyotomal muscle progenitor cells. *Development* **120**, 603-612 (1994).
39. F. Relaix, D. Rocancourt, A. Mansouri, M. Buckingham, Divergent functions of murine Pax3 and Pax7 in limb muscle development. *Genes & development* **18**, 1088 (2004).
40. S. Kuang, S. B. Chargé, P. Seale, M. Huh, M. A. Rudnicki, Distinct roles for Pax7 and Pax3 in adult regenerative myogenesis. *The Journal of cell biology* **172**, 103-113 (2006).
41. A. P. Young, A. J. Wagers, Pax3 induces differentiation of juvenile skeletal muscle stem cells without transcriptional upregulation of canonical myogenic regulatory factors. *Journal of cell science* **123**, 2632-2639 (2010).
42. H. C. Olguin, B. B. Olwin, Pax-7 up-regulation inhibits myogenesis and cell cycle progression in satellite cells: a potential mechanism for self-renewal. *Developmental Biology* **275**, 375-388 (2004).
43. P. S. Zammit *et al.*, Muscle satellite cells adopt divergent fates: a mechanism for self-renewal? *The Journal of cell biology* **166**, 347 (2004).
44. M. Buckingham, F. Relaix, PAX3 and PAX7 as upstream regulators of myogenesis. *Seminars in Cell and Developmental Biology* **44**, 115 (2015).
45. D. D. W. Cornelison, B. J. Wold, Single- Cell Analysis of Regulatory Gene Expression in Quiescent and Activated Mouse Skeletal Muscle Satellite Cells. *Developmental Biology* **191**, 270-283 (1997).
46. R. L. S. Perry, Molecular mechanisms regulating myogenic determination and differentiation. *Front Biosci* **5**, d750 (2000).
47. L. Bajard *et al.*, A novel genetic hierarchy functions during hypaxial myogenesis: Pax3 directly activates Myf5 in muscle progenitor cells in the limb. *Genes & development* **20**, 2450-2464 (2006).
48. M. Lagha, D. Rocancourt, F. Relaix, [Pax3/Pax7-dependent population of skeletal muscle progenitor cells]. *Medecine sciences : M/S* **21**, 801-803 (2005).
49. M. A. Rudnicki, F. Le Grand, I. McKinnell, S. Kuang. (2008), vol. 73, pp. 323-331.
50. M. Kitzmann *et al.*, The muscle regulatory factors MyoD and myf- 5 undergo distinct cell cycle- specific expression in muscle cells. *The Journal of cell biology* **142**, 1447 (1998).
51. M. O. Ott, E. Bober, G. Lyons, H. Arnold, M. Buckingham, Early expression of the myogenic regulatory gene, myf- 5, in precursor cells of skeletal muscle in the mouse embryo. *Development (Cambridge, England)* **111**, 1097 (1991).
52. H. C. Olguin, Z. Yang, S. J. Tapscott, B. B. Olwin, Reciprocal inhibition between Pax7 and muscle regulatory factors modulates myogenic cell fate determination. *The Journal of cell biology* **177**, 769-779 (2007).
53. L. Megeney, M. A. Rudnicki, in *Biochem. Cell Biol.* (1995), vol. 73, pp. 723-732.
54. C. A. Berkes, S. J. Tapscott, MyoD and the transcriptional control of myogenesis. *Seminars in Cell and Developmental Biology* **16**, 585-595 (2005).
55. C. F. Bentzinger, Y. X. Wang, M. A. Rudnicki, Building muscle: molecular regulation of

myogenesis. *Cold Spring Harbor perspectives in biology* **4**, a008342 (2012).
56. S. Alessandra, D. Regis, K. Peggy, V. Stefan, M. B. Helen, Self- renewal and expansion of single transplanted muscle stem cells. *Nature* **456**, 502 (2008).
57. C. A. Collins *et al.*, Stem Cell Function, Self- Renewal, and Behavioral Heterogeneity of Cells from the Adult Muscle Satellite Cell Niche. *Cell* **122**, 289-301 (2005).
58. S. Kuang, K. Kuroda, F. Le Grand, M. A. Rudnicki, Asymmetric Self- Renewal and Commitment of Satellite Stem Cells in Muscle. *Cell* **129**, 999-1010 (2007).
59. S. Kuang, K. Kuroda, F. Le Grand, M. A. Rudnicki, Asymmetric self-renewal and commitment of satellite stem cells in muscle. *Cell* **129**, 999-1010 (2007).
60. F. Le Grand, A. E. Jones, V. Seale, A. Scimè, M. A. Rudnicki, Wnt7a activates the planar cell polarity pathway to drive the symmetric expansion of satellite stem cells. *Cell stem cell* **4**, 535-547 (2009).
61. N. C. Chang, F. P. Chevalier, M. A. Rudnicki, Satellite cells in muscular dystrophy–Lost in polarity. *Trends in molecular medicine* **22**, 479-496 (2016).
62. J. Dort, P. Fabre, T. Molina, N. A. Dumont, Macrophages are key regulators of stem cells during skeletal muscle regeneration and diseases. *Stem cells international* **2019**, (2019).
63. J. G. Tidball, S. A. Villalta, Regulatory interactions between muscle and the immune system during muscle regeneration. *American Journal of Physiology-Regulatory, Integrative and Comparative Physiology* **298**, R1173-R1187 (2010).
64. M. Saclier *et al.*, Differentially activated macrophages orchestrate myogenic precursor cell fate during human skeletal muscle regeneration. *Stem cells* **31**, 384-396 (2013).
65. T. Varga *et al.*, Macrophage PPARγ, a lipid activated transcription factor controls the growth factor GDF3 and skeletal muscle regeneration. *Immunity* **45**, 1038-1051 (2016).
66. A. Patsalos *et al.*, In situ macrophage phenotypic transition is affected by altered cellular composition prior to acute sterile muscle injury. *The Journal of physiology* **595**, 5815-5842 (2017).
67. K. Mojumdar *et al.*, Inflammatory monocytes promote progression of Duchenne muscular dystrophy and can be therapeutically targeted via CCR2. *EMBO molecular medicine* **6**, 1476-1492 (2014).
68. G. Juban *et al.*, AMPK Activation Regulates LTBP4-Dependent TGF-β1 Secretion by Pro-inflammatory Macrophages and Controls Fibrosis in Duchenne Muscular Dystrophy. *Cell reports* **25**, 2163-2176. e2166 (2018).
69. Y. Wang *et al.*, Aging of the immune system causes reductions in muscle stem cell populations, promotes their shift to a fibrogenic phenotype, and modulates sarcopenia. *The FASEB Journal* **33**, 1415-1427 (2018).
70. J. S. Baker, M. C. McCormick, R. A. Robergs, Interaction among skeletal muscle metabolic energy systems during intense exercise. *Journal of nutrition and metabolism* **2010**, (2010).
71. K. Sahlin, M. Tonkonogi, K. Söderlund, Energy supply and muscle fatigue in humans. *Acta Physiologica Scandinavica* **162**, 261-266 (1998).
72. H. Westerblad, J. D. Bruton, A. Katz, Skeletal muscle: energy metabolism, fiber types, fatigue and adaptability. *Experimental cell research* **316**, 3093-3099 (2010).
73. L. L. Spriet, M. J. Watt, Regulatory mechanisms in the interaction between carbohydrate and lipid oxidation during exercise. *Acta Physiologica Scandinavica* **178**, 443-452 (2003).

74. E. Spangenburg, F. Booth, Molecular regulation of individual skeletal muscle fibre types. *Acta physiologica Scandinavica* **178**, 413-424 (2003).
75. R. Bottinelli, C. Reggiani, Human skeletal muscle fibres: molecular and functional diversity. *Progress in biophysics and molecular biology* **73**, 195-262 (2000).
76. M. Periasamy, A. Kalyanasundaram, SERCA pump isoforms: their role in calcium transport and disease. *Muscle & Nerve: Official Journal of the American Association of Electrodiagnostic Medicine* **35**, 430-442 (2007).
77. Z. Gan, T. Fu, D. P. Kelly, R. B. Vega, Skeletal muscle mitochondrial remodeling in exercise and diseases. *Cell research*, 1 (2018).
78. B. Egan, J. R. Zierath, Exercise metabolism and the molecular regulation of skeletal muscle adaptation. *Cell metabolism* **17**, 162-184 (2013).
79. S.-M. Yoo, Y.-K. Jung, A molecular approach to mitophagy and mitochondrial dynamics. *Molecules and cells* **41**, 18 (2018).
80. N. Matsuda *et al.*, PINK1 stabilized by mitochondrial depolarization recruits Parkin to damaged mitochondria and activates latent Parkin for mitophagy. *The Journal of cell biology* **189**, 211-221 (2010).
81. D. Narendra, A. Tanaka, D.-F. Suen, R. J. Youle, Parkin is recruited selectively to impaired mitochondria and promotes their autophagy. *The Journal of cell biology* **183**, 795-803 (2008).
82. Y. Chen, G. W. Dorn, PINK1-phosphorylated mitofusin 2 is a Parkin receptor for culling damaged mitochondria. *Science* **340**, 471-475 (2013).
83. T. N. Nguyen, B. S. Padman, M. Lazarou, Deciphering the molecular signals of PINK1/Parkin mitophagy. *Trends in cell biology* **26**, 733-744 (2016).
84. A. Tanaka *et al.*, Proteasome and p97 mediate mitophagy and degradation of mitofusins induced by Parkin. *The Journal of cell biology* **191**, 1367-1380 (2010).
85. R. A. Hanna *et al.*, Microtubule-associated protein 1 light chain 3 (LC3) interacts with Bnip3 protein to selectively remove endoplasmic reticulum and mitochondria via autophagy. *Journal of Biological Chemistry* **287**, 19094-19104 (2012).
86. A. Vazquez-Martin *et al.*, Mitophagy-driven mitochondrial rejuvenation regulates stem cell fate. *Aging (Albany NY)* **8**, 1330 (2016).
87. R. Rojansky, M.-Y. Cha, D. C. Chan, Elimination of paternal mitochondria in mouse embryos occurs through autophagic degradation dependent on PARKIN and MUL1. *Elife* **5**, e17896 (2016).
88. G. Ashrafi, J. S. Schlehe, M. J. LaVoie, T. L. Schwarz, Mitophagy of damaged mitochondria occurs locally in distal neuronal axons and requires PINK1 and Parkin. *J Cell Biol* **206**, 655-670 (2014).
89. P. Martín-Maestro, R. Gargini, G. Perry, J. Avila, V. García-Escudero, PARK2 enhancement is able to compensate mitophagy alterations found in sporadic Alzheimer's disease. *Human molecular genetics* **25**, 792-806 (2015).
90. M. Martinez-Vicente *et al.*, Cargo recognition failure is responsible for inefficient autophagy in Huntington's disease. *Nature neuroscience* **13**, 567 (2010).
91. F. Vazquez *et al.*, PGC1α expression defines a subset of human melanoma tumors with increased mitochondrial capacity and resistance to oxidative stress. *Cancer cell* **23**, 287-301 (2013).

92. S. M. Parikh *et al.*, in *Seminars in nephrology*. (Elsevier, 2015), vol. 35, pp. 108-119.
93. R. A. Sinha, P. M. Yen, Thyroid hormone-mediated autophagy and mitochondrial turnover in NAFLD. *Cell & bioscience* **6**, 46 (2016).
94. M. C. Vila *et al.*, Mitochondria mediate cell membrane repair and contribute to Duchenne muscular dystrophy. *Cell death and differentiation* **24**, 330 (2017).
95. M. Kelly-Worden, E. Thomas, Mitochondrial dysfunction in Duchenne muscular dystrophy. *Open Journal of Endocrine and Metabolic Diseases* **4**, 211 (2014).
96. A. V. Kuznetsov *et al.*, Impaired mitochondrial oxidative phosphorylation in skeletal muscle of the dystrophin-deficient mdx mouse. *Molecular and cellular biochemistry* **183**, 87-96 (1998).
97. D. Ryu *et al.*, NAD+ repletion improves muscle function in muscular dystrophy and counters global PARylation. *Science translational medicine* **8**, 361ra139-361ra139 (2016).
98. J. T. Selsby, K. J. Morine, K. Pendrak, E. R. Barton, H. L. Sweeney, Rescue of dystrophic skeletal muscle by PGC-1α involves a fast to slow fiber type shift in the mdx mouse. *PloS one* **7**, e30063 (2012).
99. R. G. Barker, V. L. Wyckelsma, H. Xu, R. M. Murphy, Mitochondrial content is preserved throughout disease progression in the mdx mouse model of Duchenne muscular dystrophy, regardless of taurine supplementation. *American Journal of Physiology-Cell Physiology* **314**, C483-C491 (2017).
100. E. Marzetti *et al.*, Mitochondrial dysfunction and sarcopenia of aging: from signaling pathways to clinical trials. *The international journal of biochemistry & cell biology* **45**, 2288-2301 (2013).
101. E. Marzetti *et al.*, Skeletal muscle apoptotic signaling predicts thigh muscle volume and gait speed in community-dwelling older persons: an exploratory study. *PLoS One* **7**, e32829 (2012).
102. I. Bhatia-Kiššová, N. Camougrand, Mitophagy: a process that adapts to the cell physiology. *The international journal of biochemistry & cell biology* **45**, 30-33 (2013).
103. D. Ryu *et al.*, Urolithin A induces mitophagy and prolongs lifespan in C. elegans and increases muscle function in rodents. *Nature medicine* **22**, 879 (2016).
104. P. A. Andreux *et al.*, The mitophagy activator urolithin A is safe and induces a molecular signature of improved mitochondrial and cellular health in humans. *Nature Metabolism* **1**, 595 (2019).
105. H. Zhang *et al.*, NAD+ repletion improves mitochondrial and stem cell function and enhances life span in mice. *Science* **352**, 1436-1443 (2016).
106. R. N. Cortright, D. M. Muoio, G. L. Dohm, Skeletal muscle lipid metabolism: a frontier for new insights into fuel homeostasis. *The Journal of Nutritional Biochemistry* **8**, 228-245 (1997).
107. T. S. Worgall, Sphingolipids: major regulators of lipid metabolism. *Current Opinion in Clinical Nutrition & Metabolic Care* **10**, 149-155 (2007).
108. Y. A. Hannun, L. M. Obeid, Sphingolipids and their metabolism in physiology and disease. *Nature reviews Molecular cell biology* **19**, 175 (2018).
109. Y. A. Hannun, C. Luberto, Ceramide in the eukaryotic stress response. *Trends in cell biology* **10**, 73-80 (2000).
110. R. Pralhada Rao *et al.*, Sphingolipid metabolic pathway: an overview of major roles

played in human diseases. *Journal of lipids* **2013**, (2013).

111. T. Hornemann, S. Richard, M. F. Rütti, Y. Wei, A. von Eckardstein, Cloning and initial characterization of a new subunit for mammalian serine-palmitoyltransferase. *Journal of Biological Chemistry* **281**, 37275-37281 (2006).
112. C. R. Gault, L. M. Obeid, Y. A. Hannun, in *Sphingolipids as Signaling and Regulatory Molecules*. (Springer, 2010), pp. 1-23.
113. K. Venkataraman *et al.*, Upstream of growth and differentiation factor 1 (uog1), a mammalian homolog of the yeast Longevity Assurance Gene 1 (LAG1), regulatesN-Stearoyl-sphinganine (C18-(Dihydro) ceramide) synthesis in a fumonisin B1-independent manner in mammalian cells. *Journal of Biological Chemistry* **277**, 35642-35649 (2002).
114. Y. Mizutani, A. Kihara, Y. Igarashi, Mammalian Lass6 and its related family members regulate synthesis of specific ceramides. *Biochemical Journal* **390**, 263-271 (2005).
115. C. Riebeling, J. C. Allegood, E. Wang, A. H. Merrill, A. H. Futerman, Two mammalian longevity assurance gene (LAG1) family members, trh1 and trh4, regulate dihydroceramide synthesis using different fatty acyl-CoA donors. *Journal of Biological Chemistry* **278**, 43452-43459 (2003).
116. C. K. Savile, G. Fabrias, P. H. Buist, Dihydroceramide Δ4 desaturase initiates substrate oxidation at C-4. *Journal of the American Chemical Society* **123**, 4382-4385 (2001).
117. P. Bruni, C. Donati, Pleiotropic effects of sphingolipids in skeletal muscle. *Cellular and molecular life sciences* **65**, 3725-3736 (2008).
118. R. I. Castillo *et al.*, From molecules to the clinic: linking schizophrenia and metabolic syndrome through sphingolipids metabolism. *Frontiers in neuroscience* **10**, 488 (2016).
119. A. S. Havulinna *et al.*, Circulating ceramides predict cardiovascular outcomes in the population-based FINRISK 2002 cohort. *Arteriosclerosis, thrombosis, and vascular biology* **36**, 2424-2430 (2016).
120. J. A. Chavez, S. A. Summers, A ceramide-centric view of insulin resistance. *Cell metabolism* **15**, 585-594 (2012).
121. V. Filippov *et al.*, Increased ceramide in brains with Alzheimer's and other neurodegenerative diseases. *Journal of Alzheimer's Disease* **29**, 537-547 (2012).
122. K. A. Meadows, J. M. Holly, C. E. Stewart, Tumor necrosis factor-α–induced apoptosis is associated with suppression of insulin-like growth factor binding protein-5 secretion in differentiating murine skeletal myoblasts. *Journal of cellular physiology* **183**, 330-337 (2000).
123. S. Mebarek *et al.*, Inhibition of de novo ceramide synthesis upregulates phospholipase D and enhances myogenic differentiation. *Journal of cell science* **120**, 407-416 (2007).
124. Y. Nagata *et al.*, Sphingomyelin levels in the plasma membrane correlate with the activation state of muscle satellite cells. *Journal of Histochemistry & Cytochemistry* **54**, 375-384 (2006).
125. C. Sassoli *et al.*, Effects of S1P on skeletal muscle repair/regeneration during eccentric contraction. *Journal of cellular and molecular medicine* **15**, 2498-2511 (2011).
126. K. C. Loh *et al.*, Sphingosine-1-phosphate enhances satellite cell activation in dystrophic muscles through a S1PR2/STAT3 signaling pathway. *PloS one* **7**, e37218 (2012).
127. D. Kluepfel *et al.*, Myriocin, a new antifungal antibiotic from Myriococcum albomyces.

The Journal of antibiotics **25**, 109-115 (1972).

128. F. T. Bonezzi *et al.*, Sphingolipid synthesis inhibition by Myriocin administration enhances lipid consumption and ameliorates lipid response to myocardial ischemia reperfusion injury. *Frontiers in physiology* **10**, 986 (2019).
129. M. R. Hojjati *et al.*, Effect of myriocin on plasma sphingolipid metabolism and atherosclerosis in apoE-deficient mice. *Journal of Biological Chemistry* **280**, 10284-10289 (2005).
130. W. L. Holland *et al.*, Inhibition of ceramide synthesis ameliorates glucocorticoid-, saturated-fat-, and obesity-induced insulin resistance. *Cell metabolism* **5**, 167-179 (2007).
131. K. Kurek *et al.*, Inhibition of ceramide de novo synthesis reduces liver lipid accumulation in rats with nonalcoholic fatty liver disease. *Liver International* **34**, 1074-1083 (2014).
132. E. Salaun *et al.*, Myriocin prevents muscle ceramide accumulation but not muscle fiber atrophy during short-term mechanical unloading. *Journal of Applied Physiology* **120**, 178-187 (2015).
133. J. K. Mah *et al.*, A systematic review and meta-analysis on the epidemiology of Duchenne and Becker muscular dystrophy. *Neuromuscular Disorders* **24**, 482-491 (2014).
134. S. Ryder *et al.*, The burden, epidemiology, costs and treatment for Duchenne muscular dystrophy: an evidence review. *Orphanet journal of rare diseases* **12**, 79 (2017).
135. J. K. Mah, in *Duchenne Muscular Dystrophy*. (Springer, 2018), pp. 3-17.
136. J. A. Goldstein, E. M. McNally, Mechanisms of muscle weakness in muscular dystrophy. *Journal of General Physiology* **136**, 29-34 (2010).
137. M. C. Vila *et al.*, Mitochondria mediate cell membrane repair and contribute to Duchenne muscular dystrophy. *Cell Death & Differentiation* **24**, 330-342 (2017).
138. N. Brouilly *et al.*, Ultra-structural time-course study in the C. elegans model for Duchenne muscular dystrophy highlights a crucial role for sarcomere-anchoring structures and sarcolemma integrity in the earliest steps of the muscle degeneration process. *Human molecular genetics* **24**, 6428-6445 (2015).
139. H. Scholte, I. Luyt-Houwen, H. Busch, F. Jennekens, Muscle mitochondria from patients with Duchenne muscular dystrophy have a normal beta oxidation, but an impaired oxidative phosphorylation. *Neurology* **35**, 1396-1396 (1985).
140. W. Sperl *et al.*, High resolution respirometry of permeabilized skeletal muscle fibers in the diagnosis of neuromuscular disorders. *Molecular and cellular biochemistry* **174**, 71-78 (1997).
141. C. Handschin *et al.*, PGC-1α regulates the neuromuscular junction program and ameliorates Duchenne muscular dystrophy. *Genes & development* **21**, 770-783 (2007).
142. J. M. Percival, M. P. Siegel, G. Knowels, D. J. Marcinek, Defects in mitochondrial localization and ATP synthesis in the mdx mouse model of Duchenne muscular dystrophy are not alleviated by PDE5 inhibition. *Human molecular genetics* **22**, 153-167 (2013).
143. R. G. Barker, V. L. Wyckelsma, H. Xu, R. M. Murphy, Mitochondrial content is preserved throughout disease progression in the mdx mouse model of Duchenne muscular dystrophy, regardless of taurine supplementation. *American Journal of Physiology-Cell Physiology*, (2017).

144. E. Rybalka, C. A. Timpani, M. B. Cooke, A. D. Williams, A. Hayes, Defects in mitochondrial ATP synthesis in dystrophin-deficient mdx skeletal muscles may be caused by complex I insufficiency. *PloS one* **9**, (2014).
145. M. Pant *et al.*, Metabolic dysfunction and altered mitochondrial dynamics in the utrophin-dystrophin deficient mouse model of duchenne muscular dystrophy. *PloS one* **10**, (2015).
146. K. Palikaras, E. Lionaki, N. Tavernarakis, Coordination of mitophagy and mitochondrial biogenesis during ageing in C. elegans. *Nature* **521**, 525-528 (2015).
147. C. Ploumi, I. Daskalaki, N. Tavernarakis, Mitochondrial biogenesis and clearance: a balancing act. *The FEBS journal* **284**, 183-195 (2017).
148. V. Sorrentino, K. J. Menzies, J. Auwerx, Repairing mitochondrial dysfunction in disease. *Annual review of pharmacology and toxicology* **58**, 353-389 (2018).
149. K. M. Flanigan, Duchenne and Becker muscular dystrophies. *Neurologic clinics* **32**, 671-688 (2014).
150. M. Bakay *et al.*, Nuclear envelope dystrophies show a transcriptional fingerprint suggesting disruption of Rb–MyoD pathways in muscle regeneration. *Brain* **129**, 996-1013 (2006).
151. J. N. Haslett *et al.*, Gene expression comparison of biopsies from Duchenne muscular dystrophy (DMD) and normal skeletal muscle. *Proceedings of the National Academy of Sciences* **99**, 15000-15005 (2002).
152. M. Pescatori *et al.*, Gene expression profiling in the early phases of DMD: a constant molecular signature characterizes DMD muscle from early postnatal life throughout disease progression. *The FASEB Journal* **21**, 1210-1226 (2007).
153. F. Koyano *et al.*, Ubiquitin is phosphorylated by PINK1 to activate parkin. *Nature* **510**, 162-166 (2014).
154. E. F. Fang *et al.*, Mitophagy inhibits amyloid-β and tau pathology and reverses cognitive deficits in models of Alzheimer' s disease. *Nature neuroscience* **22**, 401-412 (2019).
155. C. Kang, M. A. Badr, V. Kyrychenko, E.-L. Eskelinen, N. Shirokova, Deficit in PINK1/PARKIN-mediated mitochondrial autophagy at late stages of dystrophic cardiomyopathy. *Cardiovascular research* **114**, 90-102 (2018).
156. E. Fiacco *et al.*, Autophagy regulates satellite cell ability to regenerate normal and dystrophic muscles. *Cell Death & Differentiation* **23**, 1839-1849 (2016).
157. L. García-Prat *et al.*, Autophagy maintains stemness by preventing senescence. *Nature* **529**, 37-42 (2016).
158. H. M. BLAu, C. Webster, G. K. Pavlath, Defective myoblasts identified in Duchenne muscular dystrophy. *Proceedings of the National Academy of Sciences* **80**, 4856-4860 (1983).
159. R. Sebori, A. Kuno, R. Hosoda, T. Hayashi, Y. Horio, Resveratrol decreases oxidative stress by restoring mitophagy and improves the pathophysiology of dystrophin-deficient mdx mice. *Oxidative medicine and cellular longevity* **2018**, (2018).
160. C. De Palma *et al.*, Autophagy as a new therapeutic target in Duchenne muscular dystrophy. *Cell death & disease* **3**, e418 (2012).
161. P. Grumati, L. Coletto, M. Sandri, P. Bonaldo, Autophagy induction rescues muscular dystrophy. *Autophagy* **7**, 426-428 (2011).

162. Y. S. Hori *et al.*, Resveratrol ameliorates muscular pathology in the dystrophic mdx mouse, a model for Duchenne muscular dystrophy. *Journal of Pharmacology and Experimental Therapeutics* **338**, 784-794 (2011).
163. A. M. Andres *et al.*, Mitophagy is required for acute cardioprotection by simvastatin. *Antioxidants & redox signaling* **21**, 1960-1973 (2014).
164. V. Sorrentino *et al.*, Enhancing mitochondrial proteostasis reduces amyloid-β proteotoxicity. *Nature* **552**, 187-193 (2017).
165. D. D' Amico *et al.*, The RNA-binding protein PUM2 impairs mitochondrial dynamics and mitophagy during aging. *Molecular cell* **73**, 775-787. e710 (2019).
166. A. Joshi, M. Kundu, Mitophagy in hematopoietic stem cells: the case for exploration. *Autophagy* **9**, 1737-1749 (2013).
167. N. Vannini *et al.*, The NAD-booster nicotinamide riboside potently stimulates hematopoiesis through increased mitochondrial clearance. *Cell stem cell* **24**, 405-418. e407 (2019).
168. N. A. Dumont, M. A. Rudnicki, Targeting muscle stem cell intrinsic defects to treat Duchenne muscular dystrophy. *NPJ Regenerative medicine* **1**, 16006 (2016).
169. J. R. Chamberlain, J. S. Chamberlain, Progress toward gene therapy for Duchenne muscular dystrophy. *Molecular Therapy* **25**, 1125-1131 (2017).
170. A. Aartsma-Rus *et al.*, Development of exon skipping therapies for Duchenne muscular dystrophy: a critical review and a perspective on the outstanding issues. *Nucleic acid therapeutics* **27**, 251-259 (2017).
171. Y.-L. Min, R. Bassel-Duby, E. N. Olson, CRISPR correction of Duchenne muscular dystrophy. *Annual review of medicine* **70**, 239-255 (2019).
172. L. Forcina, L. Pelosi, C. Miano, A. Musarò, Insights into the pathogenic secondary symptoms caused by the primary loss of dystrophin. *Journal of Functional Morphology and Kinesiology* **2**, 44 (2017).
173. G. Cordova, E. Negroni, C. Cabello-Verrugio, V. Mouly, C. Trollet, Combined therapies for Duchenne muscular dystrophy to optimize treatment efficacy. *Frontiers in genetics* **9**, 114 (2018).
174. J. Heilman, P. Andreux, N. Tran, C. Rinsch, W. Blanco-Bose, Safety assessment of Urolithin A, a metabolite produced by the human gut microbiota upon dietary intake of plant derived ellagitannins and ellagic acid. *Food and Chemical Toxicology* **108**, 289-297 (2017).
175. R. Kamath, M. Martinez-Campos, P. Zipperlen, A. Fraser, J. Ahringer, Effectiveness of specific RNA-mediated interference through ingested double-stranded RNA in C. elegans. *Genome Biol* **2**.
176. L. Mouchiroud *et al.*, The movement tracker: a flexible system for automated movement analysis in invertebrate model organisms. *Current protocols in neuroscience* **77**, 8.37. 31-38.37. 21 (2016).
177. M. Koopman *et al.*, A screening-based platform for the assessment of cellular respiration in Caenorhabditis elegans. *Nature protocols* **11**, 1798 (2016).
178. A. Pasut, A. E. Jones, M. A. Rudnicki, Isolation and culture of individual myofibers and their satellite cells from adult skeletal muscle. *JoVE (Journal of Visualized Experiments)*, e50074 (2013).

179. J. W. Rowe, R. L. Kahn, Successful aging. *The gerontologist* **37**, 433-440 (1997).
180. D. E. Bloom *et al.*, Macroeconomic implications of population ageing and selected policy responses. *The Lancet* **385**, 649-657 (2015).
181. M. C. Johnston, M. Crilly, C. Black, G. J. Prescott, S. W. Mercer, Defining and measuring multimorbidity: a systematic review of systematic reviews. *European Journal of Public Health* **29**, 182-189 (2019).
182. A. J. Cruz-Jentoft *et al.*, Writing Group for the European Working Group on Sarcopenia in Older People 2 (EWGSOP2), and the Extended Group for EWGSOP2. Sarcopenia: revised European consensus on definition and diagnosis. *Age Ageing* **48**, 16-31 (2019).
183. A. B. Mitnitski, A. J. Mogilner, K. Rockwood, Accumulation of deficits as a proxy measure of aging. *The Scientific World Journal* **1**, 323-336 (2001).
184. A. J. Murton, P. L. Greenhaff, Muscle atrophy in immobilization and senescence in humans. *Current opinion in neurology* **22**, 500-505 (2009).
185. P. Sousa-Victor *et al.*, Geriatric muscle stem cells switch reversible quiescence into senescence. *Nature* **506**, 316-321 (2014).
186. P. Sousa-Victor, P. Munoz-Canoves, Regenerative decline of stem cells in sarcopenia. *Molecular aspects of medicine* **50**, 109-117 (2016).
187. M. G. Giannoulis, F. C. Martin, K. S. Nair, A. M. Umpleby, P. Sonksen, Hormone replacement therapy and physical function in healthy older men. Time to talk hormones? *Endocrine reviews* **33**, 314-377 (2012).
188. D. L. Vetrano *et al.*, Frailty and multimorbidity: a systematic review and meta-analysis. *The Journals of Gerontology: Series A* **74**, 659-666 (2019).
189. M. König, D. Spira, I. Demuth, E. Steinhagen-Thiessen, K. Norman, Polypharmacy as a risk factor for clinically relevant sarcopenia: results from the Berlin Aging Study II. *The Journals of Gerontology: Series A* **73**, 117-122 (2018).
190. S. Choi, A. J. Snider, Sphingolipids in high fat diet and obesity-related diseases. *Mediators of inflammation* **2015**, (2015).
191. J. R. Ussher *et al.*, Inhibition of de novo ceramide synthesis reverses diet-induced insulin resistance and enhances whole-body oxygen consumption. *Diabetes* **59**, 2453-2464 (2010).
192. P. Zabielski *et al.*, The effect of high-fat diet and inhibition of ceramide production on insulin action in liver. *Journal of cellular physiology* **234**, 1851-1861 (2019).
193. S. M. Turpin *et al.*, Obesity-induced CerS6-dependent C16: 0 ceramide production promotes weight gain and glucose intolerance. *Cell metabolism* **20**, 678-686 (2014).
194. P. Hammerschmidt *et al.*, CerS6-derived sphingolipids interact with Mff and promote mitochondrial fragmentation in obesity. *Cell* **177**, 1536-1552. e1523 (2019).
195. B. Chaurasia *et al.*, Targeting a ceramide double bond improves insulin resistance and hepatic steatosis. *Science* **365**, 386-392 (2019).
196. J. Kurz, M. J. Parnham, G. Geisslinger, S. Schiffmann, Ceramides as novel disease biomarkers. *Trends in molecular medicine* **25**, 20-32 (2019).
197. S. A. Summers, The ART of lowering ceramides. *Cell metabolism* **22**, 195-196 (2015).
198. N. Turner *et al.*, A selective inhibitor of ceramide synthase 1 reveals a novel role in fat metabolism. *Nature communications* **9**, 1-14 (2018).
199. M. Pagadala, T. Kasumov, A. J. McCullough, N. N. Zein, J. P. Kirwan, Role of ceramides in

nonalcoholic fatty liver disease. *Trends in Endocrinology & Metabolism* **23**, 365-371 (2012).

200. M. Lone, T. Santos, I. Alecu, L. Silva, T. Hornemann, 1-Deoxysphingolipids. *Biochimica et Biophysica Acta (BBA)-Molecular and Cell Biology of Lipids* **1864**, 512-521 (2019).
201. P. A. Andreux *et al.*, Systems genetics of metabolism: the use of the BXD murine reference panel for multiscalar integration of traits. *Cell* **150**, 1287-1299 (2012).
202. A. S. Lee *et al.*, Aged skeletal muscle retains the ability to fully regenerate functional architecture. *Bioarchitecture* **3**, 25-37 (2013).
203. B. D. Cosgrove *et al.*, Rejuvenation of the muscle stem cell population restores strength to injured aged muscles. *Nature medicine* **20**, 255-264 (2014).
204. L. Liu *et al.*, Impaired notch signaling leads to a decrease in p53 activity and mitotic catastrophe in aged muscle stem cells. *Cell stem cell* **23**, 544-556. e544 (2018).
205. T. A. Rando, Stem cells, ageing and the quest for immortality. *Nature* **441**, 1080-1086 (2006).
206. F. D. Price *et al.*, Inhibition of JAK-STAT signaling stimulates adult satellite cell function. *Nature medicine* **20**, 1174 (2014).
207. K. Hanada, Serine palmitoyltransferase, a key enzyme of sphingolipid metabolism. *Biochimica et Biophysica Acta (BBA)-Molecular and Cell Biology of Lipids* **1632**, 16-30 (2003).
208. J. G. Eriksson *et al.*, Prenatal and childhood growth and physical performance in old age—findings from the Helsinki Birth Cohort Study 1934–1944. *Age* **37**, 108 (2015).
209. H. Trierweiler *et al.*, Sarcopenia: a chronic complication of type 2 diabetes mellitus. *Diabetology & metabolic syndrome* **10**, 25 (2018).
210. S. I. Haider, K. Johnell, G. R. Weitoft, M. Thorslund, J. Fastbom, The influence of educational level on polypharmacy and inappropriate drug use: a register-based study of more than 600,000 older people. *Journal of the American Geriatrics Society* **57**, 62-69 (2009).
211. J. CARROLL, One drug, many uses. *Biotechnology healthcare* **2**, 56 (2005).
212. V. Matyash, G. Liebisch, T. V. Kurzchalia, A. Shevchenko, D. Schwudke, Lipid extraction by methyl-tert-butyl ether for high-throughput lipidomics. *Journal of lipid research* **49**, 1137-1146 (2008).
213. O. L. Knittelfelder, B. P. Weberhofer, T. O. Eichmann, S. D. Kohlwein, G. N. Rechberger, A versatile ultra-high performance LC-MS method for lipid profiling. *Journal of Chromatography B* **951**, 119-128 (2014).
214. A. Othman *et al.*, Plasma deoxysphingolipids: a novel class of biomarkers for the metabolic syndrome? *Diabetologia* **55**, 421-431 (2012).
215. E. Pirinen *et al.*, Pharmacological Inhibition of poly (ADP-ribose) polymerases improves fitness and mitochondrial function in skeletal muscle. *Cell metabolism* **19**, 1034-1041 (2014).
216. H. Shiotsuki *et al.*, A rotarod test for evaluation of motor skill learning. *Journal of neuroscience methods* **189**, 180-185 (2010).
217. M. von Euler *et al.*, Inhalation of low concentrations of toluene induces persistent effects on a learning retention task, beam-walk performance, and cerebrocortical size in the rat. *Experimental neurology* **163**, 1-8 (2000).

218. N. E. Sanjana, O. Shalem, F. Zhang, Improved vectors and genome-wide libraries for CRISPR screening. *Nature methods* **11**, 783 (2014).
219. C. W. Law, Y. Chen, W. Shi, G. K. Smyth, voom: Precision weights unlock linear model analysis tools for RNA-seq read counts. *Genome biology* **15**, R29 (2014).
220. U. Raue *et al.*, Transcriptome signature of resistance exercise adaptations: mixed muscle and fiber type specific profiles in young and old adults. *Journal of applied physiology* **112**, 1625-1636 (2012).
221. G. Consortium, The Genotype-Tissue Expression (GTEx) pilot analysis: multitissue gene regulation in humans. *Science* **348**, 648-660 (2015).
222. H. Jantunen *et al.*, Objectively measured physical activity and physical performance in old age. *Age and ageing* **46**, 232-237 (2017).
223. G. P. Consortium, A global reference for human genetic variation. *Nature* **526**, 68-74 (2015).
224. K. F. O'Brien, L. M. Kunkel, Dystrophin and muscular dystrophy: past, present, and future. *Molecular genetics and metabolism* **74**, 75-88 (2001).
225. A. J. Lee, E. T. Buckingham, A. J. Kauer, K. D. Mathews, Descriptive phenotype of obsessive compulsive symptoms in males with Duchenne muscular dystrophy. *Journal of child neurology* **33**, 572-579 (2018).
226. D. Jones, Duchenne muscular dystrophy awaits gene therapy. *Nature biotechnology* **37**, 335 (2019).
227. S. BIOSCIENCE. (SOLID BIOSCIENCE, https://www.solidbio.com/about/media/press-releases/solid-biosciences-provides-sgt-001-program-update, 2019).
228. N. Deconinck, B. Dan, Pathophysiology of duchenne muscular dystrophy: current hypotheses. *Pediatric neurology* **36**, 1-7 (2007).
229. W. Pernice *et al.*, A double-blind placebo controlled trial of diltiazem in Duchenne dystrophy. *Klinische Wochenschrift* **66**, 565-570 (1988).
230. P. Balagopal *et al.*, Oxandrolone enhances skeletal muscle myosin synthesis and alters global gene expression profile in Duchenne muscular dystrophy. *American Journal of Physiology-Endocrinology and Metabolism* **290**, E530-E539 (2006).
231. N. Wein, L. Alfano, K. M. Flanigan, Genetics and emerging treatments for Duchenne and Becker muscular dystrophy. *Pediatric Clinics* **62**, 723-742 (2015).
232. D. Gloss, R. T. Moxley, S. Ashwal, M. Oskoui, Practice guideline update summary: Corticosteroid treatment of Duchenne muscular dystrophy: Report of the Guideline Development Subcommittee of the American Academy of Neurology. *Neurology* **86**, 465-472 (2016).
233. E. Matthews, R. Brassington, T. Kuntzer, F. Jichi, A. Y. Manzur, Corticosteroids for the treatment of Duchenne muscular dystrophy. *Cochrane Database of Systematic Reviews*, (2016).
234. S. M. Turpin-Nolan *et al.*, CerS1-derived C18: 0 ceramide in skeletal muscle promotes obesity-induced insulin resistance. *Cell reports* **26**, 1-10. e17 (2019).
235. K. Kurek *et al.*, Inhibition of ceramide de novo synthesis ameliorates diet induced skeletal muscles insulin resistance. *Journal of diabetes research* **2015**, (2015).
236. W. Yang *et al.*, Prediction of key gene function in spinal muscular atrophy using guilt by

association method based on network and gene ontology. *Experimental and therapeutic medicine* **17**, 2561-2566 (2019).

237. P. Fong, P. R. Turner, W. F. Denetclaw, R. A. Steinhardt, Increased activity of calcium leak channels in myotubes of Duchenne human and mdx mouse origin. *Science* **250**, 673-676 (1990).
238. A. Agrawal, G. Suryakumar, R. Rathor, Role of defective Ca 2+ signaling in skeletal muscle weakness: Pharmacological implications. *Journal of cell communication and signaling* **12**, 645-659 (2018).
239. A. M. Bellinger *et al.*, Hypernitrosylated ryanodine receptor calcium release channels are leaky in dystrophic muscle. *Nature medicine* **15**, 325 (2009).
240. J. K. McGeachie, M. D. Grounds, T. A. Partridge, J. E. Morgan, Age-related changes in replication of myogenic cells in mdx mice: quantitative autoradiographic studies. *Journal of the neurological sciences* **119**, 169-179 (1993).
241. C. Jiang *et al.*, Notch signaling deficiency underlies age-dependent depletion of satellite cells in muscular dystrophy. *Disease models & mechanisms* **7**, 997-1004 (2014).
242. L. Arnold *et al.*, Inflammatory monocytes recruited after skeletal muscle injury switch into antiinflammatory macrophages to support myogenesis. *Journal of Experimental Medicine* **204**, 1057-1069 (2007).
243. I. Dinulovic, R. Furrer, C. Handschin, in *Stem Cell Microenvironments and Beyond*. (Springer, 2017), pp. 141-169.
244. S. Miyatake, Y. Shimizu-Motohashi, S. i. Takeda, Y. Aoki, Anti-inflammatory drugs for Duchenne muscular dystrophy: focus on skeletal muscle-releasing factors. *Drug design, development and therapy* **10**, 2745 (2016).
245. S. A. Villalta, A. S. Rosenberg, J. A. Bluestone, The immune system in Duchenne muscular dystrophy: Friend or foe. *Rare diseases* **3**, e1010966 (2015).
246. F. De Santa, L. Vitiello, A. Torcinaro, E. Ferraro, The role of metabolic remodeling in macrophage polarization and its effect on skeletal muscle regeneration. *Antioxidants & Redox Signaling* **30**, 1553-1598 (2018).
247. M. Saclier, S. Cuvellier, M. Magnan, R. Mounier, B. Chazaud, Monocyte/macrophage interactions with myogenic precursor cells during skeletal muscle regeneration. *The FEBS journal* **280**, 4118-4130 (2013).
248. J. G. Quinlan *et al.*, Evolution of the mdx mouse cardiomyopathy: physiological and morphological findings. *Neuromuscular Disorders* **14**, 491-496 (2004).
249. H. Stedman *et al.*, The mdx mouse diaphragm reproduces the degenerative changes of Duchenne muscular dystrophy. *Nature* **352**, 536-539 (1991).
250. Y. Nagata, T. A. Partridge, R. Matsuda, P. S. Zammit, Entry of muscle satellite cells into the cell cycle requires sphingolipid signaling. *The Journal of cell biology* **174**, 245-253 (2006).
251. Y. A. Hannun, L. M. Obeid, The ceramide-centric universe of lipid-mediated cell regulation: stress encounters of the lipid kind. *Journal of Biological Chemistry* **277**, 25847-25850 (2002).
252. S. Spiegel, S. Milstien, Sphingosine-1-phosphate: an enigmatic signalling lipid. *Nature reviews Molecular cell biology* **4**, 397-407 (2003).
253. L. Boldrin, P. S. Zammit, J. E. Morgan, Satellite cells from dystrophic muscle retain

regenerative capacity. *Stem cell research* **14**, 20-29 (2015).
254. J. Meng, M. Bencze, R. Asfahani, F. Muntoni, J. E. Morgan, The effect of the muscle environment on the regenerative capacity of human skeletal muscle stem cells. *Skeletal muscle* **5**, 11 (2015).
255. L. A. Perandini, P. Chimin, D. d. S. Lutkemeyer, N. O. S. Câmara, Chronic inflammation in skeletal muscle impairs satellite cells function during regeneration: can physical exercise restore the satellite cell niche? *The FEBS journal* **285**, 1973-1984 (2018).
256. S. Biressi, E. H. Miyabara, S. D. Gopinath, P. M. Carlig, T. A. Rando, A Wnt-TGFβ2 axis induces a fibrogenic program in muscle stem cells from dystrophic mice. *Science translational medicine* **6**, 267ra176-267ra176 (2014).
257. C. J. Mann *et al.*, Aberrant repair and fibrosis development in skeletal muscle. *Skeletal muscle* **1**, 21 (2011).
258. J. G. Tidball, M. Wehling-Henricks, Macrophages promote muscle membrane repair and muscle fibre growth and regeneration during modified muscle loading in mice in vivo. *The Journal of physiology* **578**, 327-336 (2007).
259. S. A. Villalta, H. X. Nguyen, B. Deng, T. Gotoh, J. G. Tidball, Shifts in macrophage phenotypes and macrophage competition for arginine metabolism affect the severity of muscle pathology in muscular dystrophy. *Human molecular genetics* **18**, 482-496 (2009).
260. J. Hyzewicz *et al.*, Low-intensity training and the C5a complement antagonist NOX-D21 rescue the mdx phenotype through modulation of inflammation. *The American journal of pathology* **187**, 1147-1161 (2017).
261. S. A. Villalta, B. Deng, C. Rinaldi, M. Wehling-Henricks, J. G. Tidball, IFN-γ promotes muscle damage in the mdx mouse model of Duchenne muscular dystrophy by suppressing M2 macrophage activation and inhibiting muscle cell proliferation. *The Journal of Immunology* **187**, 5419-5428 (2011).
262. S. C. de Carvalho, L. M. Apolinário, S. M. M. Matheus, H. Santo Neto, M. J. Marques, EPA protects against muscle damage in the mdx mouse model of Duchenne muscular dystrophy by promoting a shift from the M1 to M2 macrophage phenotype. *Journal of neuroimmunology* **264**, 41-47 (2013).
263. A. Y. Manzur, T. Kuntzer, M. Pike, A. V. Swan, Glucocorticoid corticosteroids for Duchenne muscular dystrophy. *Cochrane database of systematic reviews*, (2008).
264. A. Gomez-Munoz *et al.*, Control of inflammatory responses by ceramide, sphingosine 1-phosphate and ceramide 1-phosphate. *Progress in lipid research* **61**, 51-62 (2016).
265. R. T. Okuro *et al.* (Eur Respiratory Soc, 2015).
266. A. Pasut, P. Oleynik, M. A. Rudnicki, in *Myogenesis*. (Springer, 2012), pp. 53-64.
267. P. M. Quiros, A. Mottis, J. Auwerx, Mitonuclear communication in homeostasis and stress. *Nature reviews Molecular cell biology* **17**, 213 (2016).
268. L. Heslop, J. Morgan, T. Partridge, Evidence for a myogenic stem cell that is exhausted in dystrophic muscle. *Journal of cell science* **113**, 2299-2308 (2000).
269. J. Smith, G. Fowkes, P. Schofield, Programmed cell death in dystrophic (mdx) muscle is inhibited by IGF-II. *Cell death and differentiation* **2**, 243-251 (1995).
270. C. Ginkel *et al.*, Ablation of neuronal ceramide synthase 1 in mice decreases ganglioside levels and expression of myelin-associated glycoprotein in oligodendrocytes. *Journal of Biological Chemistry* **287**, 41888-41902 (2012).

271. W. Ruangsiriluk *et al.*, Silencing of enzymes involved in ceramide biosynthesis causes distinct global alterations of lipid homeostasis and gene expression. *Journal of lipid research* **53**, 1459-1471 (2012).
272. D. C. Pant *et al.*, Loss of the sphingolipid desaturase DEGS1 causes hypomyelinating leukodystrophy. *The Journal of clinical investigation* **129**, 1240-1256 (2019).
273. X. Fu *et al.*, Urolithin A targets the PI3K/Akt/NF-κB pathways and prevents IL-1β-induced inflammatory response in human osteoarthritis: in vitro and in vivo studies. *Food & function* **10**, 6135-6146 (2019).
274. J. N. Eskra, A. Dodge, M. J. Schlicht, M. C. Bosland, Effects of black raspberries and their constituents on rat prostate carcinogenesis and human prostate cancer cell growth in vitro. *Nutrition and cancer*, 1-14 (2019).
275. Y. I. M. Saleem, H. Albassam, M. Selim, Urolithin A induces prostate cancer cell death in p53-dependent and in p53-independent manner. *European journal of nutrition*, 1-12 (2019).
276. E. Norden, E. H. Heiss, Urolithin A gains in antiproliferative capacity by reducing the glycolytic potential via the p53/TIGAR axis in colon cancer cells. *Carcinogenesis* **40**, 93-101 (2019).
277. T. M. Totiger *et al.*, Urolithin A, a novel natural compound to target PI3K/AKT/mTOR pathway in pancreatic cancer. *Molecular cancer therapeutics* **18**, 301-311 (2019).
278. J. Shaw *et al.*, in *Advances in cancer research*. (Elsevier, 2018), vol. 140, pp. 327-366.
279. A. Baer, W. Colon-Moran, N. Bhattarai, Characterization of the effects of immunomodulatory drug fingolimod (FTY720) on human T cell receptor signaling pathways. *Scientific reports* **8**, 1-10 (2018).
280. M. J. Genin *et al.*, Imidazopyridine and pyrazolopiperidine derivatives as novel inhibitors of serine palmitoyl transferase. *Journal of medicinal chemistry* **59**, 5904-5910 (2016).
281. Y.-S. Lee *et al.*, Myriocin, a serine palmitoyltransferase inhibitor, suppresses tumor growth in a murine melanoma model by inhibiting de novo sphingolipid synthesis. *Cancer biology & therapy* **13**, 92-100 (2012).
282. T. Kojima *et al.*, Discovery of novel serine palmitoyltransferase inhibitors as cancer therapeutic agents. *Bioorganic & medicinal chemistry* **26**, 2452-2465 (2018).
283. Y. Igarashi, Functional roles of sphingosine, sphingosine 1-phosphate, and methylsphingosines: in regard to membrane sphingolipid signaling pathways. *The Journal of Biochemistry* **122**, 1080-1087 (1997).

List of abbreviations

BMD Becker muscular dystrophy
CERS Ceramide synthase
Cis-eQTL *cis*-expression quantitative trait loci
CK Creatine kinase
CTX Cardiotoxin
DAPC Dystrophin associated protein complex
DAPI 4',6-diamidino-2-phenylindole
DEGS Dihydroceramide Δ4-desaturase
DMD Duchenne muscular dystrophy
DMEM Dulbecco's modified Eagle's medium
EBD Evans Blue Dye
FAP Fibro-adipogenic progenitors
FDA U.S Food and Drug Administration
GO Gene ontology
GSEA Gene Set Enrichment Analysis
H&E Hematoxylin and eosin
HD Homeobox DNA-binding domain
IL-6 Interleukin -6
IL-10 Interleukin-10
KDSR 3-ketodihydrosphingosine reductase
MEF2 Myocyte Enhancer Factor 2
MRF Myogenic regulatory factor
MuSC Muscle stem cell
MYF5 Myogenic Factor 5
MYH Myosin heavy chain
MYOD Myoblast Determination Protein
MOYG Myogenin
NAD^+ Nicotinamide adenine dinucleotide
NAFLD Non-alcoholic fatty liver disease
NR Nicotinamide riboside
OCR Oxygen consumption rate
RyR ryanodine receptor
PD Paired Domain
SERCA sarcoplasmic reticulum calcium ATPase
SM sphingomyelin
S1P sphingosine-1-phosphate
SPT serine palmitoyl-CoA transferase
UA Urolithin A
UPR^{mt} mitochondrial unfolded protein response

Curriculum Vitae

Peiling LUAN

+41 (0)79 856 66 86 | peilingluan@gmail.com
Av. des Figuier 20, Lausanne 1007
LinkedIn

STRENGTHS

Muscle stem cell specialist, preclinical trial expert

EDUCATION

Ph.D.Biotechnology and Bioengineering **09.2016-05.2020**

Ecole Polytechnique Fédérale de Lausanne (EPFL), Lausanne,CH

M.S., Life Sciences and technology **2014-2016**
Ecole Polytechnique Fédérale de Lausanne (EPFL), Lausanne, CH

Exchange semesters, Biomedical Engineering **2012-2013**
Ulm University, Baden-Württemberg, DE

B.S., Biomedical Engineering **2009-2013**
Southeast University, Nanjing, CN

CORE EXPERIENCE

Laboratory of Integrative Systems Physiology (LISP)

Ecole Polytechnique Fédérale de Lausanne (EPFL) **Lausanne, CH**
Doctoral researcher, Supervisor: Prof. Johan Auwerx ***2016.9– 2020.5***

Title: "Metabolic rescue of muscle and muscle stem cell functions in muscle diseases"

Scientific Activities:

- Goals: Identification of novel pharmacological compound, in order to open new therapeutic and nutritional routes for improving muscle repair in elderly and patients with muscular dystrophy.
- Collaborate with **Nestlé Institute of Health Sciences , Mitobridge and Amazentis SA**.
- Muscle stem cell expertise: isolation of muscle primary progenitors by flow-cytometry, culture, cytology-histology analysis, Crispr/Cas9
- Immunology: isolate monocytes and explore the polarization of macrophages
- Development of distinct organoid, including intestine, kidney; microfluidic device handling for drug screening
- Preclinical-studies on different mouse disease models and *C.elegans* models

Competencies:

- Laboratory Management activities: installation of the laboratory and implementation, stock management, orders, Safety-Health-Environment activities

- Scientific project leadership, Project proposals.
- Pro-active cross-functional collaborations
- Teaching assistant & supervision of master student
- Scientific communication (poster and oral presentations in local and international conferences)
- Scientific writing
- Participation to patent search, patent submission, contracts redaction (ex MTA) activities.
- Redaction of animal experimentation licences, defense of animal experimentation projects in internal committees.

Laboratory of Integrative Systems Physiology (LISP)

Ecole Polytechnique Fédérale de Lausanne (EPFL) **Lausanne, CH**
Master Thesis, Supervisor: Prof. Johan Auwerx **2015 – 2016**

- Metabolic regulation of stem cell senescence by NAD+ levels and mitochondrial function.
- Molecular and functional characterization of GCN5 in skeletal muscle stem cell function.
- Functional characterization of different PARP1 inhibitors on muscular dystrophy animal models.

ADDITIONAL EXPERIENCE

Chinese Association of Life Science in Switzerland **Zürich, CH**
Communications Officer **2016-2017**

- Organize the China & Switzerland Biomedical conference and promote the conference among the scientific workers
- Confirm and invite the guest speakers
- Communicate with the sponsors and help with the financing plan of the conference

Ecole Polytechnique Fédérale de Lausanne (EPFL) **Lausanne, CH**
Teaching and mentoring assistant ***2016-2020***

- Supervisor of Master student thesis, 100 hours
- Project Supervisor of graduate student Lab Immersion (Bio-501), 200 hours, 2015
- Teaching assistant of graduate student course Scientific project design in Drug Discovery (Bio-494), 40 hours, 2015
- Teaching assistant of undergraduate student course Biological Chemistry (Bio-212), 86 hours, 2012-2014

LANGUAGE SKILLS

English (Speaking C1, Reading C1), French (Speaking A2, Reading A2, having intensive course), German (Speaking B2, Reading B2), Mandarin (native language)

TECHNICAL SKILLS

- Animal models:
  - **mice** (RESAL certified, Swiss Association of Cantonal Veterinary): Muscle stem cell isolation, Blood collection by cardiac puncture on anesthetized animal or from tail vein on awake animal, Gavage, Intraperitoneal injection, Metabolic tests (including oGTT, ipITT, CLAMS, cold test, treadmill, VO2max), Mice breeding and management of mouse colonies, Tissue harvesting
  - ***Caenorhabditis elegans***: Extensive handling experience

- Wet laboratory techniques: Biomicroscopy, Blue Native Page, Cell culture, ELISA, Enzyme activity assays, DNA extraction, Immunocytochemistry, Immunoprecipitation, Isolation of primary cells (hepatocytes, fibroblasts and myoblast), Mitochondrial isolation, Molecular cloning, NAD+ extraction, PCR techniques, RNA extraction, Transfection and adenoviral transduction of mammalian cells, Tissue and Cell respiration assessment, Western blot

- Software skills: Adobe Illustrator, Adobe Photoshop, Solidworks, Canvas, Fiji, GraphPad, Microsoft Office

- Bioinformatics: Genomics, gene set enrichment analysis, sequence comparison tools (BLAST, Geneious)

Conference experience and awards

- 4th edition of Muscle Wasting Meeting in Ascona **2018**
- LIMNA conference **2017**
- Academic Scholarship - Southeast University **2010-2013**

SELECTED PUBLICATIONS

- **Luan P***, D'amico D*, Andreux P, Li H, Laurila P, Wohlend M, Crinsch C, Auwerx J. Urolithin A improves muscle function by rescuing mitophagy in muscular dystrophies. Science Translational Medicine, under revision.

- Laurila P, **Luan P**, Wohlend M, Herzig S, Park D, Oh M, Auwerx J. Sphingolipid depletion reverses age-associated sarcopenia and improves muscle regeneration. Nature Medicine, submitted.

- **Luan P***, Laurila P*, Zanou N, Place N, Auwerx J. Reduction of sphingolipid synthesis rescues muscular dystrophy. Science Translational Medicine, soon to submit.

- Wang S*, **Luan P***, Zhang H, Auwerx J. Control of muscle stem cell function by the acetyltransferase KAT2A. Cell Stem Cell, soon to submit.

- Li H, Wang X, Rukina D, Huang Q, Lin T, Sorrentino V, Zhang H, Bou Sleiman M, Arends D, McDaid A, **Luan P**, Ziari N, Velázquez-Villegas LA, Gariani K, Kutalik Z, Schoonjans K, Radcliffe RA, Prins P, Morgenthaler S, Williams RW, Auwerx J. An Integrated Systems Genetics and Omics Toolkit to Probe Gene Function. Cell Syst. 2018 Jan 24;6(1):90-102.e4. doi: 10.1016/j.cels.2017.10.016. Epub 2017 Nov 30.

- Zhang H, Ryu D, Wu Y, Gariani K, Wang X, **Luan P**, D'Amico D, Ropelle ER, Lutolf MP, Aebersold R, Schoonjans K, Menzies KJ, Auwerx J. NAD^+ repletion improves mitochondrial and stem cell function and enhances life span in mice. Science. 2016 Jun 17;352(6292):1436-43. doi: 10.1126/science.aaf2693.

EXTRACURRICULAR ACTIVITIES

Travel, Skiing, Reading, Swimming, Volleyball

PERSONAL DETAILS

Birthday: 28.11.1991 || Civil state: Married ||